Semiclassical Molecular Dynamics of Adiabatic and Nonadiabatic processes

UNIVERSITÀ DEGLI STUDI DI MILANO
DIPARTIMENTO DI CHIMICA

Ph.D. Candidate: Davide Moscato
id. N. R13523

Advisor: Prof. Michele Ceotto

Department of Chemistry
Università degli studi di Milano

Ph.D course in Chemistry
XXXVII Cycle

Academic Year 2024/2025

ABSTRACT

Molecular dynamics over the years has been established as a powerful yet simple technique capable of offering new physical insights into molecular processes. Some of the most desirable features are that it retains favorable scalability with the increasing number of degrees of freedom and can also be used to reproduce processes happening on relatively long time scales. On the other hand, since molecular dynamics is based on classical mechanics, it neglects the quantum nature of the nuclear motion and will eventually lead to some noticeable deviations from the real behavior of molecular systems. Instead, when considering a quantum picture of the nuclear dynamics all of the previously cited desirable features of molecular dynamics tend to vanish. Making the whole picture usually more complicated and computationally daunting. Semiclassical methods are in part able to conciliate the best features of both worlds, allowing for an intuitive description of the underlying nuclear quantum dynamics based on classical molecular dynamics and at the same time keeping the scalability in function of the system dimensionality favorable.

Throughout this thesis, semiclassical methods are employed to compute vibrational and vibronic spectra. More specifically, the first part of the manuscript will be dedicated to a quick review of the theory of the semiclassical initial value representation and its application to spectroscopy. The objective of the first Chapter is not only to show the origins of the semiclassical approximation but also to describe some strategies and further approximations that can pave the way for the simulations of molecular systems featuring up to 10000 degrees of freedom. Later, in the same part of the manuscript, it is also explored the idea of including nonadiabatic effects to

semiclassical vibrational spectroscopy by employing the Meyer-Miller-Stock-Thoss mapping.

In Chapter 3 a simple study case regarding the formaldehyde molecule is used to dig deeper into a tedious question regarding what can be regarded as a classical anharmonic effect and what can be classified as a "quantum effect" in vibrational spectroscopy. This Chapter also serves as a point to assess the validity of classical methods when compared to quantum mechanical ones and validate some of the best practices to employ regarding the former.

In Chapter 4 both quasiclassical and semiclassical methods are used to reproduce the experimental spectrum of the solvated G-quadruplex and explain the effects of solvation on the observed vibrational features. To describe the dynamics of such a large system, an empirical force field must be employed, a topic that is not central to the Chapter and will be used as a starting point for the next one, regards the reliability of this way to describe the potential energy surface. To avoid the loss of accuracy that comes with employing a classical force field, but at the same time avoid the computational overheads that can be faced when employing a full *ab initio* description of the system, in Chapter 5 semiclassical molecular dynamics is employed alongside hybrid QM/MM potentials to obtain a new physical picture of solvation for the case of solvated thymidine. Such system turned out to be a very intriguing study case where the modeling of solute-solvent interactions is essential for the correct reproducibility of the experimentally observed spectroscopic behavior.

Finally, in Chapter 6 applications of the novel time-averaged semiclassical approach to nonadiabatic vibronic spectroscopy are displayed for analytical model systems of growing difficulty. During this part of the manuscript, some of the features and limitations of the method will highlighted upon comparison with numerically exact results. Conclusions of the entire work and future perspectives are drawn in Chapter 7.

Manuscript accepted upon recommendation of:

Dr. Federica Agostini, Instute de Chimie Physique, Université Paris-Saclay

Prof. Andrea Lombardi, Dipartimento di Chimica, Biologia e Biotecnologie, Chimica generale e inorganica, Università Degli Studi di Perugia

Examination Board:

Prof. Marco Garavelli, Dipartimento di Chimica Industriale, Università degli Studi di Bologna

Prof. Jeremy Richardson, Department of Chemistry and Applied Biosciences, ETH Zurich

Prof. Riccardo Conte, Dipartimento di Chimica, Università degli Studi di Milano

Final Exam:

Università Degli Studi di Milano, room G23, Via Golgi 19, Milano

February, 3rd 2025

TABLE OF CONTENTS

---

[1] Chapter 3 contains modified parts taken from the published manuscript: Conte, R.; Aieta, C.; Botti; G.; Cazzaniga M.; Gandolfi M.; Lanzi C.; Mandelli G.; **Moscato D.**; Ceotto M.; Theor Chem Acc 142, 53 (2023).

[2] Chapter 4 contains modified parts taken from the published manuscript: **Moscato D.**; Gabas F.; Conte R.; Ceotto M.; J. Biomol. Struct. Dyn. 41(23), 1428-14258

---

[3] Chapter 5 contains modified parts taken from the published manuscript: **Moscato D.**; Mandelli G.; Bondanza M.; Lipparini F.; Conte R.; Mennucci B.; Ceotto M.; J. Am. Chem. Soc. 2024, 146, 12, 8179–8188

[4] Chapter 6 contains unpublished content of a work by **Moscato D.**; Gandolfi M.; Ceotto M.; TBD

LIST OF FIGURES

LIST OF TABLES

NOMENCLATURE

Greek Symbols

β	Boltzmann temperature
$\hat{\rho}$	Density operator
$\Phi_{H,t}$	Symplectic map that maps the phase space vector $\mathbf{z}_0$ to its time evolved under the Hamiltonian H
Ψ	Symbol of a generic wave function
$\sigma(\boldsymbol{\varepsilon},\beta)$	Absorption cross section as function evaluated at the temperature β

Physical Constants

$\hbar$	Reduced Planck constant
T	Sampling time
ε_0	Vacuum permittivity
c	Speed of light
k_b	Boltzmann constant
T	Temperature

Other Symbols

$\Im$	Immaginary part of a complex number
$\mathbf{J}$	Canonical symplecitc matrix
$\mathscr{L}$	Lagrangian function
$\Re$	Real part of a complex number

Acronyms / Abbreviations

AS	Adiabatic Switching
BO	Born-Oppenheimer
DC	Divide and Conquer
dG	2'-deoxyguanosine
DoF(s)	Degree(s) Of Freedom
EOM(s)	Equation(s) Of Motion
FC	Frank-Condon
FF	Force Fields
FSSH	Fewest Switches Surface-Hopping
HHKK	Herman-Heller-Kay-Kluk
HJ	Hamilton-Jacobi
HO	Harmonic Oscillator
IR	Infra-Red
IVR	Initial Value Representation
MAE	Mean Absolute Error
MC	Multiple-Coherent

MD	Molecular Dynamics
MM	Molecular-Mechanics
MMST	Meyer-Miller-Stock-Thoss
NAC	Non-Adiabatic Coupling
NA	Non Adiabatic
NQE(s)	Nuclear Quantum Effect(s)
ODE	Ordinary-Differential Equations
PBC	Periodic Boundary conditions
PDE(s)	Partial Differential Equation(s)
PES(s)	Potential Energy Surface(s)
PIMD	Path Integral Molecular Dynamics
PI	Path Integral
PME	Particle Mesh Ewald
QCT	Quasi Classical Trajectory
QMD	Quantum Molecular Dynamics
QM	Quantum Mechanics
RDF	Radial distribution function ($g(r)$)
RDM	Ring Deformation Mode
SAPT	Symmetry-Adapted intermolecular Perturbation Theory
SCF	Self Consistent Field
SC	Semiclassical
SEO	Singly-Excited Oscillator

TA	Time-Average
TBA	Thrombin Binding Aptamer
TDSE	Time-Dependent Schroedinger Equation
TISE	Time Independent Schroedinger Equation
UVRR	UV Resonant Raman
vDOS	vibrational Density Of States
WC	Watson-Crick
ZPE	Zero-Point Energy

CHAPTER 1

INTRODUCTION

Molecules are invisible objects to the naked eye. Their existence was first hypothesized by a series of empirical observations conducted by Robert Boyle. In 1811 Amedeo Avogadro coined the word "molecule" in a work where a method to associate a mass to the fundamental units of aggregates of atoms was defined. A more rigorous and physically valid argument regarding the existence of molecules is found in Ludwig Boltzmann statistical interpretation of thermodynamics. In particular, in some of the latest Boltzmann's works the hypothesis of existence of atoms and molecules led to successfully link their motion to macroscopic properties such as temperature and pressure. It was only later to Boltzmann death that these seminal concepts were irrefutably demonstrated by Albert Einstein [1] through the direct observation of Brownian motion.

To these days we are well aware of what molecular motion consequences are. A great effort of physicists, chemists and biologist was put also into developing methods and theories dedicated to predict and describe complex molecular systems behaviour. [2–8] One of such methods is Molecular Dynamics (MD). [9–13] this specific technique allows us to recover the atomistic detail that otherwise would be impossible to catch when dealing with experiments. Thanks to this powerful tool over the years it was possible to adress a series of tasks such as protein structure prediction, in *silico* pharmaceutical screenings and new materials development.

What is actually left behind in the usage of MD is that the nuclei are in fact "quantum objects". It is to these days still strongly debated how quantum effects regarding nuclei or more commonly regarded as Nuclear Quantum Effects, (NQEs) tend to be important in molecular processes. [14, 15] Some piece of literature clearly shows how incorporation of NQEs in realistic systems, also in the case in which heavy atoms motion is considered, [16, 17] clearly gives a more complete and more accurate picture. [18–20, 12] Though, it is also true that at first sight the picture of molecular motion where atoms follow a fixed trajectory given by classical equations of motion (EOMs) for an F-body system is not fully compatible with the principles of quantum mechanics. Another point that further enforce this concept is that while the solution of classical equation of motion are real $\mathbb{R} \rightarrow \mathbb{R}^F$ vector functions also commonly known as trajectories, which determines in a deterministic way the status of the system for any given instant. Instead, the solution of the Schrodinger equation and pivotal "object" of quantum mechanics, is the wave function, which is a complex defined function of all of the system degrees of freedom (nuclear and electronic) and time. If the solution is known, one could know the state of the system for every instant, but in this case the behaviour of the system will be no more deterministic but statistical. Clearly, these two points and many others that could be brought up can seem to invalidate the simple and intuitive idea that is commonly associated with molecular motion. On the other hand, theory is also able to show that the concept of trajectory is not actually incompatible with quantum mechanics. In fact, one of the more glaring results in Bohm interpretation of quantum mechanics [21] when adopting the Lagrangian frame, shows how the EOMs of the systems can be written as classical equation of motion with an additional term usually known as the "quantum-force". (see Appendix A) Therefore, with Bohmian dynamics one is able to introduce the concept of quantum trajectories. Another pivotal interpretation of quantum mechanics is the one proposed by Richard Feynman. [22] In the Path Integral (PI) descritpion it is demonstrated that the quantum amplitude of a system evolving in a given time span, with a fixed starting and ending point in space, is reproduced by considering all the possible paths connecting the two extreme points in the given time span. While this concept will be further explored in the following chapter, it can be understood from now that while the majority of the trajectories that connects the starting point and the ending point will be quantum trajectories (non classical trajectories), some of the trajectories instead will be classical and will contribute to create the quantum amplitude of the system as well.

With these two simple examples in mind, it is possible to state that classical mechanics and quantum mechanics are to some degree compatible between each other. Moreover, to further prove this concepts thanks to different flavors of approximation one is able to insert Nuclear Quantum Effects into standard MD. [23–43]
A popular class of approximate quantum dynamics methods based on classical MD are the SemiClassical (SC) ones. In this case, the origin of the approximations derives from the van Vleck-Gutzwiller propagator, [44] which as will be shown in the following chapter, can be obtained as stationary phase approximation of the PI. The main advantage of this kind of approaches is that the classical trajectories are used to compute quantum mechanical observables. [45–63] One particular field in which SC methods have been intensively developed and used is the simulation of vibrational and vibronic spectroscopies. [64] More precisely, as it will be shown in the next chapters, starting from the definition of surviving amplitude and applying it to that of the Herman-Kluk propagator [61, 65–67] it is possible to develop a series of approximations and algorithms that makes the computation of vibrational power spectra computationally cheap but accurate at the same time. [68–76]
The interest towards spectroscopy derives from the fact that it can be a very powerful tool which can be used to define the very own topology of molecules. While this is mostly true for techniques such as NMR spectroscopy or X-ray diffraction, other techniques can be used instead to understand the dynamics of molecular systems and the interactions with the environment. [77–83] Vibrational spectroscopy is a simple, yet effective technique that can be useful both for understanding the dynamical status of the systems and can also help to asses the presence of certain molecular structure patterns. Thanks to its widespread applicability infrared (IR) and Raman spectroscopies can be employed to analyze a very large manifold of molecular systems in almost any physical state. The main issue that one can encounter when dealing with vibrational spectroscopies is observed with systems featuring many degrees of freedom (DOFs) or when embedded in complex environment. In such cases it becomes essential to recur to computer simulations. As stated at the beginning of the chapter, using numerical methods to simulate microscopic processes allows us to regain the atomistic detail that the experiment cannot have. Within this framework, SC methods are in many way desirable. This is mostly due to the fact that, as will be shown in the next chapters, NQEs are conserved [84] while at the same time a strong bond with classical mechanics is also conserved. This in

other words means that one is able to obtain the same information that one could obtain with classical molecular dynamics and at the same time also add quantum mechanics on top of that. Another desirable quality derives from the fact that thanks to suitable approximations and some pioneering intuitions, [85, 86, 70] SC methods can be applied also to molecular systems featuring a large number of DoFs.

In this thesis I will show different applications of semiclassical methods to vibrational spectroscopies for systems with a high number of degrees of freedom and solvated systems. Furthermore, a brief section will be dedicated to application of semiclassical dynamics in the nonadiabatic regime. The outline of this work is composed as follow. In the next chapter the basic theoretical tools that will be used during the manuscript will be introduced. In particular, the discussion will start from the Feynman PI and a brief excursus on the different flavors of approximations that can be derived from this point. The focus will be set on the semiclassical approximation of the PI propagator and some theoretical developments that improved the theory. Another focal part of the discussion in the next chapter will be occupied by showing how the SC propagator can be swiftly applied to the computation of power spectra and how different approximations can improve the applicability of the method. Also, a parallelism between the classical and the quantum mechanical definition of power spectrum will be drawn and the concept of quasiclassical trajectory (QCT) introduced. In the final part of the chapter it will be also explored the possibility to expand the semiclassical theory beyond the Born-Oppenheimer approximation.

In very recent times, an interesting debate regarding the difference between NQEs and classical anharmonicity in theoretical vibrational spectroscopy has been initiated after the publication of the peer review process of a work by Y. Yang et. al..[87] Chapter three will be dedicated to shed some light on this topic by highlighting the differences between SC methods and QCT methods, by analyzing a simple but meaningful example. [84] Moreover, during this chapter will be shown that the choice of the initial conditions of the trajectories are crucial to obtain physically correct and accurate results. In the conclusion of this section two points will be made clear, what is classifiable as NQEs in vibrational spectroscopy and what cannot, and also that there are more physically correct and less physically correct choices that one can employ to initiate an MD simulation to compute vibrational spectra.

A significant case of study will be introduced in chapter 4, where QCT and SC methods will be applied to molecular systems featuring up to 10000 degrees of freedom. The main topic of the chapter will be set on the role of solvation in vibrational spectroscopy. Also, here it will be discussed the main critical issues that can be encountered in vibrational spectroscopy simulations of massive molecular systems. Since both SC and QCT are trajectory based methods, the employment of accurate Potential Energy Surfaces (PES) makes the simulation more accurate. On the other hand, when moving to higher dimensional systems in order to gain computational efficiency one has to lower the PES accuracy. While this seems to be affecting very little the molecular modelling community it can be an issue for more delicate applications as which can be the one of spectroscopic calculations. For this reason, it becomes necessary to find a practical solution that can be able to conciliate accuracy and computational efficiency. To this end in chapter 5 we explore the possibility of employing QM/MM and implicit solvation schemes to compute semiclassical vibrational spectra of water solvated thymidine. Moreover, thanks to the use of these advanced tools combined with accurate spectroscopic calculation, a physical picture of water solvation will be introduced which will give an atomistic explanation of the observed experimental data. Chapter 6 will conclude the section concerning the results by showing that semiclassical methods can be extended to problems regarding non adiabatic dynamics. [88–90] As will be shown in the next chapter, this is made possible by using the mapping Hamiltonian method introduced by H.D Mayer and W.H. Miller [91] and further developed by G. Stock and M. Thoss, [92] which maps the problem of propagating a wavepacket between more electronic states PESs to the problem of integrating a classical Hamiltonian.

Finally in the conclusion all the content of chapters is summarized and the different results discussed. To end the manuscript future perspectives and possible room for improvment of the shown methods will be discussed.

CHAPTER 2

THEORY

The main challenge in the field of quantum dynamics is to find the solution of the time dependent schroedinger equation (TDSE)

$$i\hbar\frac{\partial\Psi}{\partial t} = \hat{H}\Psi \; . \tag{2.1}$$

Where $\hat{H}$ is the Hamiltonian operator and Ψ a generic wavefunction dependent of time and all of the system DoFs. It is clear from eq. 2.1 that most of the difficulty in solving the TDSE depends on the complexity of the Hamiltonian operator. In fact, the analytical solution for simple systems such as the Harmonic Oscillator (HO) is actually known and trivial to derive. On the other hand, molecules are in general some of the most complicated physical systems that one can think of. This complexity arises mainly from the fact that these objects are in first instance an ensemble of N_e interacting electrons and N_N nuclei

$$\hat{H} = \hat{T}_N + \hat{T}_e + \hat{V}_{eN} + \hat{V}_{NN} + \hat{V}_{ee} \; . \tag{2.2}$$

One of the "simplest" way of writing the Hamiltonian of a molecular systems would be as done in equation 2.2, in which are present the nuclear kinetic energy ($\hat{T}_N$), the electron kinetic energy ($\hat{T}_e$), the electron-nuclei attraction ($\hat{V}_{eN}$), the nuclei-nuclei repulsion ($\hat{V}_{NN}$) and the electron-electron repulsion ($\hat{V}_{ee}$). By using this Hamiltonian, as commonly made most of the time, one is missing relativistic effects e.g. Spin-Orbit Coupling, rigid body rotations and traslations and other more complex interactions. On the other hand, when the nuclear kinetic term is neglected from eq. 2.2 and all of the other terms are grouped in the electronic Hamilotonian $\hat{H}_{el}$ approximated numerical solutions to the Time Indipendent Schroedinger Equation (TISE) are known within the Born-Oppenheimer (BO) approximation

$$\hat{H}_{el}\phi_k(\mathbf{r};\mathbf{R}) = E_k(\mathbf{R})\phi_k(\mathbf{r};\mathbf{R}) \ . \tag{2.3}$$

Where ϕ_k is k-th electronic adiabatic eigenfunction, $\mathbf{R}$ are the nuclear DoFs, $\mathbf{r}$ the electronic DoFs and E_k the k-th adiabatic eigenvalue also known as adiabatic potential energy. The focus of the thesis is mostly on the quantum dynamics of the nuclei. Therefore during this chapter it will be assumed as known the solution of the TISE or in general the analytical form of a potential energy function.

Before moving to the first section of this chapter, it is still necessary to make a distinction between two different types of nuclear dynamics. In fact, if one considers the Hamiltonian in eq. 2.2 as

$$\hat{H} = \sum_{J=1}^{N_N} -\frac{\hbar^2}{2M_J}\nabla^2_{R_J} + \hat{H}_{el} \ , \tag{2.4}$$

and apply it to eq. 2.1 by using the Born-Huang ansatz to the wave function

$$\Psi(\mathbf{R},\mathbf{r},t) = \sum_{k=1} \phi_k(\mathbf{r};\mathbf{R})\chi_k(\mathbf{R},t) \ . \tag{2.5}$$

It is easy to see that in the nuclear TDSE of a given electronic state l, there are two terms that couples the nuclear Dofs to the electronic ones

$$\begin{aligned} i\hbar\frac{\partial\chi_l}{\partial t}(\mathbf{R},t) = & \sum_{k=1}\sum_{J=1}^{N_N} \left[2d^J_{lk}(\mathbf{R})\nabla_{R_J} + D^J_{lk}(\mathbf{R})\right]\chi_k(\mathbf{R},t) \\ & + \left[\sum_{J=1}^{N_N} -\frac{\hbar^2}{2M_J}\nabla^2_{R_J} + E_l(\mathbf{R})\right]\chi_l(\mathbf{R},t) \ , \end{aligned} \tag{2.6}$$

these two terms are the Non-Adiabatic Coupling vectors (NAC) and are defined as

$$\begin{aligned} d^J_{lk} =& \langle \phi_l | \nabla_{R_J} | \phi_k \rangle \\ D^J_{lk} =& \langle \phi_l | \nabla^2_{R_J} | \phi_k \rangle \end{aligned} \, . \tag{2.7}$$

By neglecting the NAC, one enters in the adiabatic nuclear dynamics regime. This means that the nuclear dynamics is completely decoupled with the electronic one. The main consequence of this decoupling is that the system is restrained to evolve on a single BO surface. As shown by Koppel et al., [90] by evaluating the gradient of the nuclear coordinates of eq. 2.3 and multiplying it by $\phi^*_l(\mathbf{r};\mathbf{R})$ it is possible to obtain a very insightful identity for NAC vector $\mathbf{d}_{lk}(\mathbf{R})$

$$\mathbf{d}_{lk}(\mathbf{R}) = \frac{\langle \phi_l | \nabla_{\mathbf{R}} \hat{H}_{el} | \phi_k \rangle}{E_k(\mathbf{R}) - E_l(\mathbf{R})} \, . \tag{2.8}$$

In eq. 2.8 it is showed very clearly that the coupling term tend to be very important in steep points of the potential or when the two adiabats are close in energy. It is also easy to observe that when the two adiabatic PESs are well separated this coupling term can be neglected and the BO approximation holds. During the first part of the manuscript the BO approximation will be retained as valid and in second instance only the coupling with more electronic states will accounted for.

2.1 Feynman's Path Integral

The TDSE, as stated at the beginning of this chapter, is the problem to solve in order to know the true quantum mechanical evolution of a given system. It is simple to observe from eq. 2.1 that the formal solution is given by

$$\Psi(t) = e^{-\frac{i}{\hbar}\hat{H}t}\Psi(0) \, , \tag{2.9}$$

where $\Psi(0)$ is the initial value of the wavefunction, $\Psi(t)$ the time evolved wavefunction and $e^{-\frac{i}{\hbar}\hat{H}t}$ is the time evolution operator or also known as the quantum mechanical propagator. Direct application of eq. 2.9 is possible through the approximation of the Suzuki-Trotter formula as done in split-operator techniques, though it is not usually fit for systems with many DoFs. To find an approximation to the quantum propagator which can be suitable to be applied to more complex systems a different point of view must be considered.

A possible starting point is to project eq. 2.9 in the F-dimmensional position space $\mathbf{x}$

$$\Psi(\mathbf{x},t) = \langle \mathbf{x} | \Psi(t) \rangle = \left\langle \mathbf{x} \middle| e^{-\frac{i}{\hbar}\hat{H}t} \middle| \Psi(0) \right\rangle \tag{2.10}$$

by inserting the position space identity $\mathbb{1} = \int_{\mathbb{R}^F} d\mathbf{x}_0 |\mathbf{x}_0\rangle\langle\mathbf{x}_0|$ between the propagator and the initial wavefunction in eq. 2.10 it is possible to obtain an integral form of eq. 2.9

$$\Psi(\mathbf{x},t) = \int_{\mathbb{R}^F} d\mathbf{x}_0 \left\langle \mathbf{x} \middle| e^{-\frac{i}{\hbar}\hat{H}t} \middle| \mathbf{x}_0 \right\rangle \left\langle \mathbf{x}_0 \middle| \Psi(0) \right\rangle . \tag{2.11}$$

The term after the integral sign in eq. 2.11 is known as probability amplitude. The problem has now been shifted from applying directly the propagator to the wavefunction to finding a suitable representation to the probability amplitude. In order to do so, it is possible to split the propagation in infinitesimal slices of times $\delta t = \frac{t}{N}$ according to the Suzuki-Trotter decomposition

$$\left\langle \mathbf{x} \middle| e^{-\frac{i}{\hbar}\hat{H}t} \middle| \mathbf{x}_0 \right\rangle = \lim_{\delta t \to 0} \left\langle \mathbf{x} \middle| \left(e^{-\frac{i}{\hbar}\hat{T}\delta t} e^{-\frac{i}{\hbar}\hat{V}\delta t} \right)^N \middle| \mathbf{x}_0 \right\rangle . \tag{2.12}$$

Equation 2.12 is the Suzuki-Trotter decomposed form of the probability amplitude, where $\hat{T}$ is the kinetic operator and $\hat{V}$ is the potential one. The term inside the braket elevated to N can be rewritten as product multiplied by quantum mechanical identities in the position space

$$\begin{aligned} \left(e^{-\frac{i}{\hbar}\hat{T}\delta t} e^{-\frac{i}{\hbar}\hat{V}\delta t} \right)^N = & \left[\prod_{j=1}^{N-1} \int_{\mathbb{R}^F} d\mathbf{x}_{N-j} \, e^{-\frac{i}{\hbar}\hat{T}\delta t} e^{-\frac{i}{\hbar}\hat{V}\delta t} |\mathbf{x}_{N-j}\rangle\langle\mathbf{x}_{N-j}| \right] \\ & \times e^{-\frac{i}{\hbar}\hat{T}\delta t} e^{-\frac{i}{\hbar}\hat{V}\delta t} , \end{aligned} \tag{2.13}$$

by applying eq. 2.13 to eq. 2.12 and setting $\mathbf{x} = \mathbf{x}_N$

$$\begin{aligned}\left\langle \mathbf{x}_N \middle| e^{-\frac{i}{\hbar}\hat{H}t} \middle| \mathbf{x}_0 \right\rangle = \lim_{\delta t \to 0} \int_{\mathbb{R}^F} d\mathbf{x}_1 \cdots \int_{\mathbb{R}^F} d\mathbf{x}_{N-1} &\left\langle \mathbf{x}_N \middle| e^{-\frac{i}{\hbar}\hat{T}\delta t} e^{-\frac{i}{\hbar}\hat{V}\delta t} \middle| \mathbf{x}_{N-1} \right\rangle \\ \times &\left\langle \mathbf{x}_{N-1} \middle| e^{-\frac{i}{\hbar}\hat{T}\delta t} e^{-\frac{i}{\hbar}\hat{V}\delta t} \middle| \mathbf{x}_{N-2} \right\rangle \\ \times \ldots &\left\langle \mathbf{x}_1 \middle| e^{-\frac{i}{\hbar}\hat{T}\delta t} e^{-\frac{i}{\hbar}\hat{V}\delta t} \middle| \mathbf{x}_0 \right\rangle .\end{aligned} \tag{2.14}$$

At first look equation 2.14 can seem cumbersome, though it is possible to observe that since $\delta t \to 0$ the potential within a single slice of density amplitude can be evaluated at its midpoint

$$\left\langle \mathbf{x}_{N-1} \middle| e^{-\frac{i}{\hbar}\hat{T}\delta t} e^{-\frac{i}{\hbar}\hat{V}\delta t} \middle| \mathbf{x}_{N-2} \right\rangle = e^{-\frac{i}{\hbar}\frac{V(\mathbf{x}_{N-1})+V(\mathbf{x}_{N-2})}{2}\delta t} \left\langle \mathbf{x}_{N-1} \middle| e^{-\frac{i}{\hbar}\hat{T}\delta t} \middle| \mathbf{x}_{N-2} \right\rangle . \tag{2.15}$$

The remaining parts of eq. 2.15 are free particle density amplitudes which can be evaluated analytically giving the Path Integral (PI) formulation of eq. 2.12

$$\begin{aligned}\left\langle \mathbf{x}_N \middle| e^{-\frac{i}{\hbar}\hat{H}t} \middle| \mathbf{x}_0 \right\rangle &= \lim_{\delta t \to 0} \left(\frac{\det(\mathbf{M})}{2\pi i \hbar \delta t} \right)^{\frac{N}{2}} \int_{\mathbb{R}^F} d\mathbf{x}_1 \cdots \int_{\mathbb{R}^F} d\mathbf{x}_{N-1} \\ &\quad \times e^{\frac{i}{2\hbar} \sum_{j=1}^{N} \frac{\left(\mathbf{x}_j - \mathbf{x}_{j-1}\right)^T \mathbf{M}^{-1} \left(\mathbf{x}_j - \mathbf{x}_{j-1}\right)}{\delta t^2} \delta t} \\ &\quad \times e^{-\frac{i}{\hbar}\left(\frac{V(\mathbf{x}_0)}{2} + \frac{V(\mathbf{x}_N)}{2} + \sum_{j=1}^{N-1} V(\mathbf{x}_j) \right) \delta t} \\ &= \int \mathfrak{D}\left[\mathbf{x}\right] e^{\frac{i}{\hbar} S_t(\mathbf{x}_N, \mathbf{x}_0)} ,\end{aligned} \tag{2.16}$$

where $S_t(\mathbf{x}_N, \mathbf{x}_0)$ is the action evaluated along the path with fixed extreme points $\mathbf{x}_0$ and $\mathbf{x}_N$ separated by time lapse between 0 and t, $\mathfrak{D}[\mathbf{x}]$ is a functional that regulates the importance of each path to the whole density. According to equation 2.16 the probability amplitude of the system can be evaluated by considering all the paths connecting the fixed extreme points in the timespan $0 - t$. From this point it is possible to approximate eq. 2.16 in many different flavors making it applicable to complex systems. [93–96, 80] There are two main ways in which the PI formalism can be applied to many body systems such as molecules or dissipative systems. The most cumbersome one from the theoretical point of view is the one obtained by real-time discretization of eq. 2.16. From this branch methods such as QUAPI and

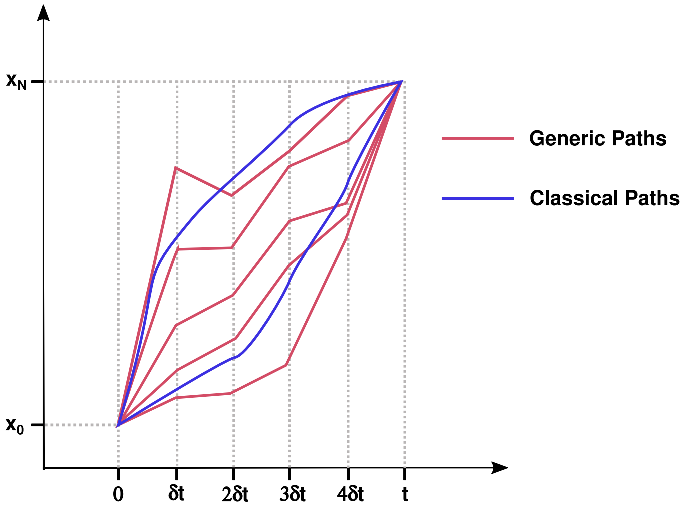

Fig. 2.1 Pictorial representation of the Path Integral formulation of quantum mechanics in which the contribution of classical paths is highlighted in blue.

all of its subsequent approximations can be derived. [97–100] Instead, the more widespread method to approximate PI is to consider the imaginary time evolution by Wick rotating eq. 2.16. This rotation permits to evaluate properties in the quantum canonical ensemble. Within this framework the canonical statistics of a particle becomes isomorphic with the classical evolution of a classical ring polymer composed by beads connected through harmonic springs. This isomorphism allowed to develop the field of Path Integral Molecular Dynamics, (PIMD) which links the quantum mechanical formalism to recover a classical-like picture of molecular dynamics. [101, 102, 37, 34] Another viable option to approximate the probability amplitude given by the Feynman's formalism can be found by considering only the classical paths connecting the two extreme points and the oscillation around them.

It is in fact possible to observe from figure 2.1 that while the majority of the paths are non classical, some of them that contribute to the total amplitude are instead classical and "easier" to account for.

2.2 Semiclassical approximation

The idea behind the semiclassical approximation is to consider the classical paths as the more important ones that contributes to the probability density while preserving quantum effects as small deviations around them.

According to the Hamilton principle a classical path ($\mathbf{q}(t)$) is a trajectory that makes the action functional stationary when evaluated along the same ($\delta S[\mathbf{q}(t)] = 0$). It is also implicit in the Hamilton principle that stationary points of the action corresponds to trajectories that evolve according to classical Equations Of Motion (EOMs)

$$\begin{cases} \dot{\mathbf{q}} = \frac{\partial H(\mathbf{p},\mathbf{q})}{\partial \mathbf{p}} \\ \dot{\mathbf{p}} = -\frac{\partial H(\mathbf{p},\mathbf{q})}{\partial \mathbf{q}} \end{cases} . \tag{2.17}$$

Therefore, in more practical terms, the semiclassical approximation of the quantum propagator is able to return quantum mechanical observables by direct evaluation of classical quantities. To approximate semiclassically eq. 2.16 the action is second order expanded around all of the classical paths (clps) that satisfy the double boundary condition imposed by the PI formulation

$$\langle \mathbf{x}_N | e^{-\frac{i}{\hbar}\hat{H}t} | \mathbf{x}_0 \rangle \approx \sum_{clps} \int \mathfrak{D}[\mathbf{x}] e^{\frac{i}{\hbar}\left[S_t^{cl} + \delta S_t^{cl} + \delta^2 S_t^{cl}\right]} , \tag{2.18}$$

it is easy to observe that since the action and all of its deviations are evaluated along the classical paths, the first deviation will be null, the zeroth order term will be constant with respect to the integration variable and the second order term is a quadratic form for which the analytical integral is known. Therefore by using the discrete form of eq. 2.16 to integrate the second order term in eq. 2.18 and by working out the algebra, it is possible to obtain

$$\begin{aligned} \langle \mathbf{x}_N | e^{-\frac{i}{\hbar}\hat{H}t} | \mathbf{x}_0 \rangle &\approx \lim_{N \to +\infty} \sum_{clps} \sqrt{\left(\frac{N \det(\mathbf{M})}{2\pi i \hbar t}\right)^N (2\pi i \hbar)^{N-1} \left| \frac{\partial S_N^{cl}}{\partial \mathbf{x}} \right|^{-1}} e^{\frac{i}{\hbar} S_N^{cl}} \\ &= \lim_{N \to +\infty} \sum_{clps} \sqrt{- \frac{\left| \frac{\partial^2 S_N^{cl}}{\partial \mathbf{x}_0 \partial \mathbf{x}_N} \right|}{(2\pi i \hbar)^F}} e^{\frac{i}{\hbar} S_N^{cl}} . \end{aligned} \tag{2.19}$$

At this point it is possible to get rid completely of the slicing and consider a continuos path where $\mathbf{x}_0 = \mathbf{x}(t = 0)$ and $\mathbf{x}_N = \mathbf{x}(t)$. Moreover, since the systems now evolve upon classical trajectories is convenient to switch to phase space variables $(\mathbf{p},\mathbf{q})$. It is now easier to see from eq. 2.19 that $-\left|\frac{\partial^2 S_N^{cl}}{\partial \mathbf{x}_0 \partial \mathbf{x}_N}\right| = \left|\frac{\partial \mathbf{q}(t)}{\partial \mathbf{p}(0)}\right|^{-1}$ and also

$$\left\langle \mathbf{x}_N \middle| e^{-\frac{i}{\hbar}\hat{H}t} \middle| \mathbf{x}_0 \right\rangle \approx \sum_{clps} \sqrt{\frac{\left|\frac{\partial \mathbf{q}(t)}{\partial \mathbf{p}(0)}\right|^{-1}}{(2\pi i\hbar)^F}} e^{\frac{i}{\hbar}S_t(\mathbf{q}_0,\mathbf{q}_t)-i\frac{\pi}{2}\nu} \ . \tag{2.20}$$

Equation 2.20 is known as the semiclassical approximation of the Feynman's PI, which is similar to another type of semiclassical propoagator proposed by van Vleck [44] many years before the work of Feynman. The added exponential term $e^{-i\frac{\pi}{2}\nu}$ contains the Maslov index which allows the continuity of the square root of the pre-exponential factor. [103] It is necessary to observe that the semiclassical propagator in eq. 2.20 it is able to reproduce nuclear quantum effects such as interference and delocalization. This is due to the fact that other than the sum on classical trajectories, their second order deviations inside the pre-exponential factor and their phase is also accounted for.

On the other hand, in terms of applicability eq. 2.20 is seriously problematic, the reason is due to two main points. The first one derives from the presence along classical paths of caustic points where $\left|\frac{\partial \mathbf{q}(t)}{\partial \mathbf{p}(0)}\right| = 0$, causing the pre-exponential factor to become singular. The other critical issue that makes the applicability of eq. 2.20 limited is due to the search of trajectories that satisfy the double boundary condition.

These two issues were solved in 1970 by W. H. Miller [104], by formulating the semiclassical (SC) propagator as an integral over initial position and momenta. The main idea is to map the sum over the classical paths with an integral over the initial momenta

$$\sum_{clps} \mapsto \int d\mathbf{p}(0) \left|\frac{\partial \mathbf{q}(t)}{\partial \mathbf{p}(0)}\right| \ , \tag{2.21}$$

in order to do so it is possible to write the quantum propagator in an integral form

$$e^{-\frac{i}{\hbar}\hat{H}t} = \iint d\mathbf{q}(0)d\mathbf{q}(t) \ \left|\mathbf{q}(t)\right\rangle\left\langle\mathbf{q}(t)\right| e^{-\frac{i}{\hbar}\hat{H}t} \left|\mathbf{q}(0)\right\rangle\left\langle\mathbf{q}(0)\right| \ , \tag{2.22}$$

in eq. 2.22 it is possible to use a change of variables $d\mathbf{q}(t) = d\mathbf{p}(0)\left|\frac{\partial \mathbf{q}(t)}{\partial \mathbf{p}(0)}\right|$ to make the integral depend on initial conditions only

$$e^{-\frac{i}{\hbar}\hat{H}t} = \iint d\mathbf{q}(0)d\mathbf{p}(0) \left|\frac{\partial \mathbf{q}(t)}{\partial \mathbf{p}(0)}\right| \left|\mathbf{q}(t)\right\rangle \left\langle \mathbf{q}(t)\right| e^{-\frac{i}{\hbar}\hat{H}t} \left|\mathbf{q}(0)\right\rangle \left\langle \mathbf{q}(0)\right| . \tag{2.23}$$

At this points it is possible to apply the semiclassical approximation to eq. 2.23 by substituting eq. 2.20 in it

$$e^{-\frac{i}{\hbar}\hat{H}t} \approx \iint d\mathbf{q}(0)d\mathbf{p}(0) \sqrt{\frac{\left|\frac{\partial \mathbf{q}(t)}{\partial \mathbf{p}(0)}\right|}{(2\pi i\hbar)^F}} e^{\frac{i}{\hbar}S_t(\mathbf{p}(0),\mathbf{q}(0)) - i\frac{\pi}{2}\nu} \left|\mathbf{q}(t)\right\rangle \left\langle \mathbf{q}(0)\right| . \tag{2.24}$$

Equation 2.24 is what is often referred as the semiclassical Initial Value Representation (SCIVR) of the quantum propagator. The main advantages of the IVR with respect to the van Vleck propagator is that the uniformity of the propagator is recovered and the double boundary problem is completely lifted. Moreover, the integration over the phase-space can be carried out numerically by means of Monte Carlo methods which are less computationally intensive than the search of multidimensional paths that satisfy a double boundary condition. Further advances in the SC dynamics were introduced by Heller, [105] which approximated the propagation of a quantum-wavepacket with the propagation of a swarm of a phase-space complex Gaussian with frozen width which obeys classical equation of motion

$$\left\langle \mathbf{x} \middle| \mathbf{p}, \mathbf{q} \right\rangle = \left(\frac{\det(\Gamma)}{\pi^F}\right)^{1/4} e^{-\frac{1}{2}(\mathbf{x}-\mathbf{q})^T \Gamma (\mathbf{x}-\mathbf{q}) + \frac{i}{\hbar}\mathbf{p}^T(\mathbf{x}-\mathbf{q})} . \tag{2.25}$$

Where in eq. 2.25, Γ is the diagonal width matrix of the Gaussian. Later in 1984, Herman and Kluk [61] revisited Heller's theory implying the necessity of a pre-exponential factor to properly account for quantum effects. Finally in 1994 Kay derived a general form for the frozen Gaussian propagator which is also known as the Heller-Herman-Kay-Kluk (HHKK) propagator [45, 65, 66]

$$\begin{aligned} e^{-\frac{i}{\hbar}\hat{H}t} \approx \iint \frac{d\mathbf{p}(0)d\mathbf{q}(0)}{(2\pi\hbar)^F} & C_t(\mathbf{p}(0),\mathbf{q}(0)) e^{\frac{i}{\hbar}S_t(\mathbf{p}(0),\mathbf{q}(0))} \\ & \times \left|\mathbf{p}(t),\mathbf{q}(t)\right\rangle \left\langle \mathbf{p}(0),\mathbf{q}(0)\right| \end{aligned} , \tag{2.26}$$

where $C_t(\mathbf{p}(0),\mathbf{q}(0))$ is the Herman-Kluk prefactor defined as

$$C_t(\mathbf{p}(0),\mathbf{q}(0)) = \sqrt{\left|\frac{1}{2}\left(\frac{\partial \mathbf{q}(t)}{\partial \mathbf{q}(0)} + \Gamma^{-1}\frac{\partial \mathbf{p}(t)}{\partial \mathbf{p}(0)}\Gamma - i\hbar\frac{\partial \mathbf{q}(t)}{\partial \mathbf{p}(0)}\Gamma + \frac{i\Gamma^{-1}}{\hbar}\frac{\partial \mathbf{p}(t)}{\partial \mathbf{q}(0)}\right)\right|} \ . \qquad (2.27)$$

Where $\frac{\partial \mathbf{i}(t)}{\partial \mathbf{j}(0)} = \mathrm{M}_{ij}(t)$ are the blocks of the monodromy (stability) matrix.

Both Miller's IVR (eq. 2.24) and the HHKK SC IVR (eq. 2.26) are practical ways to add NQEs to classical molecular dynamics. [62] This had led to further developments and approximations to which followed a widespread applicability of the method in various ambits. [56, 60, 106–116]

2.3 Semiclassical vibrational density of states

One of the possible applications of the HHKK propagator regards the computation of ground state vibrational spectra. Before delving into further details one fundamental difference has to be remarked. The IR spectrum of a generic system is defined as

$$\alpha(\omega,\beta) = \frac{\omega\left(1-e^{-\beta\hbar\omega}\right)}{2\pi}\int_{\mathbb{R}} dt\ e^{-i\omega t} C_{\mu\mu}(t)\ , \qquad (2.28)$$

where β is the Boltzmann temperature $\beta = \frac{1}{k_b T}$ and $C_{\mu\mu}(t)$ is the dipole auto-correlation function defined as

$$C_{\mu\mu}(t) = \mathrm{Tr}\left[e^{-\beta\hat{H}}\hat{\mu}e^{\frac{i}{\hbar}\hat{H}t}\hat{\mu}e^{-\frac{i}{\hbar}\hat{H}t}\right]\ . \qquad (2.29)$$

The application of eq. 2.28 will return a spectrum that will feature peaks with height and width that are regulated by the well known selection rules and also by temperature. Semiclassical approximations to IR spectroscopy has been already proposed [117, 118, 63], and a similar formula of eq. 2.28 can also be employed to compute Raman spectra.

Instead, the focus during this manuscript will be on the computation of vibrational power spectra or also known as vibrational Density Of States (vDOS). The vDOS is defined as

$$I(E) = \frac{\Re}{2\pi\hbar}\int_{\mathbb{R}} dt\; e^{\frac{i}{\hbar}Et}\langle\Psi(0)\big|e^{-\frac{i}{\hbar}\hat{H}t}\big|\Psi(0)\rangle\;, \tag{2.30}$$

where the integrand function of eq. 2.30 is known as the surviving amplitude and $\big|\Psi(0)\big\rangle$ is an arbitrary reference state. It is easy to observe that if the reference state is chosen as $\big|\Psi(0)\big\rangle = \sum_k \big|\big\langle\Psi(0)\big|k\big\rangle\big|\,\big|k\big\rangle$, such that $\hat{H}\big|k\big\rangle = E_k\big|k\big\rangle$, and apply it to eq 2.30

$$\begin{aligned} I(E) =& \frac{\Re}{2\pi\hbar}\sum_k\int_{\mathbb{R}} dt\; \big|\big\langle\Psi(0)\big|k\big\rangle\big|^2 e^{\frac{i}{\hbar}(E-E_k)} \\ =& \sum_k \big|\big\langle\Psi(0)\big|k\big\rangle\big|^2\,\delta\left(E-E_k\right)\;. \end{aligned} \tag{2.31}$$

Equation 2.31 clearly shows that the power spectrum differently from the IR spectrum in eq. 2.28 will feature all the eigenvalues of the Hamiltonian weighted by a proportional factor which in this case is given by $\big|\big\langle\Psi(0)\big|k\big\rangle\big|^2$. A semiclassical power spectrum can be simply obtained by sobsituting the HHKK propagator (eq. 2.26) into eq. 2.30

$$\begin{aligned} I(E) \approx& \frac{\Re}{2\pi\hbar}\int_{\mathbb{R}} dt\; e^{\frac{i}{\hbar}Et}\iint\frac{d\mathbf{p}(0)d\mathbf{q}(0)}{(2\pi\hbar)^F}\;C_t(\mathbf{p}(0),\mathbf{q}(0))e^{\frac{i}{\hbar}S_t(\mathbf{p}(0),\mathbf{q}(0))} \\ &\times\big\langle\Psi(0)\big|\mathbf{p}(t),\mathbf{q}(t)\big\rangle\big\langle\mathbf{p}(0),\mathbf{q}(0)\big|\Psi(0)\big\rangle\;, \end{aligned} \tag{2.32}$$

equation 2.32 feature a phase space integral which can be evaluated by using Monte Carlo methods. [119, 120] The square modulus of the time independent part ($\big|\big\langle\mathbf{p}(0),\mathbf{q}(0)\big|\Psi(0)\big\rangle\big|^2$) is the distribution from which each sample is extracted which is often referred as Husimi distribution. [121] At first sight, evaluation of the semiclassical vibrational power spectrum seems very practical and straightforward. Though, it is necessary to observe that the phase-space integrand is a strongly oscillating complex-defined function, this means that Monte Carlo convergence is very hard to reach unless tailored sampling strategies are used. [122–126] On this behalf, in order to improve convergence of eq. 2.32 W. H. Miller and A. L. Kaledin introduced the Time-Averaging (TA) approximation to the semiclassical vDOS. [68, 69] The overall idea behind this approach derives from the simple observation that if the phase-space average of a given property A is considered

$$\langle A \rangle_{ps} = \iint d\mathbf{p}(0) d\mathbf{q}(0)\, A(\mathbf{p}(0), \mathbf{q}(0)) \;, \tag{2.33}$$

and the time average of the same property

$$\langle A \rangle_{\mathrm{T}} = \frac{1}{\mathrm{T}} \int_0^{\mathrm{T}} dt\, A(\mathbf{p}(t), \mathbf{q}(t)) \;, \tag{2.34}$$

where T is the total sampling (simulation) time, and consider a time averaged version of the phase-space average

$$\begin{aligned} \langle A \rangle_{TA} =& \iint d\mathbf{p}(0) d\mathbf{q}(0)\, \frac{1}{\mathrm{T}} \int_0^{\mathrm{T}} dt\, A(\mathbf{p}(t), \mathbf{q}(t)) \\ =& \frac{1}{\mathrm{T}} \int_0^{\mathrm{T}} dt\, \iint d\mathbf{p}(t) d\mathbf{q}(t) A(\mathbf{p}(t), \mathbf{q}(t)) = \frac{\langle A \rangle_{ps}}{\mathrm{T}} \int_0^{\mathrm{T}} dt\; = \langle A \rangle_{ps} \;. \end{aligned} \tag{2.35}$$

The identity shown in eq. 2.35 shows that the a phase-space time-averaged property has the same expectation value of the phase-space one, the main advantage that comes by exploiting this identity is that a time-averaged function will be smoother i.e. simpler to integrate. The same idea can be applied to eq. 2.32

$$\begin{aligned} I(E) \approx & \frac{\Re}{\pi \hbar \mathrm{T}} \iint \frac{d\mathbf{p}(0) d\mathbf{q}(0)}{(2\pi\hbar)^F} \int_0^{\mathrm{T}} dt_1 \int_{\mathbb{R}} dt\, C_{t+t_1}(\mathbf{p}(t_1), \mathbf{q}(t_1)) \\ & \times e^{\frac{i}{\hbar}\left[S_{t_1+t}(\mathbf{p}(t_1), \mathbf{q}(t_1)) + E(t+t_1)\right]} \\ & \times \left\langle \Psi(0) \middle| \mathbf{p}(t+t_1), \mathbf{q}(t+t_1) \right\rangle \left\langle \mathbf{p}(t_1), \mathbf{q}(t_1) \middle| \Psi(0) \right\rangle \;, \end{aligned} \tag{2.36}$$

adding the time-average integral into the semiclassical power spectrum has the effect of sliding the initial time to t_1. By applying the change of variables $t_2 = t + t_1$, it is possible to rewrite the classical action as

$$\begin{aligned} S_{t_1+t}(\mathbf{p}(t_1), \mathbf{q}(t_1)) =& \int_{t_1}^{t_1+t} d\tau\, \mathscr{L}(\mathbf{p}(\tau), \mathbf{q}(\tau)) = \\ =& \int_0^{t_2} d\tau\, \mathscr{L}(\mathbf{p}(\tau), \mathbf{q}(\tau)) - \int_0^{t_1} d\tau\, \mathscr{L}(\mathbf{p}(\tau), \mathbf{q}(\tau)) \\ =& S_{t_2}(\mathbf{p}(0), \mathbf{q}(0)) - S_{t_1}(\mathbf{p}(0), \mathbf{q}(0)) \;, \end{aligned} \tag{2.37}$$

and eq. 2.36 can also be rewritten

$$\begin{aligned}I(E) \approx & \frac{\Re}{\pi\hbar T}\iint \frac{d\mathbf{p}(0)d\mathbf{q}(0)}{(2\pi\hbar)^F} \\ & \times \int_0^{\mathrm{T}} dt_1\ e^{-\frac{i}{\hbar}\left[S_{t_1}(\mathbf{p}(0),\mathbf{q}(0))+Et_1\right]}\left\langle \mathbf{p}(t_1),\mathbf{q}(t_1)\middle|\Psi(0)\right\rangle \\ & \times \int_{\mathbb{R}} dt_2\ C_{t_2}(\mathbf{p}(t_1),\mathbf{q}(t_1))e^{\frac{i}{\hbar}\left[S_{t_2}(\mathbf{p}(0),\mathbf{q}(0))+Et_2\right]}\left\langle \Psi(0)\middle|\mathbf{p}(t_2),\mathbf{q}(t_2)\right\rangle .\end{aligned} \tag{2.38}$$

In equation 2.38 the semiclassical equation for the power spectrum has been rewritten as a phase space integral of two time integration. Though, true separability between t_1 and t_2 cannot be reached without the separable approximation of the prefactor introduced by Kaledin and Miller [68, 69]

$$C_{t_2}(\mathbf{p}(t_1),\mathbf{q}(t_1)) \approx e^{\frac{i}{\hbar}\left[\phi_{t_2}(\mathbf{p}(0),\mathbf{q}(0))-\phi_{t_1}(\mathbf{p}(0),\mathbf{q}(0))\right]}\ , \tag{2.39}$$

where $\phi_t(\mathbf{p}(0),\mathbf{q}(0)) = \mathrm{phase}\left[C_t(\mathbf{p}(0),\mathbf{q}(0))\right]$. The approximation is exact in case of an harmonic systems, the same is not true for general systems. The consequences of this simplification are not fully known apart for the augmented numerical numerical stability that comes with it. By applying the separable approximation to eq. 2.38 it is possible to observe that the integral in t_1 is the complex conjugate (c.c.) of the one in t_2. This means that the phase-space integrand can be rewritten as a real positive-defined function

$$\begin{aligned}I(E) \approx & \frac{1}{(2\pi\hbar)^F}\iint d\mathbf{p}(0)d\mathbf{q}(0) \\ & \times \frac{1}{2\pi\hbar\mathrm{T}}\left|\int_0^{\mathrm{T}} dt\ e^{\frac{i}{\hbar}\left[S_t(\mathbf{p}(0),\mathbf{q}(0))+\phi_t(\mathbf{p}(0),\mathbf{q}(0))+Et\right]}\left\langle \Psi(0)\middle|\mathbf{p}(t),\mathbf{q}(t)\right\rangle\right|^2 .\end{aligned} \tag{2.40}$$

Equation 2.40 is often referred as the Time-Averaged SemiClassical Inital Value Representation (TA SCIVR), and to the current knowledge of the author it is the only semiclassical method based on the HHKK propagator applicable to molecular systems.

As previously stated, both Γ and $\left|\Psi(0)\right\rangle$ can be are arbitrary and the final result should be invariant with respect to their choice. On the other hand, some choices makes the numerical convergence of eq. 2.40 faster. In particular, was already observed by Kaledin and Miller that by choosing the width parameter equal to the harmonic frequencies of each vibrational DoF (γ_j), and the reference state as $\left|\mathbf{p}_{eq}, \mathbf{q}_{eq}\right\rangle$, where $p_{j,eq} = \sqrt{\hbar\gamma_j}$, makes the TA SCIVR converge with almost 1000 trajectories per DoF. It is worth observing, that a choice like this other then being intuitive brings many advantages. The more obvious one, is that the coherent-state overlap $\left\langle \mathbf{p}_{eq}, \mathbf{q}_{eq} \middle| \mathbf{p}(t), \mathbf{q}(t) \right\rangle$ can be evaluated analytically and when its square modulus is evaluated at $t = 0$ returns a phase space Gaussian which is used as a weight function for the Monte Carlo integration

$$\left|\left\langle \mathbf{p}_{eq}, \mathbf{q}_{eq} \middle| \mathbf{p}(0), \mathbf{q}(0) \right\rangle\right|^2 = e^{-\frac{1}{2}\left(\mathbf{q}_{eq}-\mathbf{q}(0)\right)^T \Gamma \left(\mathbf{q}_{eq}-\mathbf{q}(0)\right) - \frac{1}{2\hbar^2}\left(\mathbf{p}_{eq}-\mathbf{p}(0)\right)^T \Gamma^{-1}\left(\mathbf{p}_{eq}-\mathbf{p}(0)\right)} . \tag{2.41}$$

A less obvious one regards the choice of Γ. In fact, by choosing a tight width parameter at first sight should ease numerical convergence, but will cause to lose most of the quantum delocalization effects. Instead, when a loose width parameter is chosen, numerical convergence will be more difficult to reach.

From a more practical point of view, the requirements to compute the TA SCIVR power spectrum are just a few. To sample initial conditions as proposed by Kaledin and Miller , the Hessian matrix of the potential at the equilibrium geometry ($\mathbb{H}_{V(\mathbf{q}_{eq})}$) has to be computed and diagonalized to obtain the harmonic frequencies. Another prerequisite fundamental for the correct evaluation of eq. 2.40, is the use of symplectic algorithms to propagate the trajectories and the monodromy matrix ($M(t)$) according to

$$\dot{\mathrm{M}}(t) = \mathbf{J}^T \mathbb{H}_{H(\mathbf{p}(t),\mathbf{q}(t))} \mathrm{M}(t) , \tag{2.42}$$

where $\mathbf{J}$ is the canonical symplectic matrix and $\mathbb{H}_{H(\mathbf{p}(t),\mathbf{q}(t))}$ is the Hessian matrix of the Hamiltonian evaluated at time t. This last point is important mostly because as pointed previously by Kay, [45] trajectories that evolves in anharmonic potentials could exhibit a chaotic behaviour for which the HK prefactor suffer an exponential growth over time. This behaviour has often the effect to lower the accuracy of the estimated observable or return nonphysical results. Therefore, while non-symplectic integrators generally do not conserve the unitarity of the monodromy matrix determinant and will cause the pre-exponential factor to grow indefinetly along the dynamics, symplectic algorithms should be able to discriminate between chaotic trajectories and stable ones. To avoid the inclusion of chaotic trajectories in the Monte Carlo estimation of eq. 2.40 a rejection method proposed by H. Wang et. al. is usually used. [127]

While the time averaging procedure opens the possibility to compute semiclassical power spectra of systems featuring up to 10 DoFs, the possibility of going over this number is still very limited. One of the most obvious reasons regards the fact that accurate analytical Potential Energy Surface (PES) for large systems are difficult to fit, moreover the computation of numerical Hessians and gradients does not scale favorably with increasing number of DoF. The alternative would be to employ ab-initio methods, unfortunately the number of Hessian matrices and trajectories required would make this alternative not viable. The second reason regards the so called "curse of dimensionality", for which when $\left|\Psi(0)\right\rangle = \left|\mathbf{p}_{eq},\mathbf{q}_{eq}\right\rangle$

$$\left\langle \mathbf{p}_{eq},\mathbf{q}_{eq} \middle| \mathbf{p}(t),\mathbf{q}(t)\right\rangle = \prod_{j=1}^{F} \left\langle p_{j,eq},q_{j,eq} \middle| p_j(t),q_j(t)\right\rangle , \tag{2.43}$$

meaning that increasing values of F increases the probability that one or more elements of the product are near or equal to zero.

2.3.1 Semiclassical spectroscopy of high dimensional systems

Computation of semiclassical spectra on-the-fly was made available by the introduction of the Multiple-Coherent (MC) SCIVR. [86, 70] The underlying idea is based on a pivoting work by Heller and De Leon, [85] in which was demonstrated that accurate semiclassical eigenenergies and eigenfunctions can be obtained even by a single trajectory if it is run a the correct but unknown energy. Therefore, the assumption made in the MC SCIVR is that an accurate spectrum can be obtained by running just few trajectories (ideally one per spectral feature) originated in the surrounding of the exact eigenvalue. The simplest way to obtain an estimate of the vibrational eigenvalues is to consider the potential as harmonic for every DoF where $E_j = \hbar\gamma_j\left(n_j + \frac{1}{2}\right)$. In this case the phase space torus which is isoenergetic to the eigenvalues of the quantum harmonic oscillator will be spanned by

$$\begin{cases} q_j = & q_{j,eq} + \sqrt{\frac{\hbar}{\gamma_j}\left(2n_j+1\right)}\cos\left(\theta_j\right) \\ p_j = & \sqrt{\hbar\gamma_j\left(2n_j+1\right)}\sin\left(\theta_j\right) \end{cases} , \tag{2.44}$$

meaning that the trajectories could be initialized for any value of $\theta_j \in [0, 2\pi)$, in practice the most common choice is to start from equilibrium position $\theta = \frac{\pi}{2}$. The MC SCIVR working formula is analogous to the one of the TA SCIVR (eq. 2.40), with the only difference that the phase-space integration has been replaced by a sum over the number of trajectories N_{tr}

$$
\begin{aligned}
I(E) \approx & \frac{1}{(2\pi\hbar)^F} \sum_{K=1}^{N_{tr}} \frac{1}{2\pi\hbar \mathrm{T}} \\
& \times \left| \int_0^{\mathrm{T}} dt\, e^{\frac{i}{\hbar}\left[S_t^{(K)}(\mathbf{p}_{eq},\mathbf{q}_{eq}) + \phi_t^{(K)}(\mathbf{p}_{eq},\mathbf{q}_{eq}) + Et\right]} \left\langle \Psi^{(K)} \middle| \mathbf{p}^{(K)}(t), \mathbf{q}^{(K)}(t) \right\rangle \right|^2 .
\end{aligned}
\tag{2.45}
$$

Where

$$
\left|\Psi^{(K)}(0)\right\rangle = \prod_{j=1}^{F} \sum_{l=1}^{N_c} \varepsilon_{l,J}^{(K)} \left| p_{j,eq}^{(K)}, q_{j,eq}^{(K)} \right\rangle ,
\tag{2.46}
$$

in which N_c is the number of coherent states, and $\varepsilon_{l,J}$ is a coefficient that can be used to enforce parity or molecular symmetry to enhance or suppress signals to specific mode excitations or symmetry species. In most of the applications that will be shown in the next chapters to assign with more certainty signals of the power spectrum the number of coherent states will be chosen equal to two, and the parity symmetry is exploited

$$
\left|\Psi(0)\right\rangle = \prod_{j=1}^{F} \left[\varepsilon_{1,j} \left| p_{j,eq}, q_{j,eq} \right\rangle + \varepsilon_{2,j} \left| -p_{j,eq}, q_{j,eq} \right\rangle \right] .
\tag{2.47}
$$

In this case, the sign of $\varepsilon_{2,j}$ determines if an odd ($\varepsilon_{2,j} = -1$) or even ($\varepsilon_{2,j} = 1$) number if quanta in the mode j is associated to the peak to be assigned. For example, in a three-mode molecule $\varepsilon = (\varepsilon_{1,1}, \varepsilon_{2,1}; \varepsilon_{1,2}, \varepsilon_{2,2}; \varepsilon_{1,3}, \varepsilon_{2,3})$, the Zero-Point Energy (ZPE) peak and even excitations ($n_j = 2, 4, 6, \dots$) will be highlighted when $\varepsilon = (1,1;1,1;1,1;1,1)$, otherwise all the odd excitations ($n_j = 1, 3, 5, \dots$) will be highlighted when $\varepsilon_{2,j} = -1$. As stated before, to obtain more accurate results and obtain also a good spectral resolution for higher excitations (overtones), a trajectory with energy near every vibrational state should be run. Though, numerous works has shown that even a single trajectory ran at the harmonic ZPE is able to return accurate enough estimates to the fundamentals eigenenergies. [86, 70, 128, 129]

While with the development of the MC SCIVR it was possible to converge the SC IVR within just few trajectories, allowing to compute spectra from trajectories computed with ab-initio Born-Oppenheimer Molecular Dynamics (BOMD). An issue that still stands is the infamous curse of dimensionality regarding the nuclear overlap in eq. 2.45. To overcome this issue a Divide-and-Conquer scheme (DC SC IVR) was developed. [72, 73] The underlying idea within this method is to divide the whole considered F-dimensional system onto a set of subspaces of lower dimensionality (M) from which partial spectra can be computed, eventually the whole spectrum can be rebuilt upon convolution of the same. The working equation of the DC SC IVR is the same of the MC SC IVR (eq. 2.45), with the only difference that in this case the dynamical quantities are projected in subspaces of lower dimensionality

$$\begin{aligned}\tilde{I}(E) \approx & \frac{1}{(2\pi\hbar)^M} \sum_{K=1}^{N_{tr}} \frac{1}{2\pi\hbar \mathrm{T}} \\ & \times \left| \int_0^{\mathrm{T}} dt\ e^{\frac{i}{\hbar}\left[\tilde{S}_t^{(K)}(\tilde{\mathbf{p}}_{eq},\tilde{\mathbf{q}}_{eq})+\tilde{\phi}_t^{(K)}(\tilde{\mathbf{p}}_{eq},\tilde{\mathbf{q}}_{eq})+Et\right]} \left\langle \tilde{\Psi}^{(K)} \middle| \tilde{\mathbf{p}}^{(K)}(t), \tilde{\mathbf{q}}^{(K)}(t) \right\rangle \right|^2 ,\end{aligned} \tag{2.48}$$

where the symbol tilde written above the various quantities of eq. 2.48 is used to indicate that such quantity is projected on a given subspace. In more practical terms, the trajectory is computed as full dimensional, and later the system is divided in subspaces to compute the spectrum.

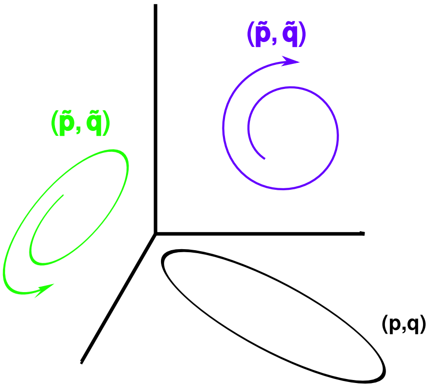

Fig. 2.2 Pictorial representation of the concept behind the DC SC IVR, where the full trajectory (black line) is used to generate a reduced dynamics in the projected subspaces (green and violet line)

This means that the coherent state overlap is no more an F-dimensional product over the entire system DoF but rather an M-dimensional one, which if chosen small enough has lower probabilities to have neglectable values which will cause the spectra to be too noisy or with spurious signals. Another feature of the DC SC IVR that allows for the computation of spectra for large molecular systems is that is no more necessary to compute the entire Hessian matrix for every step of the MD simulation since only blocks of the monodromy matrix are needed, more details about this will be given later in the manuscript. What instead is more tedious and bring an approximation with it, is the computation of the projected action. This is due to the fact that the potential is often non-separable. Ideally a projected potential should be able to reproduce in a rigorous way the reduced-dimensional dynamics and return the original potential when the subspace is substituted with the entire system. What is done instead, is to consider the potential as function of the reduced position $V(\tilde{\mathbf{q}}(t)) \approx V(\tilde{\mathbf{q}}(t);\mathbf{q}_{eq,F-M})$ and consider the positions of the other DoFs as a paramters. To this approximated potential a time dependent field is summed

$$\begin{aligned} V(\tilde{\mathbf{q}}(t)) &\approx V(\tilde{\mathbf{q}}(t);\mathbf{q}_{eq,F-M}) + \lambda(t) \; ; \\ \lambda(t) &= V(\tilde{\mathbf{q}}(t);\mathbf{q}_{F-M}(t)) - V(\tilde{\mathbf{q}}(t);\mathbf{q}_{eq,F-M}) - V(\tilde{\mathbf{q}}_{eq};\mathbf{q}_{F-M}(t)) \; . \end{aligned} \tag{2.49}$$

In this way the reduced-dimension dynamics will be exact when the potential is separable and will be approximate otherwise but still reliable. Equation 2.49 will be used to propagate the action after the full dimensional trajectory is computed. In order to do so, a single point calculation is done for every configuration explored along the trajectory upon substitution of the normal modes belonging to given subspace with their equilibrium values.

Now that the mathematical formalism of the DC SC IVR has been introduced, a few words must be spent on the computation protocol. As in all SC IVR methods the most important step of the whole procedure is the computation of the trajectory, which can be generated from eq. 2.44 for every normal mode. Along the full-dimensional trajectory the Hessian matrix of the potential is computed and stored for every step of the dynamics. The Hessian matrix is used not only to compute the elements of the monodromy matrix, but also to divide the system in subspaces. One of the most obvious methods that can be employed in order to do so is the so called "Hessian decomposition method", [73] in which the normal modes Hessian is averaged along the dynamics. The off-diagonal elements of the average second-derivative matrix are used as an estimate of the coupling between the different normal modes. Upon comparison to an arbitrary threshold the matrix is coarse-grained creating different subspaces. Even though this method has a high degree of arbitrariness and the choice of a given value of threshold can change dramatically the shape of the different subspaces, its application has been proven practical and effective. [130–133] Other subdivision methods requiring less arbitrary choices were also developed, one is the "Jacobi decomposition" in which the subspaces are chosen by selecting the combination of subspaces that more preserve the symplectic property of the Jacobian matrix. [73] Instead, another method is based on an evolutionary algorithm, [75] which uses laws similar to the ones of species-evolution to select the more "fitted" subspaces. On the other hand, while both methods are well formalized and require less human intervention in the whole procedure, their scalability with the increasing number of DoFs is not favorable. When it comes to medium/large molecular simulations, another step of the SC computational protocol that can be a problematic bottleneck, is the computation of the Hessian matrix. In fact, for medium sized molecules their evaluation along the ab-initio MD can be cumbersome, for this reason a series of algorithms has been developed to reduce the number of Hessian matrices computed along the trajectory. [74, 76] Although this two methods has made the calculation of DC SC IVR spectra on-the-fly even more practical and accessible, their applicability remains limited to medium-sized molecular systems, since their use require the computation and storage of the distance matrix between all of the DoFs. In fact, when moving to large molecular systems the process of storing whole matrices and also reading/writing files can become a further bottleneck. The DC SC IVR in this case allows to work in reduced dimensionality which means being able to speed up time and memory consuming procedures.

A useful procedure that opened the way to the computation of semiclassical spectra to condensed phase systems and solvated molecular systems [130, 134, 133] is the so called "gradient method". Since in these cases the computation and storage of every Hessian matrix along the MD simulation is not affordable in terms of both memory and time, only few uniformly distributed along the trajectory are computed and stored, the gradients instead are stored for every MD step. The calculated second derivatives are used to decide the subspaces according to the Hessian decomposition method. Once the subspaces of interest are defined a partial Hessian matrix containg only the blocks of the desired normal modes will be calculated, this is obtained by finite difference of the gradients considering only the displacement of the subspaces.

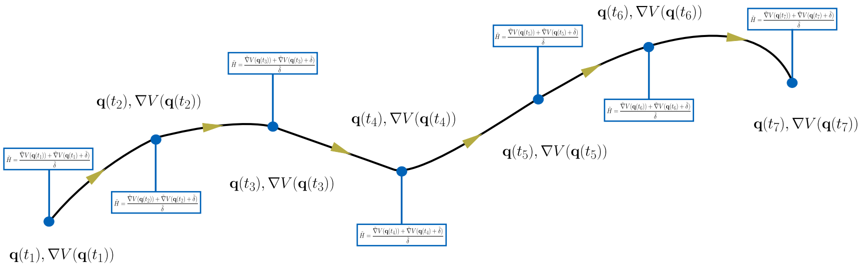

Fig. 2.3 Pictorial representation of the gradient method in which at every step of the trajectory (black line), positions and gradients are stored. To calculate the partial Hessian $\tilde{H}$ the gradient of the displaced geometry $\mathbf{q}+\tilde{\delta}$ is also evaluated, where $\tilde{\delta}$ is the partial displacement vector which is non-null only for the normal modes of interest.

It has to be pointed out also, that the use of the gradient method can be another source of error if the displacement factor ($\tilde{\delta}$) is chosen too big or too small. Another thing to notice, is that in order to limit computational overheads the single displacement formula with the gradients has been employed in the computation of the second derivatives. Therefore an error proportional to $\mathcal{O}\left(\tilde{\delta}^2\right)$ must be expected.

2.4 Classical vibrational density of states

A classical analog of equation 2.30 is given by the Fourier transform of the momentum autocorrelation function [135, 136]

$$I(\omega) = \frac{\Re}{2\pi} \int_{\mathbb{R}} dt \; e^{i\omega t} \left\langle \mathbf{p}(0)\mathbf{p}(t) \right\rangle \;, \tag{2.50}$$

where the quantity $C_{\mathbf{pp}}(t) = \langle \mathbf{p}(0)\mathbf{p}(t) \rangle$ is the classical autocorrelation function which can be calculated from MD simulations in a given ensemble. As done with the SC IVR, the $C_{\mathbf{pp}}(t)$ can be calculated as Monte Carlo integral over the initial conditions

$$C_{\mathbf{pp}}(t) = \iint d\mathbf{p}(0) d\mathbf{q}(0) \; \rho(\mathbf{p}(0), \mathbf{q}(0)) \mathbf{p}^T(0) \mathbf{p}(t) \;, \tag{2.51}$$

where $\rho(\mathbf{p}(0),\mathbf{q}(0))$ is the phase-space probability distribution of the chosen ensemble. Convergence of eq. 2.51 is not usually problematic, though a long sampling time is usually required in order to make the power spectrum (eq. 2.50) more clean as possible from noise and spurious signals. On the other hand, running long trajectories in the field of vibrational spectroscopies will cause to make the energy flow from the high-energy modes to lower energy modes (ZPE leakage), and eventually with even longer trajectories rotations and translations will be activated too. In more practical terms this means that the computed spectrum could become too crowded or even noisy due to the presence of undesired ro-vibrational features. To overcome this issue equation 2.35 can be exploited also for eq. 2.50

$$I(\omega) = \frac{1}{2\pi \mathrm{T}} \iint d\mathbf{p}(0)d\mathbf{q}(0)\ \rho(\mathbf{p}(0),\mathbf{q}(0)\ \int_{\mathbb{R}} dt\ e^{i\omega t} \int_0^{\mathrm{T}} dt'\ \mathbf{p}(t')\mathbf{p}(t'+t)\ . \tag{2.52}$$

The integrands in dt and dt' being functions of time can be rewritten as their inverse Fourier transform

$$\begin{aligned} \mathbf{p}(t') &= \frac{1}{2\pi} \int_{\mathbb{R}} d\omega' e^{-i\omega' t'} \tilde{\mathbf{p}}(\omega') \\ \mathbf{p}(t'+t) &= \frac{1}{2\pi} \int_{\mathbb{R}} d\omega'' e^{-i\omega''(t'+t)} \tilde{\mathbf{p}}(\omega'') \end{aligned} , \tag{2.53}$$

by substituting the identities of eq. 2.53 into eq. 2.52 and exploiting the definition of Dirac's delta through the Fourier transform, it is possible to obtain

$$\begin{aligned} I(\omega) =& \frac{1}{2\pi \mathrm{T}} \iint d\mathbf{p}(0)d\mathbf{q}(0)\ \rho(\mathbf{p}(0),\mathbf{q}(0)) \\ & \times \int_0^{\mathrm{T}} dt' \int_{\mathbb{R}} d\omega'\ e^{-i(\omega+\omega')t'} \tilde{\mathbf{p}}^T(\omega')\tilde{\mathbf{p}}(\omega)\ . \end{aligned} \tag{2.54}$$

By considering the limit in which T → $+\infty$ and by exploiting the parity property for which $\delta(-\omega-\omega') = \delta(\omega+\omega')$, eq. 2.54 can be rewritten as

$$I(\omega) = \frac{1}{2\mathrm{T}} \iint d\mathbf{p}(0)d\mathbf{q}(0)\ \rho(\mathbf{p}(0),\mathbf{q}(0))\tilde{\mathbf{p}}^T(\omega)\tilde{\mathbf{p}}(-\omega)\ . \tag{2.55}$$

Moreover, since $\tilde{\mathbf{p}}$ is a real quantity, it has to hold the following identity $\tilde{\mathbf{p}}(-\omega) = \tilde{\mathbf{p}}^*(\omega)$

$$\begin{aligned} I(\omega) &= \iint d\mathbf{p}(0)d\mathbf{q}(0)\ \rho(\mathbf{p}(0),\mathbf{q}(0))\frac{1}{2\mathrm{T}}\left|\tilde{\mathbf{p}}(\omega)\right|^2 \\ &\approx \iint d\mathbf{p}(0)d\mathbf{q}(0)\ \rho(\mathbf{p}(0),\mathbf{q}(0))\frac{1}{2\mathrm{T}}\left|\int_0^{\mathrm{T}} dt\ e^{i\omega t}\mathbf{p}(t)\right|^2 . \end{aligned} \tag{2.56}$$

Equation 2.56 can be considered as a classical equivalent of eq. 2.40. Its application is very much more straightforward then the TA SC IVR and also convergence is easier to reach. Moreover, when **p** is a normal-mode momentum equation 2.56 can be divisible in an exact way. This means that partial spectra of every normal mode can be obtained without the need of considering projected potentials. On the other hand, moving to a classical framework has also some important downsides. The most obvious regards the fact the classical MD alone is not able to account for NQEs, which in some cases were proven do be necessary. [43, 132] Another problem regards the fact that classical MD suffers from the aforementioned problem of ZPE-leakage. [137] Finally, classical spectroscopy methods strongly depends from initial conditions of the trajectory, this theme will be treated in the following chapter. [84] Therefore, the classical vDOS should be considered a practical and reliable tool only in certain conditions. In particular, a successful approach that was observed to be accurate in the classical limit is the Quasi-Classical Trajectory (QCT).[138–143] The main idea within the QCT approach is to initiate classical trajectories from "quantum" initial conditions as the ones of eq. 2.44. In this way, to some extent quantum effects such as ZPE are considered and the reliability of the vDOS is improved.

While it could be possible to argue that the QCT is not a "classical" approach to spectroscopy, it should be also observed that considering trajectories with energy below the ZPE has actually low physical meaning when trying to estimate vibrational frequencies.

2.5 Semiclassical nonadiabatic dynamics

It should be clear from the previous sections that since semiclassical molecular dynamics is based on classical MD its employment is usually limited to the Born-Oppenheimer approximation. On the other hand, many interesting chemical processes are observed to happen at conical intersections. [90, 144–148] Therefore, during the last years a large amount of methods, both for electronic structure and dynamics, has been developed in order to improve our comprehension on the matter. [88, 89, 149–154] In particular, the only methods that are compatible with SC dynamics are those that reduce the problem of nonadiabatic dynamics to a trajectory propagation, such as, Surface-Hopping [155] which uses stochastic jumps from BO surfaces to emulate the wavepacket bifurcation or Ehrenfest dynamics which uses an average potential of all the considered electronic states. Another viable option to extend semiclassical dynamics to the nonadiabatic regime are the "mapping" methods. The concept of mapping was first introduced by a pivotal work by H. D. Meyer and W. H. Miller. [91] The main idea is to consider a general diabatic potentials in a moving frame

$$\hat{H}_{el}(\mathbf{R}(t),t) = \sum_{l,m}^{N} \big|l\big\rangle V_{lm}(\mathbf{R}(t)) \big\langle m\big| \,, \tag{2.57}$$

where $\mathbf{R}$ is the nuclear coordinate, and $\left\{\big|l\big\rangle\right\}_1^N$ are the elements of the diabatic basis. By considering the electronic TDSE

$$\big|\dot{\psi}(t)\big\rangle = -\frac{i}{\hbar}\hat{H}_{el}\big|\psi(t)\big\rangle \,, \tag{2.58}$$

where $\psi(t) = \sum_l^N a_l(t)\big|l\big\rangle$, equation 2.58 can be rewritten as system of N ordinary-differential equations (ODE)

$$\dot{a}_l(t) = -\frac{i}{\hbar}\sum_{m=1}^{N} V_{lm}(\mathbf{R}(t))a_m(t) \,. \tag{2.59}$$

The novelty introduced by Meyer and Miller lies in rewriting the expansion coefficient $a_m(t) \in \mathbb{C}$ as function of two real continuous functions of time $\{\mathbf{n}(t), \mathbf{q}(t)\}$

$$a_m(t) = \sqrt{n_m(t)}e^{-\frac{i}{\hbar}q_m(t)} \,. \tag{2.60}$$

which can be thought as action-angle variables in the Argand-Gauss plane. At first sight eq. 2.59 seem to be more complicated when using eq. 2.60. Though, now the electronic Hamiltonian depends only from real continuous variables

$(\hat{H}_{el}(\mathbf{n}(t),\mathbf{q}(t),\mathbf{R}(t)))$. Moreover, the electronic Hamiltonian operator can be rewritten as a classical electronic Hamiltonian function

$$\begin{aligned} H_{el}(\mathbf{n}(t),\mathbf{q}(t),\mathbf{R}(t)) =& \langle \psi(t) \big| \hat{H}_{el}(\mathbf{R}(t),t) \big| \psi(t) \rangle \\ =& \sum_{l,m}^{N} \sqrt{n_l(t) n_m(t)} e^{-\frac{i}{\hbar}(q_m(t)-q_l(t))} V_{lm}(\mathbf{R}(t)) \ . \end{aligned} \tag{2.61}$$

The main result obtained from this mapping procedure is that the action-angle variables when rewritten in a classical Hamiltonian as in eq. 2.61, will obey classical Hamilton equations of motion. This means that the N-dimensional system of complex ODEs is now a $2N$-dimensional system of real differential equations.

A similar concept is the one proposed later by G. Stock and M. Thoss, [92] in which the idea is to map the N-state electronic system into a system of N coupled harmonic oscillators

$$\begin{aligned} \big|l\big\rangle\big\langle m\big| &\mapsto \hat{a}_l^{\dagger}\hat{a}_m \\ \big|l\big\rangle &\mapsto \big|0_1 \ldots 1_l \ldots 0_N\big\rangle \end{aligned} \ . \tag{2.62}$$

Where $\hat{a}_l^{\dagger}$ and $\hat{a}_m$ are the bosonic annihilation and creation operators which hold the usual commutation relation $\left[\hat{a}_m, \hat{a}_l^{\dagger}\right] = \delta_{ml}$, and

$$\langle \mathbf{y} | 0_1 \ldots 1_l \ldots 0_N \rangle = \langle \mathbf{y} | 1_l, \mathbf{0} \rangle = \left(\frac{1}{\pi}\right)^{\frac{N}{4}} \left[\sqrt{2} y_l \prod_{m=1}^{N} e^{-\frac{1}{2}\mathbf{y}^T\mathbf{y}}\right] \ . \tag{2.63}$$

The mapping-basis is usually referred as the Singly-Excited Oscillator (SEO) basis. It is easy to observe that the mapping operators in eq. 2.62 preserve the commutation relations, but represent the identity only in the case where the oscillator subspace is restricted only to single mode excitation.

The mapping relations in eq. 2.62 can be substituted in the electronic Hamiltonian in eq. 2.57

$$\hat{H}_{el} = \sum_{l,m}^{N} \hat{a}_l^{\dagger} V_{lm}(\mathbf{R}(t)) \hat{a}_m \ , \tag{2.64}$$

since the electronic operator are being mapped in the physical space of the harmonic oscillator, the creation and annihilation operators can be written in function of the position ($\hat{x}_m$) and momentum operator ($\hat{p}_m$)

$$\begin{cases} \hat{a}_m = & \frac{\hat{x}_m + i\hat{p}_m}{\sqrt{2}} \\ \hat{a}_m^{\dagger} = & \frac{\hat{x}_m - i\hat{p}_m}{\sqrt{2}} \end{cases} . \tag{2.65}$$

By using the operator identities in eq. 2.65 in the mapped electronic Hamiltonian in eq. 2.64

$$\begin{aligned} \hat{H}_{el} =& \sum_{l,m}^{N} \frac{1}{2} \left(\hat{x}_l - i\hat{p}_l\right) V_{lm}(\mathbf{R}(t)) \left(\hat{x}_m + i\hat{p}_m\right) \\ =& \sum_{l,m}^{N} \frac{1}{2} \left(\hat{x}_l \hat{x}_m + \hat{p}_l \hat{p}_m - \delta_{lm}\right) V_{lm}(\mathbf{R}(t)) \ , \end{aligned} \tag{2.66}$$

it is easy to notice that the mapped Hamiltonian in eq. 2.66 has a well known classical analog

$$\begin{aligned} H(\mathbf{R}(t), \mathbf{p}(t), \mathbf{x}(t)) =& \sum_{l,m} \frac{1}{2} \left(x_l(t) x_m(t) + p_l(t) p_m((t) - \delta_{lm}\right) V_{lm}(\mathbf{R}(t)) \\ =& \frac{1}{2} \mathbf{x}^T(t) \mathbb{V}(\mathbf{R}(t)) \mathbf{x}(t) + \frac{1}{2} \mathbf{p}^T(t) \mathbb{V}(\mathbf{R}(t)) \mathbf{p}(t) - \frac{1}{2} \mathrm{Tr}\left[\mathbb{V}(\mathbf{R}(t))\right] \ . \end{aligned} \tag{2.67}$$

Eventually, in order to simulate vibronic systems the nuclear kinetic energy can be added to the Meyer-Miller-Stock-Thoss (MMST) Hamiltonian

$$\begin{aligned}H(\mathbf{P}(t),\mathbf{R}(t),\mathbf{R}(t),\mathbf{p}(t),\mathbf{x}(t)) = &\sum_{J=1}^{F}\frac{P_J^2(t)}{2M_J}+V_0(\mathbf{R})\\ &+\frac{1}{2}\mathbf{x}^T(t)\mathbb{V}(\mathbf{R}(t))\mathbf{x}(t)+\frac{1}{2}\mathbf{p}^T(t)\mathbb{V}(\mathbf{R}(t))\mathbf{p}(t)\\ &-\frac{1}{2}\mathrm{Tr}\left[\mathbb{V}(\mathbf{R}(t))\right]\ .\end{aligned} \tag{2.68}$$

Where $\mathbf{P}$ is the conjugate momentum to the nuclear coordinate and $V_0(\mathbf{R})$ is a state independent potential.

It is possible to observe that even if the fundamental formulation of the mapping proposed by Meyer and Miller is different from the one proposed by Stock and Thoss, the mapped Hamiltonian of eq. 2.67 and 2.61 are interchangeable by using a canonical transformation between cartesian and action-angle variables

$$\begin{cases} x_l = & \sqrt{2n_l+1}\cos(q_l) \\ p_l = & \sqrt{2n_l+1}\sin(q_l) \end{cases} . \tag{2.69}$$

Also, both mapping methods allows to estimate in a classical way the elements of the electronic density matrix, in particular the populations of a given state m according to the Stock-Thoss mapping is given by

$$\rho_{mm} = n_m = \frac{1}{2}\left(x_m^2+p_m^2-1\right)\ . \tag{2.70}$$

This last observation allows to make a further observation on eq. 2.68. In particular, the mapping hamiltonian can be rewritten as

$$\begin{aligned}H(\mathbf{P}(t),\mathbf{R}(t),\mathbf{p}(t),\mathbf{x}(t)) = &\sum_{J=1}^{F}\frac{P_J^2}{2M_J}\\ &+\sum_{l}^{N}V_{ll}(\mathbf{R}(t))\rho_{ll}(t)+\sum_{l\neq m}^{N}\left(x_l x_m+p_l p_m\right)V_{lm}(\mathbf{R}(t))\ ,\end{aligned} \tag{2.71}$$

which means that the dynamics generated by the MMST Hamiltonian are run on average potentials weighted by the electronic population. This approach may seem similar to Ehrenfest dynamics, although a substantial difference comes from the last term of eq. 2.68, which is sometimes referred as the "electronic ZPE". [156–159] As was already observed by Meyer and Miller in the early formulation of the mapping method, classical dynamics suffers from ZPE-leakage which instead is prohibited in the true quantum dynamics of both electron and nuclei. To mitigate this issue, Stock and Muller [160] proposed to add an arbitrary parameter γ to the state independent part of the Hamiltonian in eq. 2.68

$$\begin{aligned} H(\mathbf{P}(t),\mathbf{R}(t),\mathbf{R}(t),\mathbf{p}(t),\mathbf{x}(t)) = & \sum_{J=1}^{F} \frac{P_J^2}{2M_J} \\ & + \frac{1}{2}\mathbf{x}^T(t)\mathbb{V}(\mathbf{R}(t))\mathbf{x}(t) + \frac{1}{2}\mathbf{p}^T(t)\mathbb{V}(\mathbf{R}(t))\mathbf{p}(t) \\ & - \frac{\gamma}{2}\mathrm{Tr}\left[\mathbb{V}(\mathbf{R}(t))\right] \ . \end{aligned} \tag{2.72}$$

In this way, different families of mapping methods can be defined. Where $\gamma = 1$ returns the MMST mapping and $\gamma = 0$ corresponds to the Ehrenfest dynamics. Stock and Muller initially tuned the value of γ to avoid the diabatic populations from becoming negative. [160] Later, Cotton and Miller [161] found a partial justification on a value of $\gamma = \sqrt{3} - 1$ which was more rigorously corroborated by Runeson and Richardson by applying Stratonovich-Weyl transformations on the spin-mapped Hamiltonian. From now on, during this manuscript this parameter will be chosen as $\gamma = 1$ unless it is explicitly specified differently.

2.5.1 Symplectic integration of the MMST Hamiltonian

It is easy to observe that the MMST Hamiltonian in eq. 2.68 is not a simple collisional Hamiltonian composed of the potential term that depends only from the position and the kinetic term that depends only from the conjugated momentum of the position. Due to its non separability, integrating eq. 2.68 by using conventional symplectic integrators will lead to violation of symplectic properties such as energy conservation or unitarity of the determinant of the monodromy matrix ($|M(t)| = 1$). To overcome this issue, different algorithms were developed.[162, 163] In particular, in a recent work by Cook. et. al. [164] it was for the first time highlited how algorithms such as the Split-Liouvillian [165] by Richardson et. al. and the Degenerate Eigenvalue by A. Kelly at. al. [166] are partially able to satisfy the Liouville theorem but not the symplecticity criterion $\sqrt{\sum_{ij}\left|\left(M^T(t)\mathbf{J}M(t)\right)_{ij} - J_{ij}\right|^2} = 0$. Instead, the Momentum Integral over Time (MINT) [53] devloped by Church et. al. was proven both theoretically and practically to be symplectic. In the case of the MINT algorithm the Hamiltonian is is divided in two sub-Hamiltonians, which if evolved in a symplectic way will recover the true symplectic evolution of the full Hamiltonian

$$
\begin{aligned}
H = (\mathbf{P},\mathbf{R},\mathbf{p},\mathbf{x}) = & \quad H_1(\mathbf{P}) + H_2(\mathbf{R},\mathbf{p},\mathbf{x}) \,, && (2.73)\\
H_1(\mathbf{P}) = & \quad \tfrac{1}{2}\mathbf{P}^T\mathbf{M}^{-1}\mathbf{P} \,, && (2.74)\\
H_2(\mathbf{R},\mathbf{p},\mathbf{x}) = & \quad V_0(\mathbf{R}) + \tfrac{1}{2}\mathbf{p}^T\mathbb{V}(\mathbf{R})\mathbf{p} + \tfrac{1}{2}\mathbf{x}^T\mathbb{V}(\mathbf{R})\mathbf{x} - \tfrac{1}{2}\mathrm{Tr}\left[\mathbb{V}(\mathbf{R})\right] \,. && (2.75)
\end{aligned}
$$

Where $\mathbf{M}$ is the mass matrix which is assumed to be diagonal. The subdivision of the full Hamiltonian allows to write a symplectic map such that $\Phi_{H,t}(\mathbf{z}_0) = \mathbf{z}_t$, where $\mathbf{z} = (\mathbf{P},\mathbf{R},\mathbf{p},\mathbf{x})$, as composition of sub-symplectic maps

$$
\Phi_{H,\delta t} = \Phi_{H_1,\delta t/2} \circ \Phi_{H_2,\delta t} \circ \Phi_{H_1,\delta t/2} \,. \tag{2.76}
$$

Evolution under H_1 is analogous to the evolution of a free particle

$$
\begin{cases}
\dot{\mathbf{R}} = & \frac{\partial H_1}{\partial \mathbf{P}} = \mathbf{M}^{-1}\mathbf{P} \\
\dot{\mathbf{P}} = & -\frac{\partial H_1}{\partial \mathbf{R}} = 0 \\
\dot{\mathbf{x}} = & \frac{\partial H_1}{\partial \mathbf{p}} = 0 \\
\dot{\mathbf{p}} = & -\frac{\partial H_1}{\partial \mathbf{x}} = 0
\end{cases} \,, \tag{2.77}
$$

which means that under H_1 all of the phase space variables but the nuclear position will remain constant

$$
\mathbf{R}\left(t + \frac{\delta t}{2}\right) = \mathbf{R}(t) + \mathbf{M}^{-1}\mathbf{P}(t)\frac{\delta t}{2} \,. \tag{2.78}
$$

Instead, the evolution under H_2 is clearly more complicated

$$\begin{cases} \dot{\mathbf{R}} = & \frac{\partial H_2}{\partial \mathbf{P}} = 0 \\ \dot{P}_k = & -\frac{\partial H_2}{\partial R_k} = -\frac{\partial V_0}{\partial R_k}(\mathbf{R}) - \frac{1}{2}\left(\mathbf{x} - i\mathbf{p}\right)^T \frac{\partial \mathbb{V}(\mathbf{R})}{\partial R_k}\left(\mathbf{x} + i\mathbf{p}\right) + \frac{1}{2}\mathrm{Tr}\left[\frac{\partial \mathbb{V}(\mathbf{R})}{\partial R_k}\right] \\ \dot{\mathbf{x}} = & \frac{\partial H_2}{\partial \mathbf{p}} = \mathbb{V}(\mathbf{R})\mathbf{p} \\ \dot{\mathbf{p}} = & -\frac{\partial H_2}{\partial \mathbf{x}} = \mathbb{V}(\mathbf{R})\mathbf{x} \end{cases} . \tag{2.79}$$

Though, it is possible to observe that since **R** is fixed uder H_2 and that **x** and **p** do not depend on **P**. Equations 2.79 can be solved in first instance for the electronic variables between t and $t + \delta t$, and then inserted into the equation of the nuclear momentum. Solution of the electronic equations of motion is straightforward

$$\begin{cases} \mathbf{x}(t+\delta t) = & \cos\left(\delta t \mathbb{V}(\mathbf{R})\right)\mathbf{x}(t) + \sin\left(\delta t \mathbb{V}(\mathbf{R})\right)\mathbf{p}(t) \\ \mathbf{p}(t+\delta t) = & \cos\left(\delta t \mathbb{V}(\mathbf{R})\right)\mathbf{p}(t) - \sin\left(\delta t \mathbb{V}(\mathbf{R})\right)\mathbf{x}(t) \end{cases} , \tag{2.80}$$

meaning that the propagator of $(\mathbf{x} + i\mathbf{p})$ is given by

$$\left(\mathbf{x}(t+\delta t) + i\mathbf{p}(t+\delta t)\right) = e^{-i\delta t \mathbb{V}(\mathbf{R})}\left(\mathbf{x}(t) + i\mathbf{p}(t)\right) \ , \tag{2.81}$$

equation 2.81 can be inserted into the equation 2.79 for the nuclear momentum and time integrated

$$\begin{aligned} P_k(t+\delta t) =& P_k(t) - \frac{\partial V_0}{\partial R_k}(\mathbf{R})\delta t \\ & - \frac{1}{2}\int_t^{t+\delta t} d\tau \left[\left(\mathbf{x}(t) - i\mathbf{p}(t)\right)^T e^{i\tau \mathbb{V}(\mathbf{R})} \frac{\partial \mathbb{V}(\mathbf{R})}{\partial R_k} e^{-i\tau \mathbb{V}(\mathbf{R})}\left(\mathbf{x}(t) + i\mathbf{p}(t)\right)\right] \\ & + \frac{1}{2}\mathrm{Tr}\left[\frac{\partial \mathbb{V}(\mathbf{R})}{\partial R_k}\right]\delta t \ . \end{aligned} \tag{2.82}$$

The time integral over the momentum is solvable analytically only in the case where $\mathbb{V}$ is diagonal. This means that is necessary to consider the relation occurring between the diabatic and adiabatic potential $(\Lambda(\mathbf{R}))$

$$\Lambda(\mathbf{R}) = \mathbb{S}^T(\mathbf{R})\mathbb{V}(\mathbf{R})\mathbb{S}(\mathbf{R}) \;, \tag{2.83}$$

where $\mathbb{S}$ is the eigenvector matrix which diagonalize the diabatic potential. To the relation in eq. 2.83 is subsequent also the trivial property

$$e^{-i\tau\mathbb{V}(\mathbf{R})} = \mathbb{S}(\mathbf{R})e^{-i\tau\Lambda(\mathbf{R})}\mathbb{S}^T(\mathbf{R}) \;, \tag{2.84}$$

which can be directly subsituited in eq. 2.82

$$\begin{aligned} P_k(t+\delta t) =& P_k(t) - \frac{\partial V_0}{\partial R_k}(\mathbf{R})\delta t \\ & -\frac{1}{2}\left(\mathbf{x}(t) - i\mathbf{p}(t)\right)^T \mathbb{S}(\mathbf{R}) \\ & \times \int_t^{t+\delta t} d\tau \; e^{i\tau\Lambda(\mathbf{R})}\mathbb{W}_k(\mathbf{R})e^{-i\tau\Lambda(\mathbf{R})} \\ & \times \mathbb{S}^T(\mathbf{R})\left(\mathbf{x}(t) + i\mathbf{p}(t)\right) + \frac{1}{2}\mathrm{Tr}\left[\frac{\partial \mathbb{V}(\mathbf{R})}{\partial R_k}\right] \\ \mathbb{W}_k(\mathbf{R}) =& \mathbb{S}^T(\mathbf{R})\frac{\partial \mathbb{V}(\mathbf{R})}{\partial R_k}\mathbb{S}(\mathbf{R}) \;. \end{aligned} \tag{2.85}$$

Equation 2.85 can be solved analytically

$$\int_t^{t+\delta t} d\tau \; e^{i\tau\Lambda(\mathbf{R})}\mathbb{W}_k(\mathbf{R})e^{-i\tau\Lambda(\mathbf{R})} = \Gamma_k(\mathbf{R}) + i\Omega_k(\mathbf{R}) \;, \tag{2.86}$$

where

$$(\Gamma_k)_{lm} = \begin{cases} (\mathbb{W}_k)_{lm}\,\delta t & m = n \\ \frac{(\mathbb{W}_k)_{lm}}{\lambda_{lm}}\sin\left(\lambda_{lm}\delta t\right) & m \neq n \end{cases} \tag{2.87}$$

$$(\Omega_k)_{lm} = \begin{cases} 0 & m = n \\ \frac{(\mathbb{W}_k)_{lm}}{\lambda_{lm}}\left[1 - \cos\left(\lambda_{lm}\delta t\right)\right] & m \neq n \end{cases} \;, \tag{2.88}$$

in which the Γ_k and Ω_k matrices are respectively symmetric and skew-symmetric matrices solution of the integral in eq. 2.86 and the terms $\lambda_{lm} = (\Lambda)_{ll} - (\Lambda)_{mm}$ are defined as the differences between the elements of the adiabatic potentials. Upon its substitution in eq. 2.85 and by defining the $\mathbb{E}_k(\mathbf{R})$ and $\mathbb{F}_k(\mathbf{R})$ as

$$\begin{aligned} \mathbb{E}_k(\mathbf{R}) =& \mathbb{S}(\mathbf{R})\Gamma_k(\mathbf{R})\mathbb{S}^T(\mathbf{R}) \\ \mathbb{F}_k(\mathbf{R}) =& \mathbb{S}(\mathbf{R})\Omega_k(\mathbf{R})\mathbb{S}^T(\mathbf{R}) \end{aligned} , \tag{2.89}$$

it is possible to obtain the integration rule also for the nuclear momentum

$$\begin{aligned} P_k(t+\delta t) =& P_k(t) - \frac{\partial V_0}{\partial R_k}(\mathbf{R})\delta t \\ & - \frac{1}{2}\left[\mathbf{x}^T(t)\mathbb{E}_k(\mathbf{R})\mathbf{x}(t) + \mathbf{p}^T(t)\mathbb{E}_k(\mathbf{R})\mathbf{p}(t) - 2\mathbf{x}^T(t)\mathbb{F}_k(\mathbf{R})\mathbf{p}(t)\right] \\ & + \frac{1}{2}\mathrm{Tr}\left[\frac{\partial \mathbb{V}(\mathbf{R})}{\partial R_k}\right]\delta t \; . \end{aligned} \tag{2.90}$$

Since eigenvector matrices are already being computed, eqs. 2.80 can be computed using an analogous property to the one of eq. 2.84 avoiding series expansion

$$\begin{aligned} \mathbb{C}(\mathbf{R}) =& \mathbb{S}\cos\left(\delta t\Lambda(\mathbf{R})\right)\mathbb{S}^T(\mathbf{R}) = \cos\left(\delta t\mathbb{V}(\mathbf{R})\right) \\ \mathbb{D}(\mathbf{R}) =& \mathbb{S}\sin\left(\delta t\Lambda(\mathbf{R})\right)\mathbb{S}^T(\mathbf{R}) = \sin\left(\delta t\mathbb{V}(\mathbf{R})\right) \end{aligned} . \tag{2.91}$$

Therefore, electronic variables integration rules can be rewritten as

$$\begin{aligned} \mathbf{x}(t+\delta t) =& \mathbb{C}(\mathbf{R})\mathbf{x}(t) + \mathbb{D}(\mathbf{R})\mathbf{p}(t) \\ \mathbf{p}(t+\delta t) =& \mathbb{C}(\mathbf{R})\mathbf{p}(t) - \mathbb{D}(\mathbf{R})\mathbf{x}(t) \end{aligned} . \tag{2.92}$$

While the time evolution of the phase-space variables proposed by Church et. al. [53] is able to preserve energy, the proposed method to evolve the monodromy matrix

$$M(t) = \begin{vmatrix} M_{PP}(t) & M_{Pp}(t) & M_{PR}(t) & M_{Px}(t) \\ M_{pP}(t) & M_{pp}(t) & M_{pR}(t) & M_{px}(t) \\ M_{RP}(t) & M_{Rp}(t) & M_{RR}(t) & M_{Rx}(t) \\ M_{xP}(t) & M_{xp}(t) & M_{xR}(t) & M_{xx}(t) \end{vmatrix} = \begin{vmatrix} \mathbb{M}_{\pi\pi}(t) & \mathbb{M}_{\pi\xi}(t) \\ \mathbb{M}_{\xi\pi}(t) & \mathbb{M}_{\xi\xi}(t) \end{vmatrix} , \tag{2.93}$$

results to be approximated on long timescales and multidimensional problems. This is due to the fact that in ref. [53] and [164] the evolution of $M(t)$ under H_1 is assumed independent from the evolution under H_2

$$M(t+\delta t) = \left[M_{H_1}^T \left(t + \frac{\delta t}{2} \right) M_{H_2}(t+\delta t) M_{H_1} \left(t + \frac{\delta t}{2} \right) \right]^T M(t) \, , \tag{2.94}$$

where [1]

$$\begin{aligned} M_{H_1}\left(t + \frac{\delta t}{2} \right) &= \begin{vmatrix} \mathbb{1} & 0 & \mathbb{O} & 0 \\ 0^T & \mathbf{1} & 0^T & \mathbf{0} \\ M^{-1}\frac{\delta t}{2} & 0 & \mathbb{1} & 0 \\ 0^T & \mathbf{0} & 0^T & \mathbf{1} \end{vmatrix} \\ M_{H_2}(t+\delta t) &= \begin{vmatrix} \mathbb{1} & \mathbf{e} & \frac{\partial \mathbf{P}}{\partial \mathbf{R}} & \mathbf{a} \\ 0^T & \mathbb{C} & \mathbf{f} & -\mathbb{D} \\ & 0 & \mathbb{1} & 0 \\ 0^T & \mathbb{D} & \mathbf{g} & \mathbb{C} \end{vmatrix} \end{aligned} , \tag{2.95}$$

in which the terms $\mathbf{e}, \mathbf{a}$, $\mathbf{f}$, $\mathbf{g}$ and $\frac{\partial \mathbf{P}}{\partial \mathbf{R}}$ are defined as

---

[1] $\mathbb{1}$ is the $F \times F$ identity matrix, 0 is the $F \times N$ null matrix, $\mathbb{O}$ is the $F \times F$ null matrix , $\mathbf{1}$ is the $N \times N$ identity matrix and $\mathbf{0}$ is the $N \times N$ identity matrix

$$\begin{aligned}
\mathbf{e} =& -\left[\mathbf{p}^T(t)\mathbb{E}-\mathbf{x}^T(t)\mathbb{F}\right]\\
\mathbf{a} =& -\left[\mathbf{x}^T(t)\mathbb{E}+\mathbf{p}^T(t)\mathbb{F}\right]\\
\mathbf{f} =& \mathbf{p}^T(t)\frac{\partial\mathbb{C}}{\partial\mathbf{R}}-\mathbf{x}^T(t)\frac{\partial\mathbb{C}}{\partial\mathbf{R}}\\
\mathbf{g} =& \mathbf{x}^T(t)\frac{\partial\mathbb{C}}{\partial\mathbf{R}}+\mathbf{p}^T(t)\frac{\partial\mathbb{C}}{\partial\mathbf{R}} \qquad\qquad\qquad\qquad\qquad\qquad\qquad\qquad .\\
\frac{\partial\mathbf{P}}{\partial\mathbf{R}} =& -\frac{\partial^2 V_0(\mathbf{R})}{\partial\mathbf{R}^2}\delta t\\
& -\frac{1}{2}\left[\mathbf{x}^T(t)\frac{\partial\mathbb{E}}{\partial\mathbf{R}}\mathbf{x}(t)+\mathbf{p}^T(t)\frac{\partial\mathbb{E}}{\partial\mathbf{R}}\mathbf{p}(t)-2\mathbf{x}^T(t)\frac{\partial\mathbb{F}}{\partial\mathbf{R}}\mathbf{p}(t)\right]+\frac{1}{2}\mathrm{Tr}\left[\frac{\partial^2\mathbb{V}}{\partial\mathbf{R}^2}\right]\delta t
\end{aligned} \tag{2.96}$$

Equation 2.94 is exact only in the case where the Liouville parentheses of the sub-Hamiltonians are null ($\{H_1, H_2\} = 0$), instead in this case since the H_1 and H_2 are not invariant one to each other, eq. 2.42 must be used in order to evolve the monodromy matrix. In this manuscript to propagate the Monodromy matrix the subdivision of the Hamiltonian is used to define

$$\begin{cases} \dot{M}_{H_1}(t) = & \mathbf{J}\frac{\partial^2 H_1}{\partial\mathbf{z}^2}(\mathbf{z})M_{H_1}(t)\\ \dot{M}_{H_2}(t) = & \mathbf{J}\frac{\partial^2 H_2}{\partial\mathbf{z}^2}(\mathbf{z})M_{H_2}(t) \end{cases}. \tag{2.97}$$

Where $\frac{\partial^2 H_1}{\partial\mathbf{z}^2}(\mathbf{z})$ and $\frac{\partial^2 H_2}{\partial\mathbf{z}^2}(\mathbf{z})$ are the Hessian matrices of the sub-Hamiltonians, defined as

$$\begin{aligned}
\frac{\partial^2 H_1}{\partial\mathbf{z}^2}(\mathbf{z}) =& \begin{vmatrix} M^{-1} & 0 & \mathbb{O} & 0\\ 0^T & \mathbf{0} & 0^T & \mathbf{0}\\ \mathbb{O} & 0^T & \mathbb{O} & 0\\ 0^T & \mathbf{0} & 0^T & \mathbf{0} \end{vmatrix}\\
\frac{\partial^2 H_2}{\partial\mathbf{z}^2}(\mathbf{z}) =& \begin{vmatrix} \mathbb{O} & 0 & \mathbb{O} & 0\\ 0^T & \mathbb{V}(\mathbf{R}) & \left(\frac{\partial^2 H_2(\mathbf{z}(t))}{\partial\mathbf{R}\partial\mathbf{p}}\right)^T & \mathbf{0}\\ \mathbb{O} & \frac{\partial^2 H_2(\mathbf{z}(t))}{\partial\mathbf{R}\partial\mathbf{p}} & \frac{\partial^2 H_2}{\partial\mathbf{R}^2} & \frac{\partial^2 H_2(\mathbf{z}(t))}{\partial\mathbf{R}\partial\mathbf{x}}\\ 0^T & \mathbf{0} & \left(\frac{\partial^2 H_2(\mathbf{z}(t))}{\partial\mathbf{R}\partial\mathbf{x}}\right)^T & \mathbb{V}(\mathbf{R}) \end{vmatrix}.
\end{aligned} \tag{2.98}$$

It is possible to observe that since the H_1 sub-Hamiltonian contains only the free particle term, the only non-null second derivative term is the momentum diagonal block, which corresponds to the inverse of the mass. Instead, the H_2 Hessian matrix is less sparse due to the presence of coupling terms between the nuclear coordinate and the electronic DoFs. In particular, by assuming the diabatic potential as symmetric, the mixed second derivatives matrices of H_2 between $\mathbf{R}$ and $\mathbf{x}, \mathbf{p}$ are of size $F \times N$ and defined as

$$\begin{aligned} \frac{\partial}{\partial R_J}\frac{\partial H_2}{\partial x_k} &= \sum_l^N \frac{\partial V_{kl}(\mathbf{R})}{\partial R_J} x_l = \left(\frac{\partial^2 H_2}{\partial \mathbf{R} \partial \mathbf{x}}\right)_{Jk} \\ \frac{\partial}{\partial R_J}\frac{\partial H_2}{\partial p_k} &= \sum_l^N \frac{\partial V_{kl}(\mathbf{R})}{\partial R_J} p_l = \left(\frac{\partial^2 H_2}{\partial \mathbf{R} \partial \mathbf{p}}\right)_{Jk} \end{aligned} . \tag{2.99}$$

By exploiting eqs. 2.97, it is easy to see that the equations of motion under H_1 are independent from the ones under H_2. This means that it is possible to solve initially the equations under H_1

$$\begin{cases} M_{RP}\left(t+\frac{\delta t}{2}\right) = & M_{RP}(t) + M^{-1} M_{PP}(t)\frac{\delta t}{2} \\ M_{Rp}\left(t+\frac{\delta t}{2}\right) = & M_{Rp}(t) + M^{-1} M_{Pp}(t)\frac{\delta t}{2} \\ M_{RR}\left(t+\frac{\delta t}{2}\right) = & M_{RR}(t) + M^{-1} M_{PR}(t)\frac{\delta t}{2} \\ M_{Rx}\left(t+\frac{\delta t}{2}\right) = & M_{Rx}(t) + M^{-1} M_{Px}(t)\frac{\delta t}{2} \end{cases} , \tag{2.100}$$

then the time evolved quantities can be used for the evolution under H_2. Clearly, since $\frac{\partial^2 H_2}{\partial \mathbf{z}^2}$ is less sparse, the evolution of the monodromy matrix under H_2 will be described by a system of sixteen coupled equations

$$\begin{cases}
\dot{M}_{PP}(t) = & -\frac{\partial^2 H_2}{\partial \mathbf{R}^2} M_{RP}(t) - \frac{\partial^2 H_2(\mathbf{z}(t))}{\partial \mathbf{R} \partial \mathbf{p}} M_{pP}(t) - \frac{\partial^2 H_2(\mathbf{z}(t))}{\partial \mathbf{R} \partial \mathbf{x}} M_{xP}(t) \\
\dot{M}_{Pp}(t) = & -\frac{\partial^2 H_2}{\partial \mathbf{R}^2} M_{Rp}(t) - \frac{\partial^2 H_2(\mathbf{z}(t))}{\partial \mathbf{R} \partial \mathbf{p}} M_{pp}(t) - \frac{\partial^2 H_2(\mathbf{z}(t))}{\partial \mathbf{R} \partial \mathbf{x}} M_{xp}(t) \\
\dot{M}_{PR}(t) = & -\frac{\partial^2 H_2}{\partial \mathbf{R}^2} M_{RR}(t) - \frac{\partial^2 H_2(\mathbf{z}(t))}{\partial \mathbf{R} \partial \mathbf{p}} M_{pR}(t) - \frac{\partial^2 H_2(\mathbf{z}(t))}{\partial \mathbf{R} \partial \mathbf{x}} M_{xR}(t) \\
\dot{M}_{Px}(t) = & -\frac{\partial^2 H_2}{\partial \mathbf{R}^2} M_{Rx}(t) - \frac{\partial^2 H_2(\mathbf{z}(t))}{\partial \mathbf{R} \partial \mathbf{p}} M_{px}(t) - \frac{\partial^2 H_2(\mathbf{z}(t))}{\partial \mathbf{R} \partial \mathbf{x}} M_{xx}(t) \\
\dot{M}_{pP}(t) = & -\mathbb{V}(\mathbf{R}) M_{xP}(t) - \left(\frac{\partial^2 H_2(\mathbf{z}(t))}{\partial \mathbf{R} \partial \mathbf{x}} \right)^T M_{RP}(t) \\
\dot{M}_{pp}(t) = & -\mathbb{V}(\mathbf{R}) M_{xp}(t) - \left(\frac{\partial^2 H_2(\mathbf{z}(t))}{\partial \mathbf{R} \partial \mathbf{x}} \right)^T M_{Rp}(t) \\
\dot{M}_{pR}(t) = & -\mathbb{V}(\mathbf{R}) M_{xR}(t) - \left(\frac{\partial^2 H_2(\mathbf{z}(t))}{\partial \mathbf{R} \partial \mathbf{x}} \right)^T M_{RR}(t) \\
\dot{M}_{px}(t) = & -\mathbb{V}(\mathbf{R}) M_{xx}(t) - \left(\frac{\partial^2 H_2(\mathbf{z}(t))}{\partial \mathbf{R} \partial \mathbf{x}} \right)^T M_{Rx}(t) \\
\dot{M}_{RP}(t) = & \mathbb{O} \\
\dot{M}_{Rp}(t) = & 0 \\
\dot{M}_{RR}(t) = & \mathbb{O} \\
\dot{M}_{Rx}(t) = & 0 \\
\dot{M}_{xP}(t) = & \mathbb{V}(\mathbf{R}) M_{pP}(t) + \left(\frac{\partial^2 H_2(\mathbf{z}(t))}{\partial \mathbf{R} \partial \mathbf{p}} \right)^T M_{RP}(t) \\
\dot{M}_{xp}(t) = & \mathbb{V}(\mathbf{R}) M_{pp}(t) + \left(\frac{\partial^2 H_2(\mathbf{z}(t))}{\partial \mathbf{R} \partial \mathbf{p}} \right)^T M_{Rp}(t) \\
\dot{M}_{xR}(t) = & \mathbb{V}(\mathbf{R}) M_{pR}(t) + \left(\frac{\partial^2 H_2(\mathbf{z}(t))}{\partial \mathbf{R} \partial \mathbf{p}} \right)^T M_{RR}(t) \\
\dot{M}_{xx}(t) = & \mathbb{V}(\mathbf{R}) M_{px}(t) + \left(\frac{\partial^2 H_2(\mathbf{z}(t))}{\partial \mathbf{R} \partial \mathbf{p}} \right)^T M_{Rx}(t)
\end{cases} . \tag{2.101}$$

To evolve the equations of motion of the monodromy matrix under H_2 in eq. 2.101 a finite difference scheme is employed. To maximize the accuracy of the algorithm it is necessary to consider the updates of the different quantities in the right order. In order to do so, it is possible to observe that the $\dot{M}_{Pj}(t)$ blocks do not depend from other elements of the monodromy under H_2, therefore they can be evolved similarly to eqs. 2.100. Also, since the $\dot{M}_{pj}(t)$ and $M_{xj}(t)$ blocks depends on each others only in couples, e.g. $\dot{M}_{pP}(t)$ depends from $M_{xP}(t)$ and vice-versa, and the second addend can be considered as a forcing term, it is possible to evolve the remaining two blocks in a Verlet-like way.

2.5.2 Semiclassical Nonadiabatic Vibronic Spectroscopy

The mapped Hamiltonian in eq. 2.68, maps the problem of propagating a wavepacket on two or more diabatic potential energy surfaces into a trajectory propagation problem. The employment of an improved version of the MINT algorithm allows also for long time propagation without occurring in nonphysical violation of symplectic properties. These two elements allows to expand the semiclassical IVR to the nonadiabatic (NA) regime. In particular, one interesting application regards the spectroscopy of systems where two or more electronic states are coupled [167–170] or Jahn-Teller conical conical intersections. [171, 172] Such application of the NA SC IVR was already proven successful in the case of the S_1-S_2 model potential of pyrazine. [173] Though, in that work by Thoss,Miller and Stock a cellularization smoothing procedure was applied to the survival amplitude [174] in order to improve the convergence of the HHKK propagator. Such procedure depends from arbitrary parameters and can bring very strong approximations. Therefore, during this manuscript a time averaged version of the absorption spectrum will be employed.

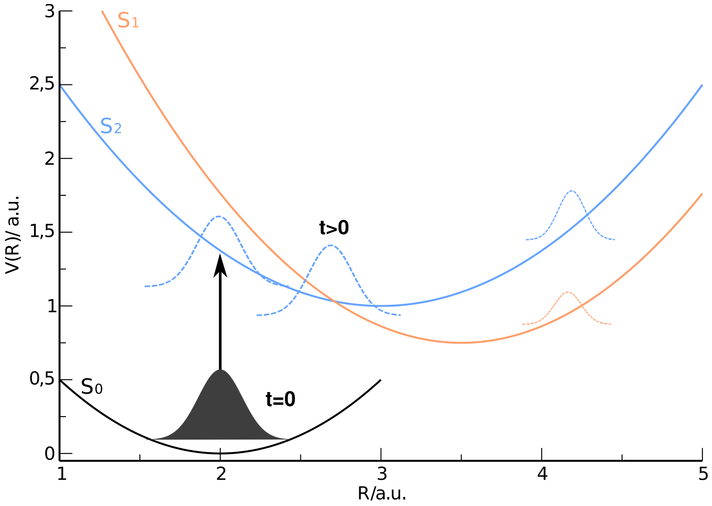

Fig. 2.4 Pictorial representation of the procedure used to compute the vibronic spectra

The physical process to be reproduced within this section is the photoabsorption of a system initially at the equilibrium in the vibronic ground state. After the absorption the system is vertically excited to one or more diabatically coupled resonant states. For pratical reasons, it is assumed that the exciting pulse is a simple δ-pulse that leaves no amplitude in the ground state.[175] Figure 2.4 schematically illustrates the process from the initial time ($t = 0$) in which takes place the excitation, to the propagation in the coupled excited resonant states.

Differently from the previous case, in this section the derivation of the semiclassical method is initiated by defining a general working formula for the absorption spectrum. In particular, by exploiting the time-dependent first-order perturbation theory, the photo-absorption cross section can be defined as the Fourier transfrom of the thermal dipole-autocorrelation function

$$\sigma_\beta(\boldsymbol{\varepsilon}, E) = \frac{E}{2\hbar^2 c \varepsilon_0} \Re \int_{\mathbb{R}} dt \; C^{\beta}_{\mu\mu}(\boldsymbol{\varepsilon}, t) e^{\frac{i}{\hbar}Et} \; , \tag{2.102}$$

where β is the Boltzmann temperature, $\boldsymbol{\varepsilon}$ is the unit polarization vector of the electric field and $C^{\beta}_{\mu\mu}$ is the thermal dipole-autocorrelation function

$$C^{\beta}_{\mu\mu}(\boldsymbol{\varepsilon}, t) = \mathrm{Tr}\left[\hat{\rho} e^{\frac{i}{\hbar}\hat{H}_0 t} \hat{\mu} e^{-\frac{i}{\hbar}\hat{\mathbf{H}}_d t} \hat{\mu}\right] \; . \tag{2.103}$$

In equation 2.103, $\hat{\rho}$ is the density matrix, $\hat{H}_0$ is the Hamiltonian of the ground state, $\hat{\mathbf{H}}_d$ is the diabatic Hamiltonian of the excited states and $\hat{\mu}$ is the dipole operator projected in the direction of the electric field ($\hat{\mu} = \boldsymbol{\varepsilon}^T \hat{\boldsymbol{\mu}}$). In the limit of the zero temperature approximation ($\beta \to +\infty$), the only populated state is the vibronic ground state

$$\hat{\rho} = \lim_{\beta \to +\infty} \frac{e^{-\beta \hat{H}_0}}{Z(\beta)} = \left|\psi_0\right\rangle\left\langle\psi_0\right| \; , \tag{2.104}$$

where $\left|\psi_0\right\rangle\left\langle\psi_0\right|$ is the projector to the vibronic ground state, $Z(\beta)$ is the partition function of the system and $e^{-\beta \hat{H}_0}$ is the Boltzmann operator. This approximation was also used by Lanzi et. al. (Ref. [63]) to calculate semiclassical IR spectra, and proved to be adequate for both molecular and model systems. In the future we don't exclude to implement finite temperature calculations which proved to be important in the computation of vibrationally resolved electronic spectra.[176, 177] It is possible to see that by applying eq. 2.104 to eq. 2.103 the dipole autocorrelation function becomes

$$\begin{aligned} C_{\mu\mu}(\boldsymbol{\varepsilon},t) \approx& \left\langle \psi_0 \middle| e^{\frac{i}{\hbar}\hat{H}_0 t} \hat{\boldsymbol{\mu}}_{0\leftarrow f} e^{-\frac{i}{\hbar}\hat{\mathbf{H}}_d t} \hat{\boldsymbol{\mu}}_{0\rightarrow f} \middle| \psi_0 \right\rangle \\ =& e^{\frac{i}{\hbar}E_0 t} \left\langle \psi_0 \middle| \hat{\boldsymbol{\mu}}_{0\leftarrow f} e^{-\frac{i}{\hbar}\hat{\mathbf{H}}_d t} \hat{\boldsymbol{\mu}}_{0\rightarrow f} \middle| \psi_0 \right\rangle \end{aligned} , \tag{2.105}$$

$\hat{H}_0$ is now the Hamiltonian of the vibronic ground state, such that $\hat{H}_0 \left| \psi_0 \right\rangle = E_0 \left| \psi_0 \right\rangle$ and $\hat{\boldsymbol{\mu}}_{0\leftarrow f}$ is the transition dipole vector between the ground state and the possible final states. The last considered approximation regarding the definition of the spectrum is the Condon approximation, which lifts the dependence of the transition-dipole from the nuclear position ($\hat{\boldsymbol{\mu}}(\mathbf{R}) \approx \hat{\boldsymbol{\mu}}(\mathbf{R}_{eq})$), allowing to remove it from the integral in eq. 2.105

$$C_{\mu\mu}(\boldsymbol{\varepsilon},t) \approx e^{\frac{i}{\hbar}E_0 t} \left| \boldsymbol{\mu}_{0\rightarrow f} \right|^2 \left\langle \psi_0 \middle| e^{-\frac{i}{\hbar}\hat{H}_d t} \middle| \psi_0 \right\rangle . \tag{2.106}$$

Finally, by inserting equation 2.106 in eq. 2.102 it is possible to obtain the final working formula for the absorption cross section

$$\sigma(\boldsymbol{\varepsilon},E) = \frac{E \left| \boldsymbol{\mu}_{0\rightarrow f} \right|^2}{2\hbar^2 c \varepsilon_0} \Re \int_{\mathbb{R}} dt \; e^{\frac{i}{\hbar}(E+E_0)t} \left\langle \psi_0 \middle| e^{-\frac{i}{\hbar}\hat{\mathbf{H}}_d t} \middle| \psi_0 \right\rangle , \tag{2.107}$$

which is composed by a lineshape factor

$$\alpha(\boldsymbol{\varepsilon},E) = \frac{E \left| \boldsymbol{\mu}_{0\rightarrow f} \right|^2}{2\hbar^2 c \varepsilon_0} , \tag{2.108}$$

and a density of states factor which is the real part of the Fourier transform of the survival amplitude between the initial wavepacket and its time evolved on the diabatically coupled excited states

$$I(E) = \Re \left[\int_{\mathbb{R}} dt \; e^{\frac{i}{\hbar}(E+E_0)t} \left\langle \psi_0 \middle| e^{-\frac{i}{\hbar}\hat{\mathbf{H}}_d t} \middle| \psi_0 \right\rangle \right] . \tag{2.109}$$

Chapter 6 will be focused on the computation of the latter quantity.

In an exact framework eq. 2.109 is evaluated by evolving the diabatic reference state $\left| \psi_0 \right\rangle$ under the effect of the true diabatic Hamiltonian, approximated wavefunction based method are able to do so either.[178, 149, 179] On the other hand, in a semiclassical framework a proper definition of the diabatic propagator does not exists. Thus, the next step is to define a semiclassical propagator for the mapping Hamiltonian that will be used to evaluate eq. 2.109

$$\begin{aligned} e^{-\frac{i}{\hbar}\hat{H}t} \approx \iiiint & \frac{d\mathbf{P}(0)d\mathbf{R}(0)d\mathbf{p}(0)d\mathbf{x}(0)}{(2\pi\hbar)^{F+N}} \times \\ & C_t(\mathbf{P}(0),\mathbf{R}(0),\mathbf{p}(0),\mathbf{x}(0)) e^{\frac{i}{\hbar}S_t(\mathbf{P}(0),\mathbf{R}(0),\mathbf{p}(0),\mathbf{x}(0))} \times \\ & \big|\mathbf{P}(t),\mathbf{R}(t)\big\rangle\big\langle\mathbf{P}(0),\mathbf{R}(0)\big| \otimes \big|\mathbf{p}(t),\mathbf{x}(t)\big\rangle\big\langle\mathbf{p}(0),\mathbf{x}(0)\big| \end{aligned} \quad , \tag{2.110}$$

where the coherent states for the nuclear DoFs are defined as in eq. 2.25 and for the electronic ones as

$$\big\langle\mathbf{y}\big|\mathbf{p},\mathbf{x}\big\rangle = \left(\frac{1}{\pi}\right)^{N/4} e^{-\frac{1}{2}(\mathbf{y}-\mathbf{x})^T \mathbb{1}(\mathbf{y}-\mathbf{x}) + \frac{i}{\hbar}\mathbf{p}^T(\mathbf{y}-\mathbf{x})} \ , \tag{2.111}$$

$S_t(\mathbf{P}(0),\mathbf{R}(0),\mathbf{p}(0),\mathbf{x}(0))$ is the classical action

$$S_t(\mathbf{P}(0),\mathbf{R}(0),\mathbf{p}(0),\mathbf{x}(0)) = \int_0^t d\tau \left[\mathbf{P}(\tau)\dot{\mathbf{R}}(\tau) - \mathbf{p}(\tau)\dot{\mathbf{x}}(\tau) - H(\mathbf{P}(\tau),\mathbf{R}(\tau),\mathbf{p}(\tau),\mathbf{x}(\tau))\right] \ . \tag{2.112}$$

The prefactor $C_t(\mathbf{P}(0),\mathbf{R}(0),\mathbf{p}(0),\mathbf{x}(0))$ is rewritten in terms of macroblocks of the monodromy matrix

$$C_t(\mathbf{P}(0),\mathbf{R}(0),\mathbf{p}(0),\mathbf{x}(0)) = \sqrt{\left|\frac{1}{2}\left(\mathbb{M}_{\xi\xi}(t) + \Gamma_{N-el}^{-1}\mathbb{M}_{\pi\pi}(t)\Gamma_{N-el} - i\hbar\mathbb{M}_{\xi\pi}(t)\Gamma_{N-el} + \frac{i}{\hbar}\Gamma_{N-el}\mathbb{M}_{\pi\xi}(t)\right)\right|} \ , \tag{2.113}$$

where the macro-blocks of the monodromy matrix are defined in eq. 2.93 and Γ_{N-el} is the "width" factor for both nuclear (first $F \times F$ block) and electronic (second $N \times N$ block) DoFs, where the latter is always set equal to the unity matrix. Equation 2.110, was already employed to compute correlation functions, [180] within the Forward-Backward (FB) IVR methodology. To the current knowledge of the author, this is the first time that the HHKK propagator is used within the TA SCIVR approximation for the calculation of NA vibronic spectra

$$
\begin{aligned}
I(E) \approx \iiiint & \frac{d\mathbf{P}(0) d\mathbf{R}(0) d\mathbf{p}(0) d\mathbf{x}(0))}{(2\pi\hbar)^{N+F}} \times \\
& \frac{1}{2\mathrm{T}} \left| \int_0^{\mathrm{T}} dt\ e^{\frac{i}{\hbar}[(E+E_0)t + S_t(\mathbf{z}_0) + \phi_t(\mathbf{z}_0)]} \langle \psi_0 | \mathbf{P}(t), \mathbf{R}(t), \mathbf{p}(t), \mathbf{x}(t) \rangle \right|^2 .
\end{aligned}
\tag{2.114}
$$

Where $\mathbf{z}_0 = (\mathbf{P}(0), \mathbf{R}(0), \mathbf{p}(0), \mathbf{x}(0))$ is the phase space vector and $|\psi_0\rangle$ is the reference state, which is chosen in multiple-coherent way

$$
|\psi_0\rangle = \sum_{j=1}^{N} \sqrt{\rho_{jj}(p_{0,j}, x_{0,j})} |1_j, \mathbf{0}\rangle \otimes |\mathbf{P}_{eq}^{(0)}, \mathbf{R}_{eq}^{(0)}\rangle . \tag{2.115}
$$

Where $(\mathbf{P}_{eq}^{(0)}, \mathbf{R}_{eq}^{(0)})$ is the Frank-Condon (FC) point which usually corresponds to $\mathbf{P}_{eq}^{(0)} = 0$ and $\mathbf{R}_{eq}^{(0)}$ is the equilibrium geometry on the ground state from which takes place the vertical excitation to the possible bright states. The prefactor $\sqrt{\rho_{jj}(p_{0,j}, x_{0,j})}$ in eq. 2.115 is the square-root of the classical-mapped population at $t = 0$ as defined in eq. 2.70. Such term is used as an amplitude factor for when more then one bright states are considered.

CHAPTER 3

FROM ANHARMONICITY TO NUCLEAR QUANTUM EFFECTS

3.1 Introduction

As already stated in the first chapter and more in depth treated in the second, the vibrational motion of molecules can be treated in a classical way or in a quantum mechanical one. The easiest way to provide an assessment of the vibrational behavior of a molecule is by means of the harmonic approximation, where the optimization of the molecular geometry is followed by the calculation of the mass-scaled Hessian matrix, finally the diagonalization of the same will return the $3F-6$ vibrational eigenvalues. The corresponding eigenvectors define what are known as the normal modes of vibration.

This procedure takes in consideration only a single molecular geometry and therefore it is based on a very local investigation of the potential energy surface (PES). Actually, molecular PESs can be very complicated and they clearly deviate from the parabolic (harmonic) approximation as soon as the molecule moves away from the equilibrium geometry. In other words, PESs are anharmonic and this feature is reflected by the vibrational spectrum of the molecular system under investigation.

The immediate consequence is that harmonic estimates are often off the mark and more refined methods are needed to take anharmonicity into account.

More elaborated and refined theories are able to account for anharmonic effects. For instance, classical molecular dynamics (MD) simulations have been often adopted to determine the molecular frequencies of vibration. In this kind of approach the simulated trajectories are employed to compute the Fourier transformation of the velocity (momentum) autocorrelation function (2.56). The issue which emerges when choosing the arbitrary probability distribution ($\rho(\mathbf{p}(0), \mathbf{q}(0))$) as a classical Maxwell-Boltzmann distribution, is that the frequency estimates are temperature dependent, and not always carrying out the simulation at the temperature of the reference experiment provides an accurate result. This is particularly true when the experiment is performed at very low temperature as we demonstrate in this work.

Another approach able to include anharmonic effects is represented by QCT molecular dynamics. In this case the working formula is the same as before (eq. 2.56), the difference stands in how each trajectory is initiated. Within this approach, each degree of freedom is initially harmonically quantized (eq. 2.44), after the initial quantization the trajectory is evolved in a completely classical. The approach is more suitable than classical MD when the experiment is undertaken at very low temperature (a few K), but still there is a dependence of the results on the trajectory energy.

Another layer of complexity is added when quantum effects are added while considering the nuclear motion. A large number of methods have been developed within either a time-dependent or time-independent framework. [181–185, 62, 186, 187, 56, 86, 188, 53, 34, 102] Similarly to classical methods, all these quantum approaches can detect the anharmonicity effects related to the potential energy surface, but differently from their classical counterparts they are able to describe also quantum effects.

Quantum effects play a fundamental role in molecular vibrational spectroscopy. One of them is the zero-point energy. This is a purely quantum mechanical quantity which can be estimated by neither experiments nor classical theoretical approaches. The presence of the zero-point energy poses also a challenge to quantum dynamical methods (i.e. those developed in a time-dependent framework). In fact these methods may suffer from zero-point energy leakage,[189–191, 137] while time-independent approaches do not have this issue. However, time-independent methods experience exponential scaling of computational memory with the number of degrees of freedom, an issue not affecting the trajectory-based time-dependent approaches.

As anticipated, experiments cannot provide an estimate of the zero-point energy, but there are other quantum effects clearly present in experimental spectra. Among them, combination bands provide a quantum fingerprint of even complex molecular systems and a representative example is given, for instance, by water clusters[42, 75] or adsorbed molecules on titania.[130, 192, 141] Combination bands are due to transitions associated to the simultaneous excitation of two or more modes. Another difference between a classical and a quantum spectroscopy simulation is that in a classical simulation spectroscopic features are found at integer multiples of the frequencies of vibration (these frequencies are known as higher harmonics and sometimes improperly called classical overtones), while in the quantum world anharmonic overtones, which reflect the changing spacing between energy levels due to the anharmonicity of the potential, are present. Tunneling is another quantum effect which influences spectroscopy.[193, 71, 194, 80, 195] For systems presenting a double well the tunnel effect splits the energy levels and the effect on the vibrational spectrum is that a doublet is present instead of a single peak. This feature is obviously present in experiments but cannot be reproduced with a classical simulation. Finally, quantum mechanics anticipates the possibility of quantum interference, a purely quantum effect which may affect the quantum frequencies of vibration.

Another difference between the classical and quantum description of spectroscopy lies in the dependence of the vibrational frequencies on the temperature. In the classical world, the frequencies of vibration are in general a continous function of the energy of the system, i.e. $\omega = \omega(E)$, and so they are a function of temperature. The quantum picture is described instead by the Schroedinger equation, and in the Schroedinger equation there is no temperature. In few words, the discrete Hamiltonian eigenvalues do not depend on temperature, and so the transition energy gaps between them. This means that quantum mechanically vibrational frequencies are temperature independent. Consequently, a quantum approach should be able to describe quantum effects and also achieve some sort of convergence in the calculation of vibrational frequencies, which makes the method energy or temperature independent. This may look counterintuitive because experience shows that experimental spectra are temperature dependent. However, the reason is that it is the intensity of absorption which varies with temperature, not the frequency which is related to the energy gap between two states. This is because the temperature influences the population of the quantum energy levels and therefore affects the intensity of the quantum transitions (the theoretical counterpart of experimental spectroscopic signals).

During the following chapter will be remarked the limitations of the classical and QCT method, and then compared with the semiclassical approach to vibrational spectroscopy through a simple example. The final objective will be to inquire about the tedious argument risen from the transparent peer-review process of ref. 87, in which the Author and one of the reviewer argued about the difference between what is classifiable as NQEs and what as simple classical anharmonicity.

3.2 Theoretical methods

Classical MD and QCT runs differ in the way the dynamics is performed but they both rely on the mathematical formalism of equation 2.56. [132, 68, 69] The initial distributions of velocities for the MD simulations are obtained from the Maxwell-Boltzmann distribution. Then, a thermalization run at the desired temperature is performed by means of a stochastic velocity rescaling algorithm applied to an evolution of 200000 a.u.[196] followed by a production run 30000 a.u. long in an NVE ensemble. The production dynamics is used to collect the data necessary for calculating the vibrational frequencies.[197] QCT simulations start the trajectories at a target and harmonically quantized energy.[198] The starting configuration of all trajectories is chosen to be the equilibrium geometry, while initial atomic linear momenta are extracted from a Husimi distribution and then rescaled in a way that the total energy matches the target one, i.e. the harmonic zero point energy or a multiple of it. QCT trajectories are evolved in an NVE ensemble for a total time of 25000 a.u. For both MD and QCT a 4th order symplectic algorithm is adopted for evolving the trajectories.[199]

The phase space integration in eq. 2.56 is evaluated in a Monte Carlo way: For all temperatures and energies investigated 6000 trajectories are generated starting from a distribution of initial conditions and average the time-dependent integrand over the trajectories.

Another technique employed in this chapter is known as adiabatic switching (AS).[200–206] The starting point of adiabatic switching is the classical Hamiltonian of a set of F uncoupled harmonic oscillators (H_0) to obtain a harmonic quantization of the initial energy. In this aspect AS resembles QCT but, differently from the QCT runs, in which trajectories are evolved in the NVE ensemble according to the classical molecular Hamiltonian, in AS the actual classical molecular Hamiltonian (H) is very slowly switched on. In formulae

$$H^{AS}(t) = H_0 + f_S(t)(H - H_0) \qquad H_0 = \sum_{i=1}^{F} \left(\frac{p_i^2}{2} + \frac{\omega_i^2 q_i^2}{2} \right) , \tag{3.1}$$

where $H^{AS}(t)$ is the AS Hamiltonian and f_S is a switching function, for which several expressions have been proposed and adopted in the literature. Here, the latter is defined as it was done in some previous works about the adiabatic switching[207–209]

$$f_S(t) = \frac{t}{T_{AS}} - \frac{1}{2\pi} \sin\left(\frac{2\pi t}{\mathrm{T}_{AS}}\right). \tag{3.2}$$

Where T_{AS} is the total time of the adiabatic switching evolution, which was chosen as $\mathrm{T}_{AS} = 200000$ a.u. AS is based on the adiabatic theorem which states that if one starts with a quantized model system (a set of harmonic oscillators) and switches on very slowly the molecular Hamiltonian (ideally taking an infinite amount of time), then the initial quantization is preserved also for the molecular system.[210] The theorem is valid when the density of states is low, i.e. for the ground state (zero-point energy) and the first excited states, i.e. for determining the fundamental frequencies of vibration. Therefore, by means of adiabatic switching one can employ a classical dynamics to get a limited amount of approximate quantum information. For this reason AS is sometimes labeled as a semiclassical approach. However, it necessary point out that AS is not derived from the Schroedinger equation and it is based on Newton's laws of motion.

In this chapter, it is employed a particular version of TA SCIVR (eq. 3.3) known as the adiabatically switched semiclassical initial value representation (AS SCIVR).[207–209] It is made of a preliminary part in which an adiabatic switch run is performed followed by a TA-SCIVR simulation. In this kind of approach the starting conditions of the TA-SCIVR simulation correspond to the exit conditions of the AS procedure. This is more accurate than using a Husimi distribution. Indeed, AS SCIVR provides better resolved spectroscopic signals, it is characterized by a much lower trajectory rejection rate, and it allows one to perform full dimensional simulations of larger systems.

The H_2CO molecule was chosen as an example of a system where anharmonicity is present. To show this it is reported in Table 3.1 a comparison between the quantum mechanical and harmonic fundamental frequencies of vibration of this molecule. An analytical PES for H_2CO constructed by Martin et al. at CCSD(T) level of theory[211] was employed. On this PES time-independent, full-dimensional quantum mechanical calculations were performed by Carter et al.[212] From the data reported, it is clear that the quantum frequencies of vibration are substantially shifted with respect to harmonic estimates, and, as anticipated, being the results at the quantum mechanical level, there is no need to specify what temperature these data are referred to.

Table 3.1 Quantum mechanical (QM) and harmonic (HARM) estimates of the fundamental frequencies of vibration of H_2CO. Δ is the anharmonic correction, i.e. the difference between the exact and the harmonic value. Values are in cm^{-1}.

Frequency	QM	HARM	Δ
ν_1	1171	1192	-21
ν_2	1253	1275	-22
ν_3	1509	1543	-34
ν_4	1750	1781	-31
ν_5	2783	2929	-146
ν_6	2842	2996	-154

3.3 Results and Discussion

The results of the classical simulations are presented. The MD simulations, carried out in the NVT ensemble (i.e. in a canonical ensemble where the number of particles, volume and temperature are held fixed), are performed at different temperatures, while the QCT ones, carried out in the NVE ensemble , are undertaken at different values of the total energy.

To start off the focus is set on the highest fundamental frequency, labeled ν_6, because it is the frequency presenting the largest shift ($-154\,\mathrm{cm}^{-1}$). The normal mode associated to it, mode 6, is related to the CH_2 asymmetric stretch. From Figure 3.1 it is evident that the estimated frequency is changing with the temperature or energy employed. More precisely, when MD is performed at very low temperature (10K) or QCT is undertaken at an energy which is just 5% of the harmonic zero-point energy, the simulations return a frequency value which is basically the harmonic one. The reason for this is that at such low temperature or energy the classical trajectory can sample only a region of the PES close to the equilibrium position. In this region the parabolic (harmonic) approximation to the PES is valid and a frequency value close to the harmonic one is obtained. Remarkably, for the same reason, the MD simulation at room temperature (300K) fails badly in estimating the frequency of vibration.

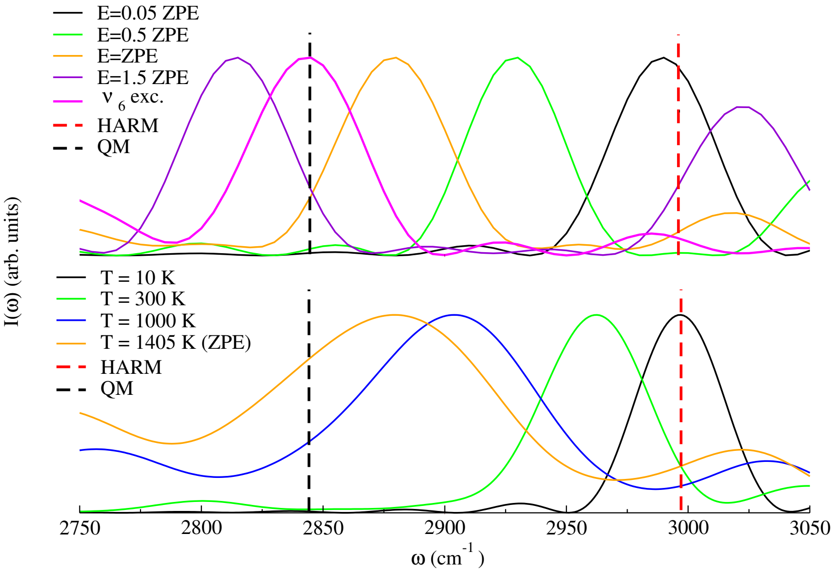

Fig. 3.1 QCT (upper panel) and MD (lower panel) simulations of ν_6 in H_2CO. The maximum of intensity has been set equal to 1 for all simulations.

Moving to higher energies (or temperature) when the energy equals the harmonic ZPE, then the frequency estimate gets closer to the quantum mechanical benchmark (it is about 30 cm^{-1} away). Secondly and remarkably, the ν_6 exc. and 1.5 ZPE simulations are characterized by about the same energy (just a few wavenumbers difference) but while the ν_6 exc. trajectory is on the mark, the 1.5 ZPE trajectory is clearly underestimating the QM frequency. This is a demonstration that not only the total energy (temperature) of the trajectory but also the way it is distributed in the molecule may affect the outcome of a classical simulation. The fact that with the ν_6 exc. trajectory a classical method like QCT is able to reproduce the quantum frequency demonstrates that there are no sizeable quantum effects in play and anharmonicity can be detected by means of classical approaches. Finally, it is also possible to notice that for the trajectories run at high energy or temperature some spectroscopic features appear above 3000 cm^{-1}. Those are the higher harmonics associated to lower-frequency modes, in particular mode 3 and mode 4. It is not surprising that their intensity is quite high because as stated in section 2, the simulated spectra are not dipole (IR) spectra, so intensities in Figure 3.1 are not related to the actual absorption intensities but to the recurrence of trajectories in the phase space.

It is clear that both methods are able to account for the anharmonicity of the formaldehyde PES. QCT by means of a tailored single-trajectory is giving the best estimates. Also, classical spectra, as expected, present only the spectroscopic features related to the fundamental frequencies of vibration and some higher harmonic overtones. In Table 3.2 are reported values obtained with the classical simulations and compared with the harmonic and quantum mechanical results. For QCT are reported results obtained by running the trajectories at E=ZPE, while for MD are provided results for the trajectories thermalized at T=1405 K. This temperature is the thermal equivalent of the zero-point energy according to the equipartition theorem is valid.

Table 3.2 Harmonic, quantum, and classical frequencies of vibration of formaldehyde. For QCT the results are reported for E=ZPE, while MD results come from the simulation at T=1405K. The Mean Absolute Error (MAE) is referred to the QM results. Values are in cm^{-1}.

Frequency	HARM	QM	QCT(NVE, E=ZPE)	MD(NVT, T=1405 K)
ν_1	1192	1171	1165	1162
ν_2	1275	1253	1255	1253
ν_3	1543	1509	1506	1515
ν_4	1781	1750	1755	1753
ν_5	2929	2783	2835	2839
ν_6	2996	2842	2880	2881
MAE	51	-	18	19

From Table 3.2 it is possible to notice that QCT and MD values for simulations run at similar energies are very close to each other, another clue at the dependence of classical results on the involved energy. Furthermore, they provide good estimates of the frequency of vibration when anharmonicity is low, while they are off the mark for the higher frequency modes where anharmonicity is more evident. It was anticipated that, for instance, a tailored single-trajectory QCT simulation is needed to get the correct ν_6 frequency.

It is now possible to move to the quantum results obtained in semiclassical approximation by means of AS SCIVR. There are two ways, which are relevant for the present work, in which quantum spectroscopical effects can show up: One is by means of a peculiar quantum shift from harmonic estimates not reproducible by classical simulations; the other one is the presence in the quantum spectrum of additional features with respect to the classical counterpart. The former is not the case of H_2CO since appropriate classical simulations provide estimates which are very close to the quantum mechanical benchmark. As for the latter aspect is reported in Figure 3.2 the outcome of our AS-SCIVR simulation for H_2CO. To perform the AS-SCIVR calculation 50000 a.u. long trajectories are employed, characterized by initial harmonic ZPE quantization, for the preliminary adiabatic switching part, followed by 50000 a.u. long trajectories for the semiclassical part. We set the threshold for trajectory rejection at the very strict value of 10^{-6} with the result that about 500 trajectories are retained for the simulation. This number of trajectories is sufficient for AS SCIVR to simulate a very detailed spectrum.

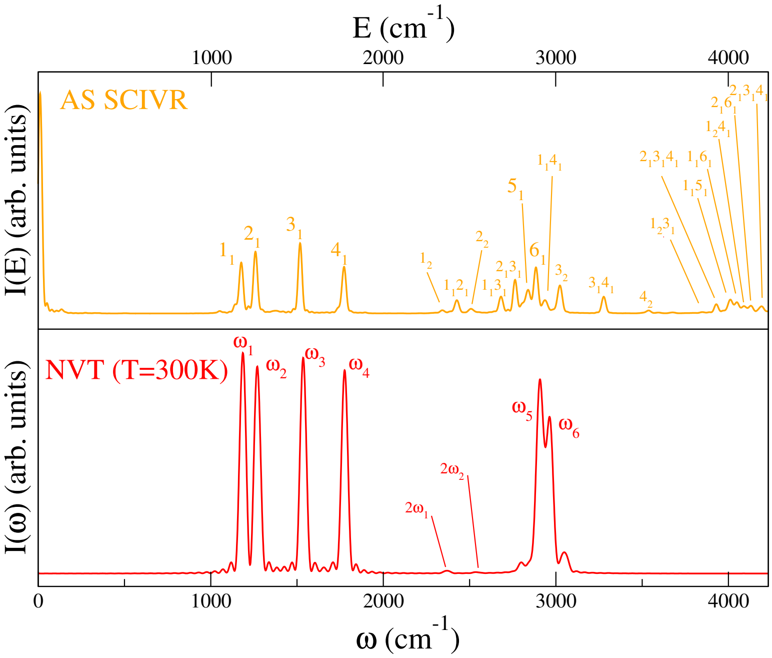

Fig. 3.2 Comparison between AS-SCIVR and MD simulations of the H_2CO spectrum. In the AS-SCIVR panel the ZPE has been shifted to 0 and subscripts indicate the quanta of excitation in the corresponding mode.

Table 3.3 AS-SCIVR results for all fundamental frequencies and 4 pure overtones of H_2CO. Superscripts indicate the overtones. MAE is referred to the QM results. Values are in cm^{-1}.

Frequency	HARM	QM	AS SCIVR
ν_1	1192	1171	1158
ν_2	1275	1253	1245
ν_3	1543	1509	1507
ν_4	1781	1750	1748
ν_5	2929	2783	2784
ν_6	2996	2842	2844
ν_1^2	2392	2333	2315
ν_2^2	2550	2502	2490
ν_3^2	3086	3016	3016
ν_4^2	3562	3480	3488
MAE	67	-	7

It is immediate to notice that the AS-SCIVR spectrum presents many more features than the classical one. The reason is that AS SCIVR is able to point out quantum features. One example is given by the combination bands, which are mixed excitations of several modes (see for instance the energy levels associated to $1_1 2_1$ and $1_1 3_1$ and many others).

As anticipated, the simulation has been performed starting from harmonic ZPE energy quantization. This is the best condition to evaluate the ZPE (5768 cm^{-1}), but a more accurate estimate of frequencies is obtained by employing different AS-SCIVR runs for the several energy levels starting each simulation from the appropriate harmonic energy quantization. Results are reported in Table 3.3, from which another quantum spectroscopic feature can be appreciated: AS-SCIVR overtones are anharmonic if compared to twice the corresponding fundamental frequency (this is evident for ν_4^2 compared to ν_4), whereas in classical simulations one finds higher harmonics at integer multiples of the frequencies of vibration. Finally, we notice that AS SCIVR returns a very low MAE even when overtones are taken into consideration.

With these results it is possible to demonstrate that some spectroscopic features can be detected only when a quantum approach, even in an approximate way, is undertaken. However, so far the demonstration has not involved the fundamental frequencies of vibration, which are the most relevant ones in an experimental spectrum. In fact it was shown indeed that a tailored QCT simulation is able to accurately identify even the most anharmonic (ν_6) of the six vibrational frequencies of formaldehyde. However, as anticipated, such behaviour is not observed in the case of formaldehyde. Though, a previous work by Gabas et. al., [43] clearly demonstrate that the SC IVR is able to capture this experimentally observed phenomenon for the H_2-tagged protonated glycine.

3.4 Conclusions

An interesting question in theoretical vibrational spectroscopy concerns the possibility to identify anharmonicity and quantum effects and distinguish between them in a spectrum. In this chapter three different types of theoretical approaches to the vibrational spectroscopy of the isolated formaldehyde molecule were presented. The interest was set on studying the frequencies of vibration because both anharmonicity and quantum effects imply a shift in the spectrum from the harmonic value. Though, it was observed that while all the frequency shifts were reproducible by the QCT and MD approaches, the quantum effects manifested as additional features in the spectrum, such as anharmonic overtones and combinations bands.

Based on this evidence the conclusions are twofold. First of all, appropriate simulations provide one with a way to distinguish between anharmonicity and quantum effects. Secondly, recalling the title of the chapter, things are not always as they seem. Not necessarily a shift with respect to the harmonic estimates is related to a quantum effect. For this reason to confirm the effectiveness of a new method in theoretical vibrational spectroscopy one should test it against systems known to present quantum effects like a double well potential, which is characterized by a tunneling splitting, or the H_2-tagged protonated glycine.

CHAPTER 4

VIBRATIONAL SPECTROSCOPY SIMULATION OF SOLVATION EFFECTS ON A G-QUADRUPLEX

4.1 Introduction

The nowadays well known double helix structure of DNA is widely regarded as one of the most important discoveries of the last century. This kind of structure is characterized by a well defined pattern of interactions between pairs of nucleobases and it is able to preserve the entire genetic information of living creatures. It is also now known that some nucleobases are able to interact with each other in a different way than the one described by Watson and Crick (WC).[213] To emphasize this concept, some computational studies demonstrated that guanine seems particularly prone to interact with other guanine molecules.[214–216] In many living organisms we are indeed able to observe this behavior, for instance in the guanine rich sequences found in the telomeric and promoter regions of DNA.[217] It is likely that these sequences fold into a non canonical double-helix

WC structure, where four guanines interacting through Hoogsteen-type bonding are arranged in a square planar geometry. This type of geometries that are formed by one, two or four DNA strands, are also known as G-quadruplexes. Recently a lot of attention has been payed by the scientific community to these kinds of systems due to their potential functional role in gene regulation and DNA repairing mechanisms from lesions.[218, 219]

The interest in G-quadruplexes comes mainly from their potential applicability as targets of cancer therapeutics,[220–224] but also for their possible role in virus replication activity for viruses like HIV and SARS-CoV-2.[225–228] This is due to the fact that G-quadruplexes serve as kind of "knot" in the DNA replication process signaling the stop of transcription. This means that the development of ligands stabilizing the quadruplexes could be used to induce the apoptosis of target cells.[229] Many efforts have been put also in the *in vitro* detection of specific G-quadruplexes by means of UV spectroscopy and Circular Dichroism (CD).[230, 231] Other techniques used for the analysis of the quadruplexes in water solutions, which are also good candidates for the *in vivo* detection, are Raman spectroscopy (RS) methods such as surface enhanced Raman spectroscopy (SERS), polarized Raman scattering, and UV resonant Raman (UVRR).[232–234] While all of these approaches focus mainly on the effects of topology change, change of the templating cation and signal identification, none of them seem to point towards solvent effects, which are fundamental to be taken into consideration before moving to the in vivo analysis.

In this chapter the main goal is to understand the effects of solvation on the vibrational features of the G-quadruplex. In particular, the focus is on the differences that occur between gas phase spectroscopic simulations and simulations carried out in a box of solvent. The latter should also allow to demonstrate that use of an appropriate explicit solvent is fundamental to catch the correct shifts caused by system-solvent interactions. As starting benchmark a simple system like the 2'-deoxyguanosine is considered, which is studied both in gas and solvated phase. The information gained from this first set of simulations is used to show how solvation acts differently when the same molecule is found in a quadruplex arrangement, and compare our results with experimental data. [232]

4.2 Computational details

The reported simulations are characterized by more than 20000 degrees of freedom. Therefore, the only viable way to describe the PES of the system is the adoption of classical force fields. (FF) In a previous work presented by Gabas et. al.,[131] several FF were benchmarked against ab initio data, and the polarizable FF AMOEBABIO18 included in the Tinker 8.6.1 software suite emerged as the most effective one.[235, 236] An important point to make while using FF applied to spectroscopic simulations is that as the quality of the PES description is limited, so it is expected to be the accuracy with respect to experimental data. However, a qualitative and insightful description of the spectroscopic features is still achievable.

For every studied system, a preliminary geometry optimization is carried out in gas-phase conditions, with a quasi-Newton algorithm. Then, the system is inserted in a solvent box with periodic boundary conditions (PBC), and particle mesh Ewald (PME) scheme for the long range interactions is adopted. Choice of the dimension and shape of the box is specific for the system and will be specified later in this section. Once the molecule is inserted in the PBC box, a second optimization with the steepest descent method is carried out. The MD simulations are propagated for 3000 steps with a time step of 0.2 fs by using the Beeman integrator.[237] To initiate the dynamics, initial conditions equal to the ones of equation 2.44 are employed by setting $\theta = \frac{\pi}{2}$ for single trajectories. With these initial conditions it is possible to run trajectories at an energy close to the harmonic ZPE. By adding a quantum of excitation on a given mode, the energy of the trajectory will be closer to the energy of the quantum state corresponding to the excitation in that mode.

Most of the spectroscopic simulations presented in the chapter are made at the QCT level. The used approach with this method is to run a single trajectory with a quantum of excitation in the mode of interest. Usually a trajectory per mode of interest is sufficient to obtain a clean and accurate enough spectrum, but as it will be shown in the results section, for some modes a wider area of the phase space needs to be sampled to achieve a better qualitative description of the spectroscopic feature. In the latter instance, we sample initial conditions randomly from eq. 2.44.

In the case of Semiclassical calculations, the Divide and Conquer Multiple-Coherent Semiclassical Initial Value Representation is employed to compute the quantum mechanical spectra of both gas phase and solvated systems. To evaluate the sub blocks of the monodromy matrix which appear in ϕ_t the gradient method [130, 192] explained in section 2.3.1 is employed. In this way, we are able to focus only on the normal modes centered on the molecule and eliminate from the spectrum those coming from the solvent molecules. For SC calculations, a single trajectory has been used upon setting to zero the initial momentum of all the normal modes with harmonic frequencies lower than 300 cm^{-1}, and providing all other normal modes with the basic zero-point energy contribution (i.e. n=0).

As anticipated in the introduction, the focus is set on the study of the 2'-deoxyguanosine, and a tetrad of 2'-deoxyguanosine which from now on will be simply referred to as the “quadruplex”. Guess geometries for both systems are extrapolated by removing the necessary residues from a DFT optimized structure published in a paper by Sponer et. al.[215] Then, minimization is performed for a single deoxyguanosine inserted in a 30 Å-side cubic box filled with water (2702 atoms), and the quadruplex inserted in a rectangular box with a 50×50 Å^2 base, and 30 Å height. (7517 atoms) For both systems long range interactions are considered using PME.[238, 239] As a comparison with experimental data, we considered the Raman spectrum in water of the thrombin binding aptamer (TBA) by ref. 232 In this case it was made the assumption that the quadruplex considered in our simulations can be thought of as a minimal sub-unit of the full TBA. Other experiments with other types of G-quadruplexes exist as well, but since the TBA is one of the smallest systems that can be found in literature it could better resemble the behavior of the minimal unit that is being considering. At the moment is not possible to fully asses how much the presence of a rigid backbone like the one present in the TBA can influence our discussion, but this factor will be taken into consideration in the result discussion part.

The vibrational normal modes considered in this work, for both studied systems are the asymmetric and symmetric stretches of the C2'H_2 group of the sugar moiety, the C6=O stretch, and the 2'-deoxyguanosine (dG) ring deformation mode.

4.3 Results

4.3.1 2'-Deoxyguanosine

In the first set of QCT simulations performed on the 2'-deoxyguanosine molecule, it was observed that solvation acts differently on different normal modes. Specifically, it is possible to observe that for the C=O stretch, (figure 4.2, panel a) multiple vibrational features are present in both solvated and gas phase systems. In order

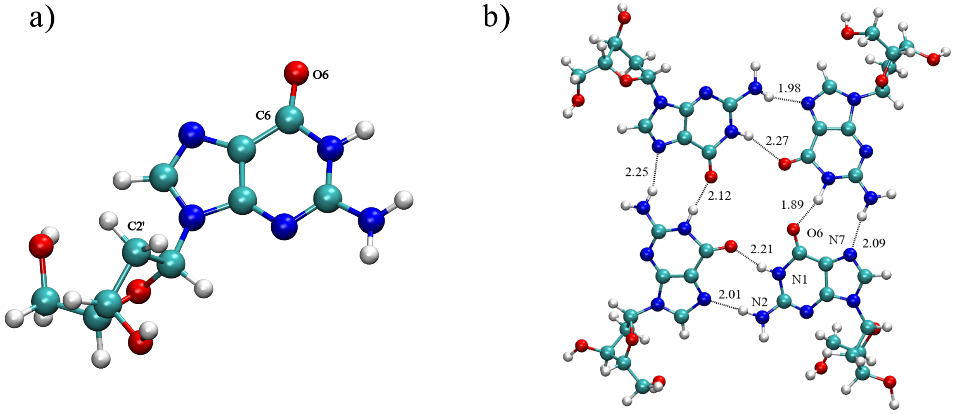

Fig. 4.1 a) 2'-deoxyguanosine minimum geometry in the water box; b) quadruplex minimum in the water box.

to assign the C=O stretch to the correct peak, a more detailed analysis has been conducted. For both systems two additional trajectories are run. In one all the initial momenta are set to the harmonic ZPE (ZPE trajectory). In the other one the initial momentum of the C=O stretching mode is set to zero, while all the other modes have the same initial momenta as in the ZPE trajectory (Deactivated trajectory). By doing so, in the gas phase spectrum (figure 4.3 panel a) it was observed for the deactivated trajectory a single peak much more intense than the one observed in the original trajectory, which was characterized by a harmonic quantum of excitation in the stretch and the corresponding harmonic zero-point energy contribution in all other modes. The position of this peak is ≈ 30 cm^{-1} red-shifted with respect to the most intense peak in Figure 4.2 a. In the ZPE trajectory the same feature of the spectrum in Figure 4.2 a is observed, even if it is slightly blue-shifted and with a change in the intensity ratio between the most intense peak and the secondary one. In particular it seems that the secondary one gains in intensity with these set of initial conditions, while the main one loses intensity. Based on these observations it is possible to conclude that the most intense peak can be assigned to the C=O stretch because in the deactivated trajectory it provides an almost harmonic signal. Moving on to the analysis of the solvated system, (figure 4.3 panel b) it was observed that both the deactivated and ZPE spectra are much less intense than the one in Figure 4.2 a. In the spectrum generated by the deactivated trajectory, a single peak is again observed. It is positioned almost at the same frequency of the secondary peak on the right of the main one. A similar situation is observed with the ZPE trajectory, with the main difference that the observed feature is enlarged with a shoulder near the position of the most intense peak of the original spectrum. (figure

4.2 a) Again, these two observations led to the conclusion that the C=O stretch is the one positioned at 1553 cm^{-1}, which corresponds to the most intense one. With this results in mind one can conclude that a red shift is observed when solvent molecules are added, on the contrary of the harmonic estimates.

By a simple visual analysis of the MD simulation whereby the spectrum has been calculated, it is possible to observe that this part of the molecule is strongly interacting with the surrounding water molecules. Therefore, it is possible to think that this interaction with water is what causes the observed red shift of the QCT signal with respect to the gas phase case. Another peculiarity that can be observed from the spectrum in figure 4.2, is that while the QCT signal is reported to be strongly harmonic in gas phase, in the water box simulation the harmonic estimate is 115 cm^{-1} far from the QCT signal. Probably this anharmonicity derives from the fact that in the equilibrium conformation, from which the harmonic estimate is made, the C=O group sense some of the interactions with the solvent as repulsive. This could explain also why the harmonic estimates of the CO stretch in the water box system are blue shifted with respect to the harmonic estimate made in vacuo. This result demonstrates the importance of anharmonicity and dynamical effects when simulating biomolecules in solution. The opposite effect was observed for the ring deformation mode (dG RDM). In this case solvation seems to blue shift both the QCT and harmonic estimates with respect to the signal observed in gas phase. (fig. 4.2 panel b)

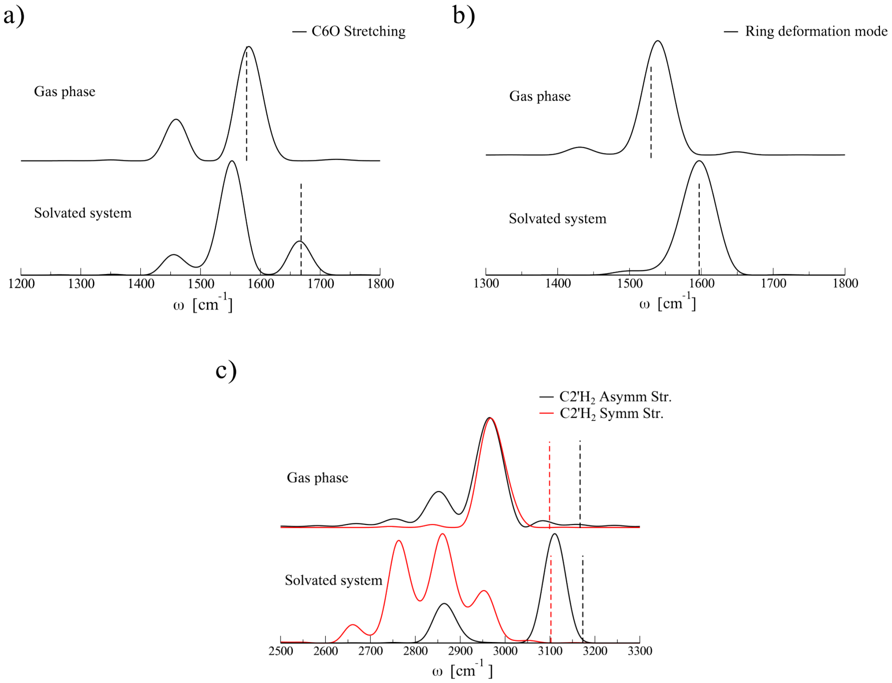

Fig. 4.2 QCT spectra with a single trajectory per normal mode. Panel a) C=O stretch, b) ring deformation and c) asymmetric and symmetric stretches of C2'H_2. Vertical dashed lines indicates the harmonic estimates.

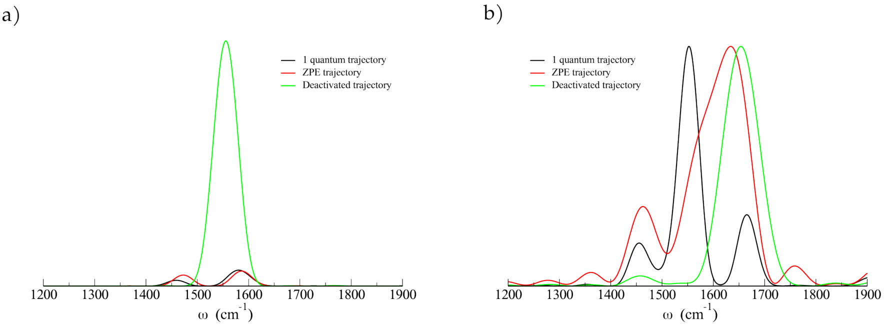

Fig. 4.3 QCT spectrum for the C=O stretch compared with the two spectra calculated with the other additional trajectories a) gas phase b) water box (normalized)

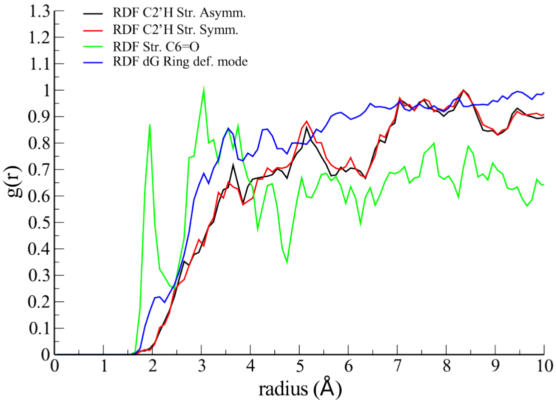

Fig. 4.4 Radial distribution function (RDF) for the trajectory associated to the analyzed normal modes calculated between the group of atoms of interest and water.

DG RDM is a vibrational normal mode delocalized on all atoms of the guanine. For this reason a simple visual analysis of the MD simulation may be not sufficient to understand why the spectrum in figure 4.2 (panel b) features blue shifted QCT and harmonic frequencies with respect to the corresponding ones in the gas phase simulation. By calculating an average [240] of the radial pair distribution function (RDF) between all the atoms of the guanine ring and all that ones of the water molecules (blue solid line in figure 4.4), it is possible to observe that water tends to occupy outer solvation shells, except for a little peak near 2 Å, which can be interpreted as the presence of labile short range interactions. This probably means that the interactions between water and the whole guanine ring tend to be unfavorable. By observing the RDF for C6=O (green solid line in figure 4.4) atoms, it can also be found the proof that during the MD simulation this part of the molecule is strongly interacting with water. In particular this can be deduced by the fact that a high peak is present at distances shorter than the first solvation shell.

The last set of normal modes that was analyzed for the 2'-deoxyguanosine is mostly localized on the C2'H_2 group on the sugar moiety of the molecule.

By observing the spectrum of the C2'H_2 modes, (figure 4.2 panel c) it is expected to be difficult to extract much information. This is due to the fact that in the QCT gas phase spectrum associated to the trajectory of the symmetric stretch there is also a signal related to the asymmetric stretch, while for a water solvated system the signals are split but do not provide a clear fingerprint. For the gas phase system, we relate the presence of several peaks to the fact that a single trajectory for these two modes is not sufficient to sample a wide enough phase-space volume around the minimum geometry.

For this reason a multiple trajectory approach is employed, with initial conditions as stated in equation 2.44. In particular, such method is tested with, 10, 100 and 1000 trajectories for the gas phase system, for all the normal modes to be studied.

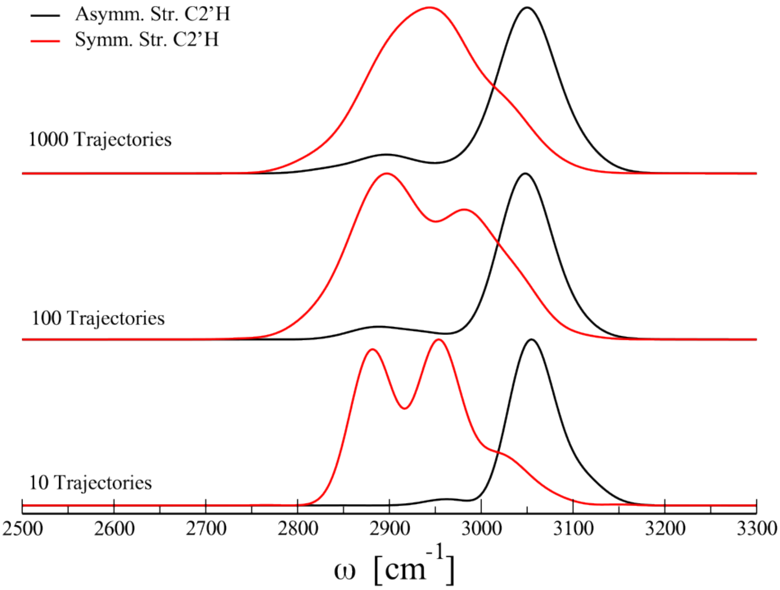

Fig. 4.5 C2'H_2 stretches QCT spectra averaged on multiple trajectories for the gas phase simulations.

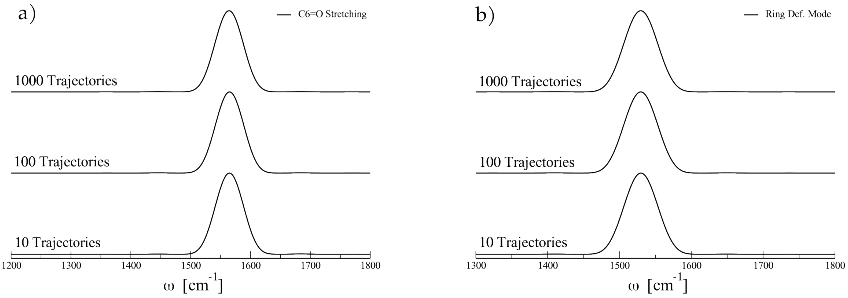

Fig. 4.6 QCT spectra of the a) C=O stretches and b) dGRDM, calculated by means of multiple trajectories

By observing the spectra in figure 4.5, it is possible to see that by increasing the number of trajectories from 10 to 1000 a better resolution of the separation between the QCT asymmetric and symmetric stretches for C2'H is obtained. On the other hand, for the C=O stretch and the ring deformation mode (figure 4.6) a reduced number of trajectories is already sufficient to provide a properly converged signal. This could be due to the fact that normal modes like the C=O stretches and dG RDM are usually rather harmonic, meaning that a more restricted volume of phase space can be sampled to recover the correct spetroscopic feature.

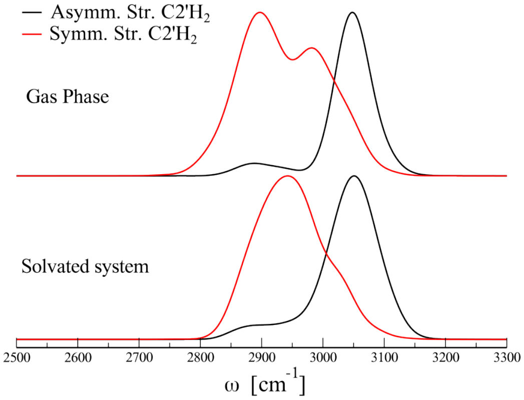

Fig. 4.7 QCT spectra of the C2'H_2 modes averaged on 100 trajectories.

Given these results it is now possible to apply our multi-trajectory approach to water solvated systems. This is done by employing 100 trajectories given the unaffordable overhead of adopting 1000 trajectories for such systems. By comparing gas-phase and "in solution" spectra, we are eventually able to assess the effects of solvation on the C2'H_2 normal modes. In this case, it is found that results are very similar in the two different phases. This lead to the hypothesis that water molecules have no sizable interactions with the C2'H_2 group. This can be verified by looking at the RDF plots for the two trajectories in question (fig. 4.4 black and red lines). In these cases it can be observed that water tends to be organized in solvation shells without any sign of short range interaction.

4.3.2 Quadruplex

In the vibrational analysis of the single 2'-deoxyguanosine molecule it was observed that the effects of solvation are quite complex and not easily detectable by adopting simple rules of thumb. Moving on to a more complex system like the quadruplex will further prove this concept true. In particular, in a system like the quadruplex it is possible to ascertain that a well-defined pattern of interactions between the four 2'-deoxyguanosine residues is present. It will be possible to confirm if the water molecules are able to interact mainly with the external part of the system, while the core of the system is partially hindered to interact with the solvent. More than that, in a structure like the one of the quadruplex, it is expected that the vibrational frequencies of the modes under investigation stick to a symmetry related order. The whole supramolecolar system which composes the quadruplex (figure 4.1) should ideally belong to the D_{4h} symmetry group. Therefore, in an ideal scenario, the normal modes which we are considering should reveal a 4-fold degeneracy. In reality there are small deviations from this symmetric arrangement and so symmetry-related frequencies are expected to be close to each other but not exactly degenerate.

In the experimental spectrum of TBA,[232] the signals of the C2'H_2 stretches are assigned to a broad low intensity feature. The main peak at 2952 cm^{-1} is related to the asymmetric stretch, while the shoulder at 2890 cm^{-1} to the symmetric stretch. The C=O stretches are experimentally assigned to the intense and broad peak centered at 1663 cm^{-1}, while the dG RDM mode is assigned to an intense narrow peak at 1582 cm^{-1}.

We start the vibrational analysis of the quadruplex by looking at the C2'H_2 normal modes. As it was observed on the previous case, a single trajectory per normal mode is not sufficient to extract fully reliable information.

For this reason the spectrum is calculated by running 100 trajectories for both the gas and solvated system. With this approach it is possible to reproduce the experimental feature. On the other hand, these results do not have a strong quantitative agreement with respect to the experimental data, resulting in a Mean Absolute Error (MAE) of 107 cm^{-1}. As anticipated in the Introduction, this is mainly due to the force field we need to employ to describe the PES of the system.

On the basis of the calculated spectra in figure 4.8, it is also easy to see that even in this case the solvation of the system has nearly no effect on the C2'H_2 signal positions. In the case of a single 2'-deoxyguanosine, this part of the molecule seems to have almost no interaction with the water molecules and for the quadruplex, it possible to suppose that this should not change much. In TBA, the tetrad of guanine is surrounded by a rigid backbone and the region near the C2' is excluded from interacting with water as well, and, for this reason, we think that considering a

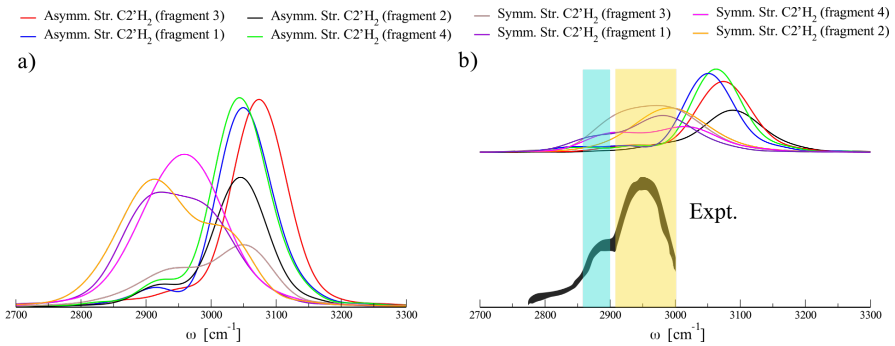

Fig. 4.8 Gas phase a) and solvated system b) C2’H stretches QCT spectra calculated by means of 100 trajectories. The profile of the experimental feature is presented as a broad black line, where the asymmetric streching is highlighted in yellow and the asymmetric one in teal.

model where this part of the molecule is weakly interacting with water should not be a rough approximation.

Moving on to lower frequencies, we analyze the C=O stretches. In the optimized structure of the quadruplex, water molecules are able to interact with the C=O group of the quadruplex only from above or below and this makes this part of the molecule less prone to solvent interaction.

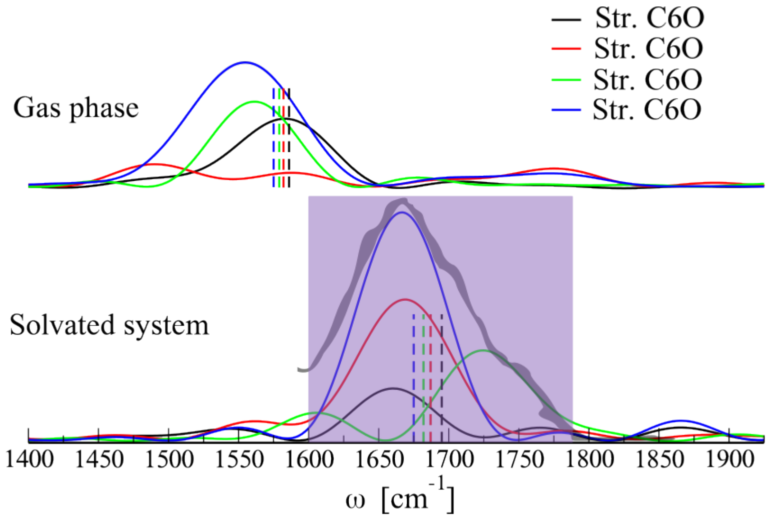

Fig. 4.9 C6O stretches QCT spectrum (solid colored lines) and the relative harmonic estimates (vertical dotted lines) for the gas-phase and solvated quadruplex.

By observing the spectrum in figure 4.9, it is clear that in this case the addition of solvent molecules to the simulation has the effect to blue shift the frequencies with respect to the gas-phase simulation. The opposite effect is observed for the single 2’-deoxyguanosine molecule, which means that solvation has a different effect on the vibrational features of the quadruplex. The RDF is used again as a tool to better understand such results. (figure 4.10) In this case is possible to observe that the shape of the function is much similar to the one of the dG RDM mode reported in figure 4.4 for the single 2’-deoxyguanosine.

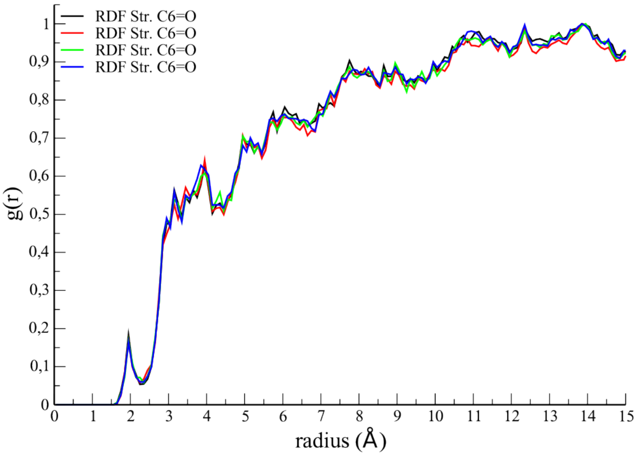

Fig. 4.10 RDF function between the four C6 = O and the water molecules for all the four trajectories

This means that the interaction of the C=O group with water is weak and unfavorable. The agreement with the experiment for the C=O stretches is good, and the QCT signals for these modes computed for the quadruplex are also blue shifted with respect to the one computed for the single 2’-deoxyguanosine. This shift, as reported in the literature,[241] is a distinctive sign of the presence of the 2’-deoxyguanosine in a G-quadruplex arrangement instead of a single/double strand configuration.

Table 4.1 QCT frequencies comparison between gas phase and water box simulation for both the quadruplex and single 2’-deoxyguanosine molecule

	Gas phase		Water box	
	2’-deoxyguanosine	quadruplex	2’-deoxyguanosine	quadruplex
Str. C=O (cm^{-1})	1581	1583 1587 1561 1555	1553	1660 1669 1724 1667

The last set of normal modes that are left to be examined are the dG RDM modes. Most of the observations regarding this set of normal modes are mostly aligned with what was observed with the single 2’-deoxyguanosine, i.e. this set of modes are strongly harmonic, and solvation makes both the QCT and harmonic estimates blue shift. The main difference lies in the reason of the blue shift, since the water molecules are not able to get as close to the guanosine rings as in 2’-deoxyguanosine.

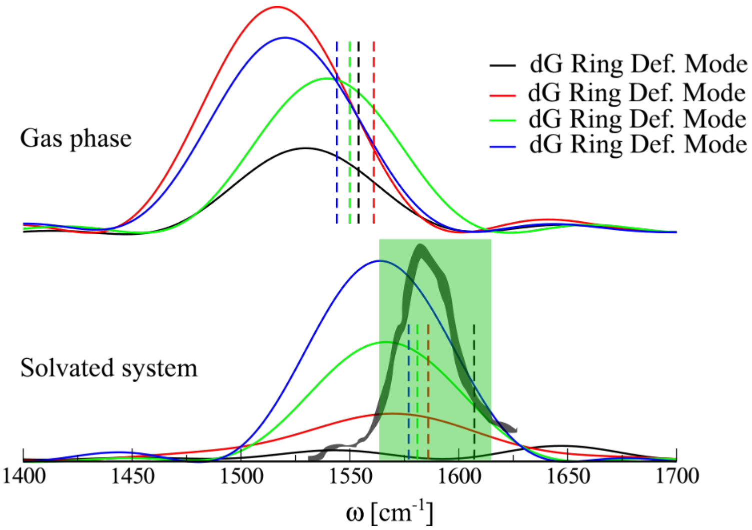

Fig. 4.11 dGRDM QCT spectrum (solid colored lines) and the relative harmonic estimates (vertical dotted lines) for the ring deformation modes. The green band identifies the experiment.

Likewise the case of the C=O stretches of the quadruplex, in the dG RDM spectrum (figure 4.11) it is observed that both the harmonic and QCT signals are in good agreement with experimental data. The main difference between the harmonic estimates and the QCT frequencies is that the latter are nearly degenerate like the experimental ones. As anticipated, the reported simulation concerns only a minimal unit of the full TBA. This means that compensation of errors could be a factor in this last set of results, but it has to be noted that, like in the full structure, also the core part of the quadruplex has low capability of interaction with water molecules. Therefore, it is possible to suggest that the effect of the presence of a rigid backbone is to preserve the core part of the G-quadruplex, which means that a structure without it opens the possibility on longer time scales to see a dissociation of the supramolecular system. Following this argument we think that the role of the water molecules in the quadruplex simulations is to constrain the four fragments of 2'-deoxyguanosine in the quadruplex geometry. The geometry of the system restrained in the quadruplex form can lead to repulsive interactions with the other 2'-deoxyguanosines, so that it should be possible to explain the observation of blue shifts when solvent molecules are added.

Table 4.2 QCT frequencies of the studied modes compared between the single 2'-deoxyguanosine and the quadruplex and to experimental data of TBA from ref. [232]

	Summary table of QCT frequencies (cm^{-1})				
	2-deoxyguanosine		quadruplex		
	gas phase	water box	gas phase	water box	exp. TBA
Asymm. Str. C2'H_2 (100 trajectories)	3048	3051	3074 3049 3045 3044	3088 3074 3051 3051	2952
Symm. Str. C2'H_2 (100 trajectories)	2897	2942	3049 2924 2959 2913	2992 2972 3014 2981	2890
Str. C6=O (1 trajectory per mode)	1581	1553	1583 1587 1561 1555	1660 1669 1724 1667	1663
dG RDM (1trajectory per mode)	1540	1568	1530 1517 1540 1520	1542 1570 1567 1564	1582
			MAE	63 cm^{-1}	

4.3.3 Semiclassical spectra

So far it has been considered only a classical nuclear framework to sample the Born-Oppenheimer surface of the system. In this framework the energy of the trajectory is ideally fixed during the dynamics and only the accessible configurations of the phase space will be sampled. Short-time trajectories have ben employed and the sampled phase space in some cases could be insufficient. Propagating longer in time the MD simulations seems to be an appealing and easy solution, but this kind of approach brings in additional issues since more and more energy will be transferred to low frequency modes and even rigid rotations due to numerical inaccuracies and energy leakage. This would lead to a less accurate spectrum. One solution which was found to be helpful is to run more trajectories with same energy, as shown previously. Another solution is to consider an approximate quantum mechanical evolution of the system, as in the MC-DC-SCIVR method. [86, 72, 73] In this case a Gaussian wavepacket is propagated in the phase space, meaning that even by means of a single trajectory a wider area with respect to a classical trajectory is sampled. Since the two low frequency modes are strongly harmonic and in good agreement with the expected results, the focus is set again on the symmetric and asymmetric C2'H_2 stretches.

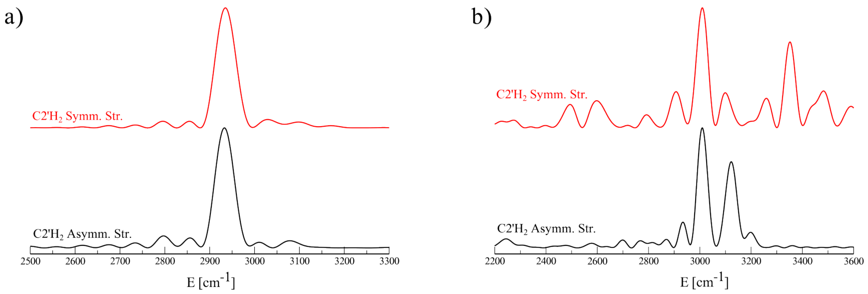

Fig. 4.12 2'-deoxyguanosine semiclassical spectra of the asymmmetric and symmetric stretching of the C2'H$_2$ group in gas (left) and water solution (right)

The analysis is started again by considering the 2'-deoxyguanosine molecule. For the gas phase calculation to partition the system into subspaces we use the average Hessian on all the Hessians along the trajectory. [72] For the water box system the average Hessian is calculated starting from fifteen Hessians uniformly distributed along the trajectory. For the gas phase system we employ a bidimensional subspace in which the asymmetric and symmetric stretches are present. This means that these two normal modes are strongly coupled along the dynamics, and could also explain why only a large number of trajectories is able to reproduce a separation of the two signals.

The MC-DC SCIVR spectrum of 2'-deoxyguanosine in gas phase (figure 4.12 panel a) shows two signals that are nearly degenerate, which, similarly to the QCT case for the same molecule, is due to the fact that asymmetric/symmetric modes are strongly coupled to each other. Moving on to the water box system, we choose two monodimensional subspaces for both modes. By looking at the spectrum (figure 4.12 panel b) for the asymmetric mode a double peak is present, with the most intense peak still degenerate with the one of the symmetric mode (upper part of panel b). In this case by changing the initial conditions as done with 2'-deoxyguanosine, it was possible to assign the less intense peak in fig. 4.12 b (black line) to the asymmetric stretch mode. It was noticed that by using MC-DC SCIVR to calculate the spectrum a better resolution with respect to the QCT counterpart is obtained. As far as the peak around 3350, we think that is a combination band originated by the C2'H$_2$ symmetric stretch.

Finally, we move to apply the semiclassical approach to the quadruplex employing the same protocol adopted for 2'-deoxyguanosine.

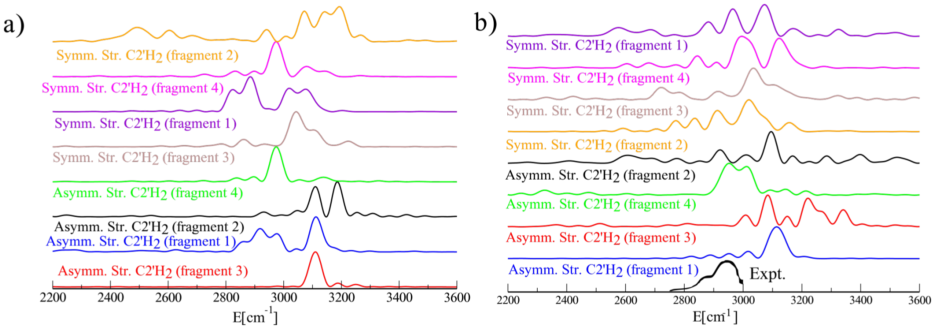

Fig. 4.13 Semiclassical spectra of the quadruplex in gas phase a) and water solution b), for the asymmetric and symmetric stretches of C2'H_2.

By analyzing the spectra in figure 4.13 it is possible to conclude that for the gas phase there is an improvement moving from QCT to SC single trajectory calculations. In particular, it is evident that most of the asymmetric and symmetric signals seem to be split. One problem that arise in this case is that the spectra are not always reporting a single or few peaks, due to the presence of resonances and other vibrational states strongly coupled to the C2'H_2 stretches, which hampers the assignment of the signals. The same is true also for the water box system, in which it is possible to observe that the experimental feature seems to be reproduced reasonably. On a quantitative level the experimental values in this case are about 100 cm^{-1} apart from the theoretical estimates, which seems to be fair since the employment of 100 trajectories gave nearly the same results for this set of modes.

4.4 Conclusions

With this analysis we were able to show how solvation acts differently on different vibrational features and compare them between the molecular and supramolecular arrangement. Solvation cannot be accounted for only by considering simple scaling factors, but it is often necessary to consider every normal mode and molecule explicitly employing a high level spectroscopy method. To corroborate these results we employed the radial pair function, which is able to assess how much a certain part of the molecule is able to interact with the solvent during the trajectory. FF do not provide highly precise descriptions of the PES and, for this reason, the use of FF in the theoretical spectroscopy field should be limited to a qualitative comparison rather than a quantitative one.

In this chapter, we also showed that for some kind of normal modes a single trajectory with the “correct” initial conditions, can lead to a good qualitative agreement with respect to the experiment. Instead for other normal modes a distribution of trajectory run in the same energy shell is needed to increase the agreement with the experiment. By using FF it is possible to run a high number of trajectories without worrying too much about computational overheads. The last point in the conclusions, comes from the fact that we were also able to observe that a quantum mechanical description of the dynamics obtained by a single trajectory, is able to give results similar to what it was obtained by calculating the spectra by means of multiple trajectories.

CHAPTER 5

UNRAVELING WATER SOLVATION EFFECTS WITH QM/MM SEMICLASSICAL VIBRATIONAL SPECTROSCOPY: THE CASE OF THYMIDINE

5.1 Introduction

All biological processes take place in water and, for this reason, water is considered the "universal solvent". Primarily *in vivo,* solvation in water is pivotal for processes like protein folding, DNA recombination, and to drive fundamental metabolic reactions. [242–245] Therefore, the understanding of the structural and dynamical properties of molecular systems solvated by water is one topic which has implications not only on all branches of chemistry, but also on biology, physics, and materials science. Providing an atomistic and fully quantum mechanical understanding of these phenomena is crucial and very valuable.

Several different approaches have been employed in the past to study water solvation. Many of them are based on thermodynamic quantities (specific heat, isothermal compressibility, etc.). In these methods the difference in free energy $\Delta G(T)$ between the gas and the condensed phase state is usually estimated at a specific temperature.[246] While $\Delta G(T)$ is important for distinguishing between hydrophilic and hydrophobic solutes, atomistic insights are not rigorous, and the methodology is cumbersome. In addition, $\Delta G(T)$ values provide only a general picture of the system state. In fact, in this framework, thermodynamic quantities are obtained as difference between state functions and these are intrinsically prone to compensation of errors. The main limitation of a basic thermodynamic approach is that it does not take into account the shape of the PES describing the interaction between nuclei because these types of calculations are based on energy differences obtained from single point energy estimates at the bottom of the potential energy well often even in a harmonic fashion. From an atomistic point of view, these calculations provide information mainly about the molecular geometry at minima. Other techniques, based on a dynamical approach, have been developed. Among those techniques, globally known as enhanced sampling methods, metadynamics and umbrella sampling performed along ‘alchemical’ collective variables, are arguably the most successful and commonly employed method to access thermodynamic information on complex system solvation.[247]

To gain atomistic insight, we choose to employ vibrational spectroscopy. This technique is able to detect the interactions that are responsible for the solvation process because it encompasses the detection of strong chemical bonds as well as long-range weak solute-solvent interactions. These include hydrogen bonding and many other intermolecular interactions originated by the surrounding molecules, such as electrostatic and polarization dispersion interactions or electronic cloud repulsion. All these information are embodied in the PES shape, and the shape of the potential can be re-conducted directly to each atomic component of the molecule, providing in this way a direct atomistic insight. Typically, modes of vibrations will experience a change in frequency when switching from the isolated molecule (gas phase) to the solvated state (solution) arrangement. For these reasons, the use of computational vibrational spectroscopy simulations through molecular dynamics methods allows to directly relate the experimental results with the interactions between the solute and the solvent molecules at atomistic level.

By means of vibrational spectroscopy, one can appreciate blue and red frequency shifts, which are related respectively to a stiffer (increase of the force constant) and floppier (decrease of the force constant) vibrational motion. More specifically, red shifts are usually originated from the weakening of the bond order, as they occur during the formation of hydrogen bonding, for example. Instead, the blue shifts are less frequent and they may be originated by increasing the bond order by adding, for example, ionic interactions on top of covalent ones. Another typical blue shift case is the one involving a bending frequency after a hydrogen bonding formation, since H-bond makes bending more difficult (i.e. stiffer) due to the directionality of the H-bond itself. These are just a few examples of interactions that can be detected by vibrational spectroscopy. Vibrational spectroscopy is more sensitive than electronic spectroscopy, where the energy range is even hundreds of times larger, and it is more difficult to reach the same detail of description. Also, in a typical electronic spectroscopy simulation of large molecular systems, the shape of the nuclear potential is taken into account indirectly. Indeed, it is the statistical average of the electronic transition at these different nuclear arrangements to provide both the frequency values and the intensities of the simulated spectrum.[248–251] This method is the most valuable in these cases though it is not able to capture some important features of nuclear vibrational motions which can be important when studying phenomena like reactivity.

To study the effects of water solvation and provide a prototype of the quantum dynamical behavior of complex solvated systems, we choose a system for which the spectroscopic differences going from solvation by water to gas phase are evident. Thymidine fits this case very well. It is a biologically relevant molecule, and it has been experimentally characterized [252, 253] in the infra-red region. More importantly for our goals, thymidine presents in the gas phase two vibrational stretching signals, one for the $C4 = O$ stretching at $1714\,\mathrm{cm}^{-1}$ and another for the $C5 = C6$ stretching at $1662\,\mathrm{cm}^{-1}$, which are degenerate at $1710\,\mathrm{cm}^{-1}$ in water solution (see Fig. 5.1c). This vibrational degeneracy is not induced by symmetry and it will provide our qualitative and quantitative accuracy check in the description of the solvation process.

Given this atomistic quantum mechanical scenario, we think that an accurate simulation aiming at reproducing the effects of water solvation should be based on *ab initio* electronic structure calculations (QM) and reproduce nuclear quantum effects by vibrational dynamics. Due to the nature of the problem, it would be desirable to apply this approach not only to the solute but also to all the solvating water molecules. Since this is not possible, in this work we adopt a QM/MM approach, where the accuracy of the solvent is downgraded, the Molecular Mechanics (MM) part, to the level of the AMOEBA FF potential to describe the water solvent.[254–257] This is expected to be still an accurate approach since previous FF-based simulations of large solvated systems showed the importance of the interaction energies in solvation,[258] and the presence of gas-to-water solvatochromic shifts.[259]

Nuclear quantum effects are reproduced by employing the Divide-and-Conquer Semiclassical Initial Value Representation (DC SCIVR) molecular dynamics method (eq. 2.48).[114, 131, 260, 208, 261] We think it is important to include quantum mechanical effects, especially the zero point energy one, in our molecular dynamics simulations because results on similar systems featuring strong hydrogen bonding have demonstrated that a quantum description of the nuclei was certainly needed to obtain accurate results.[262–266] Furthermore, NQEs have been observed to be important also in cases involving the motion of heavy atoms.[267, 268, 16] More specifically for our system, the presence of NQEs in small to large clusters and bulk water has been studied from different perspectives[269], and in all cases the inclusion of quantum mechanical effects allowed to reproduce the experimental results.[270–272] In particular, in vibrational spectroscopy, it was previously proven that only a quantum mechanical simulation is able to reproduce all the main experimental features of the liquid water IR spectrum, i.e. including the bending-libration combination bands.[42, 132]

The goal of this chapter is to test different solvent models using both implicit and explicit methods. This helps us not only observe which kind of potential returns the best results compared to the experiment, but it also sheds light on the nature of the interactions occurring between the solute and the solvent.

As a case of study we consider the gas-to-water solvatochromic $\nu\,(\mathrm{C6{=}C5})$ and $\nu\,(\mathrm{C4{=}O})$ shifts of thymidine, where the atomic labels are reported in Fig.5.1(c).The whole idea of the work is well summarized in Fig. 5.1, where we start from the bulk system, featuring many atoms and molecules interacting with each other (panel a). Then, using trajectory analysis with different models of solvent it is possible to understand the main sites of interactions (panel b). Finally, by analyzing the data, a clear atomistic vision of the problem is delivered (panel c).

5.2 Methods

As anticipated, we employ a QM/MM potential, where the QM subsystem is treated at the level of B3LYP/6-31G* density functional theory [273–278] with Grimme

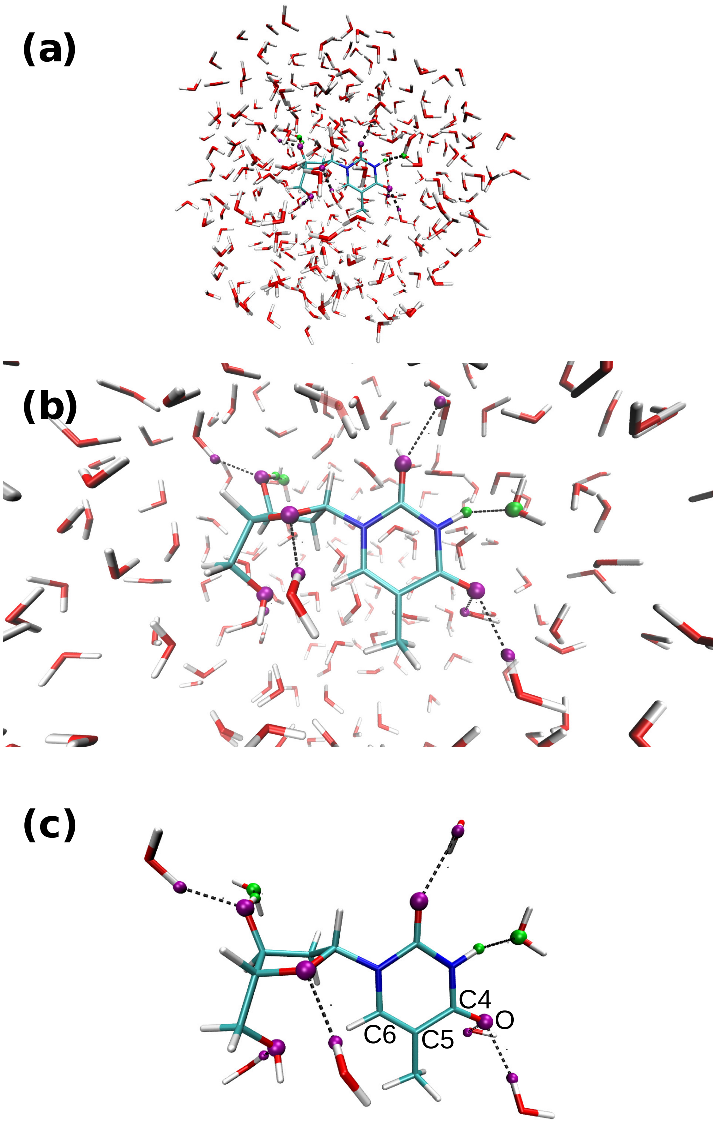

Fig. 5.1 Atomistic representation of thymidine in water solvent. Panel (a) is the full simulated system. Panel (b) is a close up picture showing that very few molecules are directly interacting with thymidine at each time-step. Panel (c) represents the thymidine H-bonded water molecules at given time-step.

dispersion corrections.[279] The MM part is composed by all the solvating water molecules and these are described by the AMOEBABIO18 force field. The QM/MM method is implemented by interfacing a modified in-house development version of Gaussian,[280] with the molecular mechanics Tinker software suite.[236, 281–283]

To prepare the system, a sphere with 15 Å radius filled with water molecules was generated using the Packmol tool. [284] The number of water molecules was chosen to reproduce the density of liquid water. With the TINKER [236] software suite repulsive walls were put on the edge of the solvation sphere, and the optimization of the system was done. Subsequently, the thymidine optimized geometry was inserted in the water sphere, and an optimization with the AMOEBABIO18 [254] force field of the water molecules was carried on. For the QM/MM system, a further full optimization is made.

The QM/MM potential can be implemented in many ways,[285–293] the main difference stands in the way the interactions between the MM and the QM parts are described. The one we employed implements the most sophisticated scheme of QM/MM embedding, known in literature as polarizable embedding. In this method, the MM part can polarize the QM subsystem and vice versa.[255, 256, 281] This QM/MM set-up showed encouraging results in photochemistry when applied to photoreceptive protein systems.[294, 295] A complete description of the QM/AMOEBA implementation and methods can be found in ref. [255, 256]. Specifically, within this framework, the total energy of the system with nuclear configuration **Q** is expressed as:

$$E(\mathbf{Q},\mathbf{P},\boldsymbol{\mu}_d,\boldsymbol{\mu}_p) = E_{QM}(\mathbf{Q},\mathbf{P}) + E_{env}(\mathbf{Q},\mathbf{P},\boldsymbol{\mu}_d,\boldsymbol{\mu}_p) \tag{5.1}$$

where both the QM potential term (E_{QM}) and the MM one (E_{env}) are functionals of the system geometry (**Q**) and the density matrix **P**. In addition, the environment depends on two sets of $\boldsymbol{\mu}_d$ and $\boldsymbol{\mu}_p$ dipole moments, which are generated respectively by the direct electric field ($\mathbf{E}_d$) and the polarizable electric field ($\mathbf{E}_p$). The QM term (E_{QM}) is obtained through Self Consistent Field (SCF) techniques, while E_{env} is defined as follows:

$$E_{env}(\mathbf{Q},\mathbf{P},\boldsymbol{\mu}_d,\boldsymbol{\mu}_p) = E_{FF}(\mathbf{Q}) + E_{pol}(\mathbf{Q},\mathbf{P},\boldsymbol{\mu}_d,\boldsymbol{\mu}_p) + E_{QM/MM}(\mathbf{Q},\mathbf{P}) \tag{5.2}$$

where E_{FF} is the sum of the classical FF terms without the electrostatic term, E_{pol} is the polarization energy, and $E_{QM/MM}$ is a coupling term between the QM and MM part containing the permanent multipoles. It is the E_{pol} term to encrypt the mutual polarization between the QM and the MM part. This term contains the definition of polarization energy as defined in AMOEBA but in a variational way[296]. The minimizers of the functional are the direct and polarization dipoles. This potential term also includes the contribution of the interaction with the QM electric field which is

$$E_{pol}(\mathbf{Q},\mathbf{P},\boldsymbol{\mu}) = \frac{1}{2}\boldsymbol{\mu}_d^T \mathscr{T} \boldsymbol{\mu}_p - \frac{1}{2}\left(\boldsymbol{\mu}_p^T \mathbf{E}_d + \boldsymbol{\mu}_d^T \mathbf{E}_p\right) - \frac{1}{2}\left(\boldsymbol{\mu}_p + \boldsymbol{\mu}_d\right)^T \mathbf{E}_{QM}(\mathbf{Q},\mathbf{P}). \quad (5.3)$$

A complete description of the QM/AMOEBA implementation and methods can be found in ref. [255, 256]. The FF calculations have been carried out using AMOEBABIO18,[254, 257, 236] which includes the polarizability by means of a sophisticated approach exploiting a self-consistent procedure developed by Thole.[297, 298] An extensive examination of the factors that led us to choose this FF as the most suitable one for vibrational spectroscopy of these systems can be found in a previous work done by Gabas et al..[131]

Vibrational spectra are computed by QCT and classical MD when employing an MM only potential, as described in chapter 3. Instead for the QM/MM simulations, initial conditions for the trajectory were chosen according to equation 2.44, with n_j set equal to zero, and θ_j equal to $\pi/2$, for all the normal modes. A 3000-step NVE trajectory with 0.2 fs timestep was propagated, and Hessian matrices along the trajectory were calculated every 100 steps. The calculated matrices along the trajectory are used to divide the system in vibrational subspaces. The elements of the monodromy matrix along the trajectory are then calculated by using the gradient method described in section 2.3.1. The semiclassical vibrational spectra is obtained by applying equation 2.48.

For the PCM calculations, the optimization of the thymidine molecule was done at the same level of theory used in the simulation with the explicit solvent, with the addition of the PCM solvent implemented in Gaussian 16. [299–303, 248, 304]The NVE MD simulation was then carried out with the same software and the same number of steps and time-step as before. The initial conditions are set in the same way as the QM/MM run. In this case, the second derivative matrices along the trajectory were evaluated at each step.

5.3 Results

We start by simulating the system in Fig.5.1(a) using a FF description for both thymidine and water. We employ both classical and QCT MD with AMOEBA FF following both NVE and NVT procedures, and compare these results with the experiment, as reported in Fig.(5.2). Both the experiment and the NVT simulation are at 300 K.

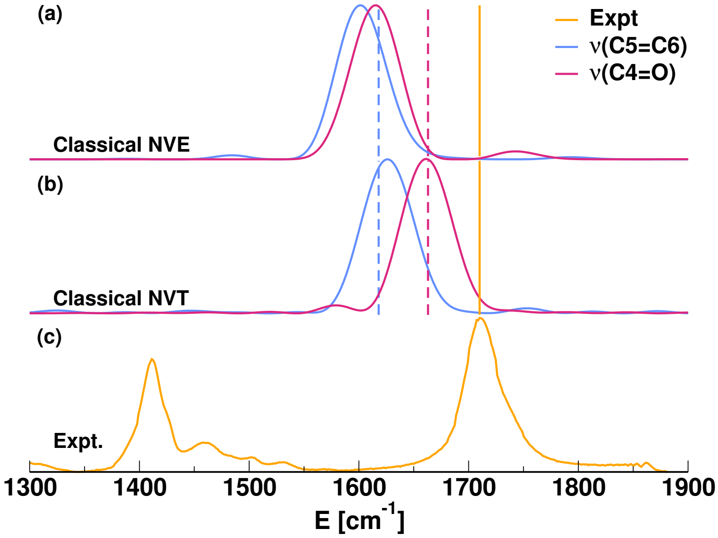

Fig. 5.2 Classical NVE (panel a) and NVT (panel b) MD spectra of the water-solvated thymidine molecule for the C5=C6 and the C4=O bond stretching motions using AMOEBA FF. Vertical dashed lines are the harmonic estimates. The mustard-colored spectrum (panel c) is the experiment where the C5=C6 and C4=O stretching frequency are degenerate.[305] The experimental peak at $\approx 1400\,\mathrm{cm}^{-1}$ is not related to the C5=C6 and C4=O signals under investigation.

The vertical dashed lines in Fig.(5.2) represent the harmonic approximation for the two stretch frequencies and their Mean Absolute Error (MAE) is 70 cm^{-1}, which is quite off the mark compared to the experimental values where the C5=C6 and C4=O stretching frequency are degenerate[253], as obtained also from an extensive isotopic labeling experiment.[305] More importantly, the harmonic approximation cannot reproduce the mode degeneracy, as there is a frequency gap between the two modes (Δ) equals to 45 cm^{-1}. One would expect a better MAE by adding anharmonicity through the NVE simulation. Instead, the accuracy is worse than in the harmonic case. This is probably due to the fact that the force field is parametrized in a way that the harmonic estimate is not a pure one, but it already implicitly includes a certain level of anharmonicity and red shift. When performing the NVE simulation we take this into account again, and the red shift is increased.

However, the NVE simulation closes the gap between the two mode frequencies ($\Delta = 13$ cm^{-1}) getting a picture which is similar to the experimental one. This first comparison is suggesting that the FF is qualitatively accurate since it mimics the right trend, but not quantitative. In the middle panel of Fig.(5.2) we report the NVT classical power spectrum at the experimental temperature. This simulation essentially fails to go beyond the harmonic approximation. This clearly indicates that the NVT single trajectory protocol at room temperature does not sample enough the anharmonic potential energy region. Instead, a single trajectory run at the ZPE energy is able to catch the anharmonicities of the system, as shown in the NVE simulation.

Thus, we need to move to a more accurate potential representation using the QM/MM method, where thymidine is at the DFT level and the solvent is described with FF accuracy, as detailed above. Previous simulations on similar systems are encouraging and showed that the DFT level of theory is enough for getting accurate vibrational frequencies.[131, 306, 134]

When we apply the QM/MM semiclassical (DC-SCIVR and DFT/AMOEBA) scheme to the explicitly solvated thymidine system of Fig. 5.1(c), we obtain the power spectra reported in Figure 5.3. Specifically, in panel (a) of Fig.(5.3) we show the convolution of the ν(C5=C6) and ν(C4=O) simulated signals to be compared with the experimental one reported in panel (c) of Fig.(5.3). In this case, the frequency value is very accurate compared to experimental signal ($1700\,\mathrm{cm}^{-1}$ *vs* $1710\,\mathrm{cm}^{-1}$) and our simulated bandwidth at half maximum is about $70\,\mathrm{cm}^{-1}$ compared to about $45\,\mathrm{cm}^{-1}$ of the experiment. The larger width is mainly due to the facts that our method employs a Fourier transform of a short, finite-time evolution and that we are simulating a power spectrum, so other quantum mechanical transitions different from the fundamental ones, but coupled to them, may contribute to increase the width of the computed band. We did not want to spoil our time-dependent calculations, which provide a physically-based bandwidth, using unphysical filtering or Lorentzian fittings. We can better appreciate how our semiclassical QM/MM mimics the correct physics of solvation by looking at panel (b) of Fig.(5.3), where thymidine ν(C5=C6) and ν(C4=O) signals are reported separately both in gas-phase (dashed line) and in the solvated system (continuous line). DC-SCIVR DFT/AMOEBA shows that in water the Mean Absolute Error

(MAE) from the experiment is only 15 cm^{-1}, and the frequency gap is greatly reduced ($\Delta = 12$ cm^{-1}). Overall, these results represent a significant improvement in terms of accuracy compared to the full FF approach.

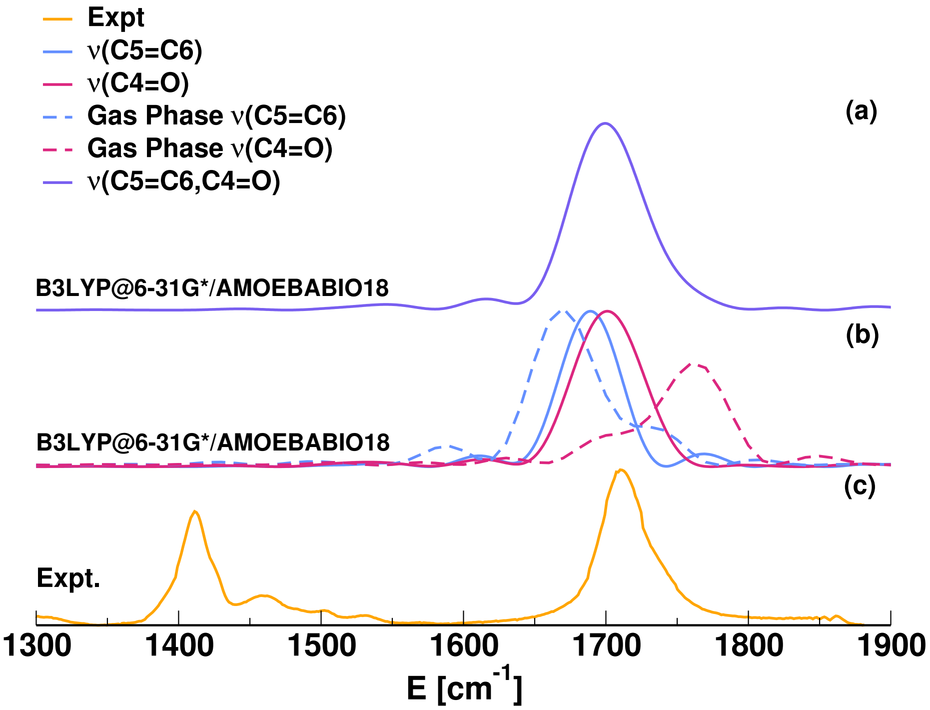

Fig. 5.3 Semiclassical (DC SCIVR) QM/MM power spectra for the C5=C6 and C4=O bond stretches of water-solvated thymidine. QM at DFT-B3LYP/6-31G* level of theory and MM at the level of AMOEBABIO18. Panel (a): The convoluted ν (C4=O) and ν (C5=C6) simulated signal. Panel (b): The separated ν (C4=O) and ν (C5=C6) signals for gas-phase (dashed lines) and water solvated (continuous line) thymidine. Panel (c): The mustard-colored experimental spectrum showing a degeneracy of the two C5=C6 and C4=O stretch frequencies at 1710 cm^{-1}.

We now try to understand how the different interactions at play influence the accuracy of the simulation, and what the peculiar properties of water solvation are. We achieve these goals by checking different models for the MM potential. We start from the TIP3P water model,[307] in which the potential energy of every molecule is represented by a harmonic bond and angle term. Non-bonding interactions are modeled by punctual charges placed on the atomic positions, and the van der Waals (VDW) interactions are accounted for by a 12-6 Lennard-Jonnes (LJ) potential. The spectrum is reported on panel (a) of Fig. (5.4). The limited flexibility and the lack of polarization of this model potential is causing the opposite effects of water solvation. The ν (C4=O) stretching frequency is blue-shifted at almost $1800\,\mathrm{cm}^{-1}$ while the ν (C5=C6) signal cannot be easily identified. In a second method, we significantly increase the quality of the description of intermolecular interactions, and the potential energy of water molecules is modeled by means of the AMOEBA FF. This means that anharmonic stretching and bending terms are considered together with atomic multipoles up to the quadrupole. In addition, 1,3 intermolecular interactions are modeled by the Urey-Bradley potential,[308] and the VdW interactions have a functional form similar to the LJ potential. Here, however, we have switched off the polarization parameters. This means that the MM subsystem cannot be polarized by the QM. This case is reported in panel (b) of Fig. 5.4 where the ν (C4=O) stretch frequency is red-shifted by a small amount with respect to the gas phase, i.e. up to $1750\,\mathrm{cm}^{-1}$. The ν (C5=C6) frequency is left invariant compared to the gas-phase signal and no blue shift solvation effect is reproduced. In this case, the MAE (44 cm^{-1}) and the Δ parameter (88 cm^{-1}) are far away from the correct physical description of the solvation process. Finally, in a third approach the solvent is represented as a continuum according to the Polarizable Continuum Model (PCM). This case is reported in panel (c) of Fig.(5.4) and the accuracy is comparable to our best QM/MM result with a MAE of (5 cm^{-1}) and a Δ of (10 cm^{-1}). This definitely proves that it is the reciprocal polarization between the solute and the solvent to mainly characterize water solvation peculiarities. In fact, this implicit model of solvation mainly focuses on reproducing the electrostatic and polarization effects that the solvent exerts on the central molecule and vice versa. A comparison between all the run at the different level of theory can be found in table 5.1.

5.4 Discussion

The results suggest that the issue of deciphering the nature of solute-water solvent interaction is a challenging one, and that only accurate spectroscopic techniques can detect the roles of classical and quantum contributions. The classical-like terms are those of the type of electrostatic interactions, while the exclusively quantum interactions are mainly electron cloud repulsion and nuclear zero-point energy effects. More specifically, the accuracy of the PCM approach shows that the polarization and the consequent electrostatic interactions are essential to reproduce the mechanics of water solvation. This is confirmed by the fact that no significant

Table 5.1 Summary the calculated frequencies for the different levels of theory in cm^{-1}

	Harmonic			
	Str. C5C6	Str. C4O	MAE	Δ
B3LYP@6-31g*/AMOEBA	1720	1738	20	18
B3LYP@6-31g*/AMOEBA (no pol)	1711	1767	29	87
B3LYP@6-31g*/TIP3P	1719	1806	52	87
B3LYP@6-31g*/PCM	1709	1743	11	34
AMOEBABIO18	1619	1664	69	45
	Quasiclassical Trajectory			
	Str. C5C6	Str. C4O	MAE	Δ
B3LYP@6-31g*/AMOEBA	1684	1695	20	11
B3LYP@6-31g*/AMOEBA (no pol)	1663	1748	42	85
B3LYP@6-31g*/TIP3P	1691	1780	44	89
B3LYP@6-31g*/PCM	1699	1722	11	23
AMOEBABIO18	1612	1618	95	5
	MC DC SCIVR			
	Str. C5C6	Str. C4O	MAE	Δ
B3LYP@6-31g*/AMOEBA	1689	1701	15	12
B3LYP@6-31g*/AMOEBA (no pol)	1660	1748	44	88
B3LYP@6-31g*/TIP3P	1687	1791	52	104
B3LYP@6-31g*/PCM	1660	1748	5	10
AMOEBABIO18	1621	1634	82	13
	Experiment			
	Str. C5C6		Str. C4O	
	1710		1710	

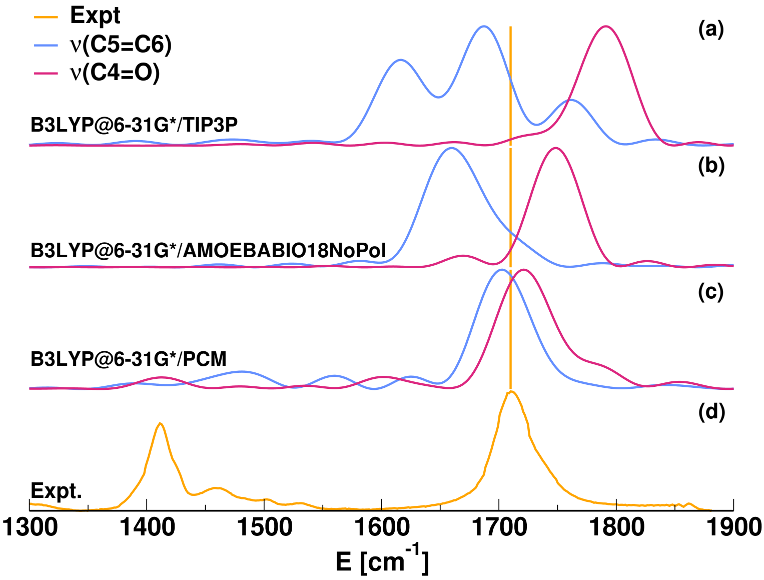

Fig. 5.4 Semiclassical power spectra for the ν(C4=O) and ν(C5=C6) stretch signals. Panel (a) refers to the QM/TIP3P solvent model. Panel (b) refers to the QM/AMOEBABIO18 scheme without polarization, and panel (c) refers to the PCM implicit model of the solvent. Panel (d) is the experimental spectrum.

difference in the ν(C5=C6) and ν(C=O) frequencies is observed in $N,N-$DMF solution compared to the gas-phase one.[253]

To further corroborate at the atomistic level this claim, we computed the average RDF [240] between the water molecules and both $C4-O$ and $C5-C6$ atoms.

By observing the calculated RDFs in figure 5.5, it is possible to observe that by removing the polarization from the MM part, the water molecules tend to stay more distant from the thymidine molecule. By impoverishing the electrostatic description of the solvent, like in the QM/TIP3P case, it is clear that the solvent molecules tend to be even more distanced with respect to a multipolar description like in the QM/AMOEBA case with no polarization included. This could be one of the reasons why the non polarizable QM/MM models reproduce a spectroscopic behavior similar to the isolated thymidine molecule.

We also performed a search for directional interactions along the QM/AMOEBA trajectory using the MDAnalysis library. [309, 310] The search has been made for two cases when the thymidine atoms serve as acceptor (O and N atoms involved) and water acts as a donor (H atoms involved), and vice versa. A first search for interactions was made by setting a distance cutoff of 2,5 Å and an angle cutoff

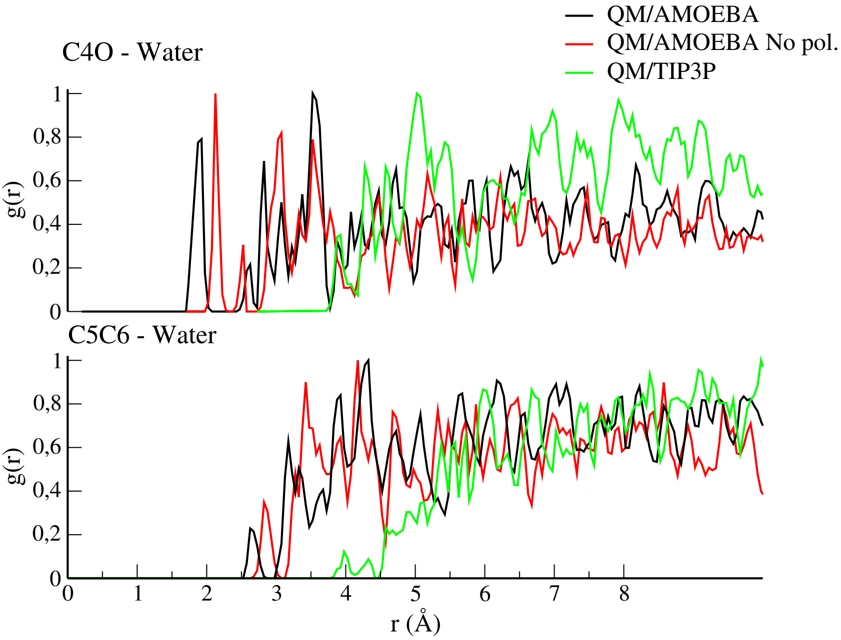

Fig. 5.5 Radial Distribution Function calculated between C4-O and water molecules (upper panel) and between C5-C6 and water molecules (lower panel). The calculations have been carried out for all of the tested QM/MM approaches.

of 170°, which means that all of the nonbonded interactions between the selected group of atoms with a distance greater than the cutoff are automatically excluded. The angle cutoff excludes all the nonbonded interactions where the donor-hydrogen-acceptor angle value is below the cutoff. This first search led to zero interactions found and for this reason, less severe parameters were tested. It was observed that by elongating the distance cutoff and keeping the angle cutoff the same still no interactions were found. Finally by setting the distance cutoff to 3.0 Å and the angle cutoff to 120° some interactions were observed.

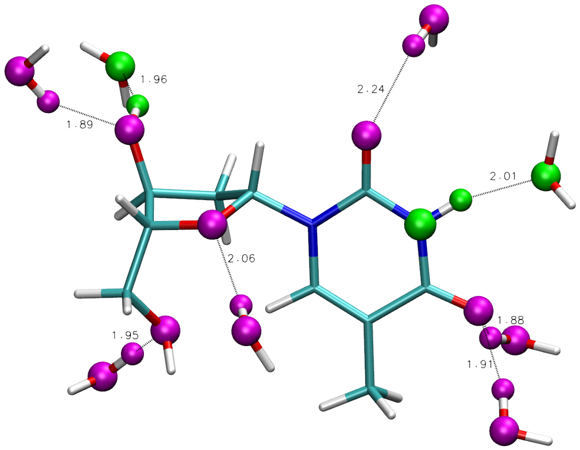

Fig. 5.6 Picture of the thymidine molecule in the minimum geometry where hydrogen bonds are highlighted as purple for acceptors and green for donors

This set of search parameters actually corroborated the hypothesis that the interactions in this study case are not strongly directional.

Moving to the atomistic details, our simulation allows us to appreciate how the blue-shift of the $\nu\,(\mathrm{C5{=}C6})$ value is mainly due to the presence of electron cloud repulsions during the quantum molecular dynamics motion, which causes the C5=C6 potential interaction to be stiffer compared to the gas phase one. In other words the natural packing present in the liquid phase is at the origin of the blue-shift of the $\nu\,(\mathrm{C5{=}C6})$ stretch. This is not only a steric matter but also a quantum mechanical one, since large amplitude vibrations in solution would cause the electronic clouds to partially overlap. To quantify this consideration, we employ the symmetry-adapted intermolecular perturbation theory (SAPT) [311] with the MOLPRO suite of packages [312] for the calculation of the electronic exchange energy between molecular fragments. In our case one fragment is represented by the entire thymidine molecule, and the other by the water molecules nearest to thymidine, as reported in the left panel of Fig. 5.7. Specifically, it is an H-atom interacting with the thymidine C=O group, which is the nearest point of contact between fragments (dotted line in the left panel of Fig. 5.7). Considering that this atom is vibrating much faster than the rate at which the two molecules (thymidine and water) are adjusting, we calculate the one-dimensional potential reported on the right panel of Fig. 5.7. This potential is anharmonic and differs from a Morse (blu line) or harmonic (red line) approximation. Using sinc-DVR,[181, 313] we calculate the exact one-dimensional ground state vibrational eigenvalue and eigenfunction for these potentials and the quantum delocalization (gray shadow region) of the proton from the quantum root mean squared displacement evaluation, also reported in the left panel. The SAPT allows us to estimate the exchange energy between fragments, also denoted as Pauli repulsion, as the sum of three contributions of different type and order, i.e $E_{exch} = E^{(1)}_{exch} + E^{(2)}_{exch-ind} + E^{(2)}_{exch-disp}$, where *ind* and *disp* stands respectively for “induction” and “dispersion”. The values of exchange energy are reported on the Table on the right panel of Fig. 5.7 for the different geometries just described, i.e. the starting equilibrium geometry (“Equilibrium”), the geometry at which the water molecule is the nearest to thymidine (“Stretched”) and those obtained by the quantum proton delocalization.

We find that the stretched molecular dynamics simulation geometry is experiencing a +2.1% increment in electronic repulsion over the total contribution coming from all the electrons of the fragments, and this is mainly originated from the interacting H-atom. With the inclusion of the quantum H-atom delocalization the repulsion is raised at almost +3.8%. We deem this increment to be significant in electronic structure theory, since it is due to the delocalization of a single atom only. Thus, we conclude that, even if the water molecules are not directly interacting with the C=C stretch, it is this type of interaction together with the dynamical coupling of the water solvent to be responsible for the C=C blue shift.

Clearly, this electronic steric issue is somehow true for any kind of stretches of the solvated molecule, since there is less room for vibration in water solution than in the gas phase. However, for the $\nu\,$(C4=O) stretch, a red-shift is prevailing because of the interplay of other electrostatic interactions. In this regard, it is interesting to look at the RDF associated to our NVE trajectory reported in Fig. 5.5. It is possible to see how in the TIP3P water model, the packing is greatly reduced with respect to the AMOEBA FF more precisely by an amount greater than 1Å. We think that this observation explains not only the larger frequency gap, which is about the same as in gas phase, but also the wrong sign of the shift of the $\nu\,$(C4=O). The

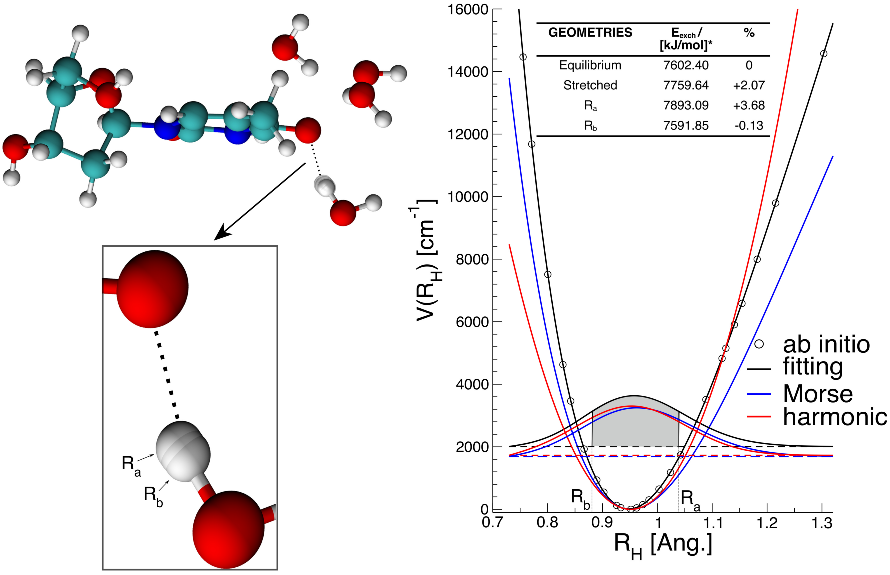

GEOMETRIES	E_{exch} / [kJ/mol]*	%
Equilibrium	7602.40	0
Stretched	7759.64	+2.07
R_a	7893.09	+3.68
R_b	7591.85	-0.13

Fig. 5.7 Thymidine atomic solvation interactions. Left panel shows a molecular dynamics snap-shot with the most interacting, i.e. the nearest, water molecules. The water H-atom interacting with the thymidine C=O group is highlighted. Right panel shows the one-dimensional potential energy experienced by the highlighted H-atom at different approximations, together with the exact ground vibrational eigenfunction. The root mean squared displacement is the shadow area. Upper right Table: The ab initio exchange electronic energy contribution for different geometries together with the percentage variation with respect to the equilibrium geometry.

packing is also reduced for the FF when the polarization is removed, but for a fewer amount (~ 0.4Å). This could explain the smaller amount of both red- and blue-shifts observed with this computational set-up. Instead, in the full QM/AMOEBA computational set-up of panel (b) of Fig. 5.3, we account for the mutual polarization of the MM and QM portions, showing that it plays a crucial role in aqueous systems. Specifically, what makes the difference between the accurate results of panel (b) of Fig. 5.3 and those of panel (b) of Fig. 5.4 is the fact that to reach accuracy we have to explicitly set-up a so-called polarizable embedding (PE) scheme where the MM force field contains additional terms accounting for the polarization effects induced by the QM density.

5.5 Conclusions

In the present chapter, we have shown that the QM/MM Semiclassical method can reach spectroscopic accuracy in the calculation of IR (and Raman) frequencies of biological molecules in water solution. Specifically, by means of our DC- SCIVR quantum dynamics approach coupled with a polarizable QM/MM representation of the PES, we were able to get very close to the degeneracy of the thymidine ν(C4=O) and ν(C5=C6) stretch signals typical of water solution, and showed that indeed quantum effects and anharmonicities play an important role in determining the dynamical behaviour and the spectroscopic features of water solvated molecules.

We were able to indirectly detect the net electronic cloud repulsion effects when performing nuclear quantum dynamics. This shows that the dynamics of biomolecules in water solution experiences not only H-bonds, multipoles, and short and long range polarization interactions but also packing effects. These effects are originated from the fact that there is fewer room for the nuclear wavepacket to vibrate given the electronic clouds superpositions and this explains the observed spectroscopic blue-shift.

CHAPTER 6

A TIME AVERAGED SEMICLASSICAL APPROACH TO THE COMPUTATION OF NONADIABATIC VIBRONIC ABSORPTION SPECTRA

6.1 Introduction

The employment of semiclassical methods to approximate quantum mechanical exact results and experimental ones has been proved to be successful in a large number of problems of different nature. In particular, in the previous chapters it was displayed how the latest developments opened the way for semiclassical calculations of vibrational spectroscopies of molecular systems with a high number of degrees of freedom. [42, 132, 134, 133] As already anticipated in the first chapters of this manuscript, there are numerous reasons that makes semiclassical molecular dynamics particularly fit for this kind of task. One of the most obvious ones are that since the SCIVR is a trajectory based approach, the potential does not have to be written in a specific way, meaning that any kind of Hamiltonian and potential energy function can be employed. Though, it is also true that MD *per se* is limited on the simulations of processes within Born-Oppenheimer approximation. This obviously poses the same limit to the applicability of the SCIVR too. To overcome this limitation, different methods to expand classical MD over the single potential energy surface evolution have been developed. [314, 151, 315] One remarkable step in this field is the introduction of the Fewest Switches Surface-Hopping (FSSH) by John Tully, [88] in which a swarm of classical trajectories are allowed to jump from different adiabatic PESs using a stochastic algorithm. In this way, classical trajectories should be able to emulate the branching of the wavepacket in regions of strong coupling between two or more electronic states. Since its original formulations many improvements have been developed in order to correct known issues such as, energy conservation and overcoherence.[150, 316] A semiclassical approach to surface-hopping was also developed by Herman, [155, 317] differently from the FSSH a rigorous mathematical derivation is followed. Making this approach surely more solid but at the same time quite more complicated when it comes to application. Even though surface-hopping methods are in principle compatible with the SC IVR formalism, the hopping events adds a further element of numerical instability to the already delicate numerical stability of the IVR method.

What instead was observed to be a successful choice when it comes to expanding semiclassical methods to the nonadiabatic regime, is to treat the electronic and the nuclear dynamics on an equal footing.[91, 92, 318] More precisely, by introducing the concept of mapping H. D. Meyer and W. H. Miller and later G. Stock and M. Thoss, (MMST) allowed to map the problem of explicitly solving the electronic TDSE into solving the classical Hamilton equations of motion i.e. allowing to use classical molecular dynamics to simulate nonadiabatic processes without the need of stochastic jumps. [62, 161] To these days mapping methods are still being intensively developed [319, 320, 159, 321–324] and applied to different kind of problems. [180, 156, 106, 325, 326, 108, 327, 328] To recover quantum effects from this "quasi-classical" nonadiabatic framework, mapping PI methods [329, 330] have been developed to compute quantum mechanical correlation functions. The SCIVR method can be employed too for the same task, [331, 107, 125, 126] though the presence of the double phase-space integral makes this task cumbersome if not virtually impossible, unless mixed quantum-classical procedures [54] or partial/full linearization approximations are introduced.[332, 333, 109–111, 124]

A less explored field both in terms of development and applications for the semiclassical nonadiabatic dynamics is about spectroscopy.[173] In fact, it is known that in molecular systems, both absorption and emission spectra can display important nonadiabatic effects.[334, 335, 179, 170] Their manifestations in practical terms is usually observed experimentally and theoretically as absorption line broadening and/or splittings but also as simple frequency shifts. Thanks to more detailed investigations on model systems it was also possible to observe that vibrationally forbidden transition arises in cases where the coupling between two states becomes important, causing a deviation from the usual regular signal progression caused by the vibronic transitions between the ground and the excited state. (Frank-Condon progression)

During this chapter the method described in section 2.5 will be applied to some model systems.

6.2 Computational details

Since the objective of the chapter is to test a newly developed semiclassical approach to vibronic spectroscopy, for this case we are considering a multi-trajectory approach. This means that the phase space integral in equation 2.114 is evaluated by means of importance sampling Monte Carlo.[119, 120] It can be easily observed, that a natural choice for the probability distribution comes from evaluating at $t = 0$ the square module of the overlap between the reference state and the phase space coherent state.[121] The main difference in this case with respect to the previous works in which the TA SCIVR was employed, is that we are considering an "extended" phase space featuring nuclear $(\mathbf{P}, \mathbf{R})$ and electronic $(\mathbf{p}, \mathbf{x})$ DOFs. One of the practical consequence is that two different probability distributions must considered to sample initial conditions from

$$\left|\left\langle \psi_0 \middle| \mathbf{P}(0), \mathbf{R}(0), \mathbf{p}(0), \mathbf{x}(0) \right\rangle\right|^2 \propto \sum_{j=1}^{N} \left|\left\langle 1_j, \mathbf{0} \middle| \mathbf{p}(0), \mathbf{x}(0) \right\rangle\right|^2 \left|\left\langle \mathbf{P}_{eq}^{(0)}, \mathbf{R}_{eq}^{(0)} \middle| \mathbf{P}(0), \mathbf{R}(0) \right\rangle\right|^2 . \tag{6.1}$$

Since the nuclear wavepacket is chosen to be defined as in eq. 2.25, the probability distribution for the nuclear DOFs is an F-dimensional Gaussian with width proportional to Γ for the positions and Γ^{-1} for the momenta (eq. 2.41). Instead, for the electronic DOFs the probability distribution is defined as

$$\left|\langle 1_j, \mathbf{0} | \mathbf{p}_0, \mathbf{x}_0 \rangle\right|^2 = \frac{1}{2}\left(x_{0,j}^2 + \frac{1}{\hbar^2} p_{0,j}^2\right) e^{-\frac{1}{2\hbar^2}\mathbf{p}_0^T\mathbf{p}_0 - \frac{1}{2}\mathbf{x}_0^T\mathbf{x}_0} , \tag{6.2}$$

which is a radial function featuring nodal planes along the axes of the non-occupated states. The sampling of the function in eq. 6.2 is generally done by rejection sampling, though it is known that such method can lead to slow convergence when dealing with multidimensional integrals. Therefore, in order to accelerate convergence we opted to employ focused initial conditions. The general idea behind it is that since the initial population of each electronic state is known, and bound by the relation $\sum_{l=1}^{N} \rho_{ll}(0) = 1$, it is possible to exploit the relation between the classical population (eq. 2.70) and the action-angle variables (eq. 2.69) to sample initial conditions. It is possible to observe that eq. 2.69 describes a circle of fixed radius equal to $\sqrt{2\rho_{ll}(0)+1}$

$$\begin{cases} p_j(0) & = \sqrt{2\rho_{jj}(0)+1}\sin(\theta) \\ x_j(0) & = \sqrt{2\rho_{jj}(0)+1}\cos(\theta) \end{cases} , \tag{6.3}$$

where θ is selected randomly between 0 and 2π. The employment of such sets of initial conditions is not novel but was already considered in the early development of the mapping methodology. [91, 318, 336] Moreover, Bonella and Coker when considering the entire probability distribution of the semiclassical propagator of the MMST Hamiltonian, found out that the set of initial conditions that matched the steepest descent conditions for the electronic DOFs are the ones sampled from eq. 2.70. A valid argument that would contrast the advantages coming from the employment of focused initial conditions derives from the fact that such simplification could affect the accuracy. While the latter statement is generally true, it was observed that for some model systems [332, 333, 319] and molecular systems, [106] an important accuracy difference is not usually observed.

After each Monte Carlo sample classical trajectories are evolved for a total time T = 50000 a.u. with a timestep $\delta t = 0.1$ a.u.. The propagation of each trajectory is done by means of the MINT algorithm as explained in subsection 2.5.1. For both 1D and higher dimensional systems, we found out that by employing 10000 Monte Carlo samples the final results are generally well converged. Since this chapter is centered on applications with low dimensional model systems, a proper study of ideal initial conditions aimed to minimize the number of samples has not been carried out yet.

A very well known issue that afflicts semiclassical molecular dynamics comes from the need of computing the monodromy matrix elements. In fact, when trajectories display a strongly chaotic (irregular) behavior one or more monodromy elements will increase exponentially along the trajectory. Eventually, if such issue is ignored the propagation of the HHKK propagator becomes unphysical. The usual procedure employed when a trajectory display such behavior, is to discard it in order preserve the final Monte Carlo average or discard all the data of the time evolution after the trajectory is deemed "chaotic", in this way the contribution of the unstable trajectory is weighted properly.[45, 127] One of the more challenging aspects we observed when dealing with trajectories generated by the MMST Hamiltonian, is that most of them tend to exhibit an highly instable behavior that would quickly lead to a non-finite value of the monodromy matrix. Therefore, the two protocols usually employed would be ineffective since will inevitably lead either to a 100% rejection rate or the sampling of only short trajectories. For these reasons, a solution we found to be effective and more practical is the employment of the regularization scheme described in section VIIB of ref. [337], in which the real eigenvalues of the monodromy matrix which are found to be higher than a given threshold are imposed to be equal to zero and then used to re-build a new monodromy matrix. Since the employment of this regularization scheme creates a discontinuity in the time propagation we imposed that the trajectories where this procedure is called more than ten times must be rejected.

6.3 Results

In this section the limits and potentialities of the newly developed NA TA SCIVR will be tested on model systems. Every semiclassical result will be compared with numerically exact data obtained by propagating the time-dependent wavefunction with the split-operator technique.[338] Differently from the study cases displayed in the previous chapters, in order to evaluate the accuracy of this method we need to consider both the agreement in terms of frequency and in terms of relative intensities, since in this ambit they have an important physical meaning.

6.3.1 No coupling regime

Before delving in the main topic of this chapter it is necessary to consider if the MMST Hamiltonian, and the numerical propagation algorithm for the trajectories that is being employed are able to properly catch the main features of the "simpler" system. In this circumstance, the simpler case would be to consider a system in which the diabatic coupling is considered as null

$$\mathbf{V}(R) = \begin{vmatrix} \frac{1}{2}\omega_1^2\,(R - R_{eq_1})^2 + \varepsilon_1 & 0 \\ 0 & \frac{1}{2}\omega_2^2\,(R - R_{eq_2})^2 + \varepsilon_2 \end{vmatrix} , \tag{6.4}$$

where the harmonic frequencies of the two parabolic potentials are $\omega_1 = 0.0045563$ a.u. and $\omega_2 = 0.003645$ a.u., the equilibrium positions have been set as $R_{eq_1} = 0$ a.u. and $R_{eq_2} = 10.0$ a.u.. The two values of the vertical excitation energy have been chosen to be equal to each other $\varepsilon_1 = \varepsilon_2 = 0.036451$ a.u..

To initialize the system, it was chosen that the whole amplitude is completely transferred on state 2, the FC point ($R_{eq}^{(0)}$) is set in way that the initial position has a potential energy equivalent to the energy of the third vibrational level of state 2. The initial value of the wavefunction for the exact propagation has been chosen to be a Gaussian wavepacket centered in the FC point

$$\Psi(R,t=0) = \left(\frac{\gamma}{\pi}\right)^{1/4} e^{-\frac{\gamma}{2}\left(R-R_{eq}^{(0)}\right)^2} \left|2\right\rangle , \tag{6.5}$$

where $\gamma = 0.007$ a.u. is the width factor that will be also employed in the semiclassical calculations. The split-operator propagation has been executed on a symmetric grid of 2000 points defined between $R \in [-200, 200]$ a.u., with time step $\delta t = 0.1$ a.u. for the same amount of time reported in the previous section.

In figure 6.1 it is possible to observe that the spectrum is as expected composed by a simple FC progression in which the highest intensity peak is the one corresponding to the $0_0 \rightarrow 3_2$ vibronic transition. The general agreement between the QM and semiclassical approach is good, especially when considering the position of each vibronic transition. Instead, when the relative intensities are considered, it is possible to observe that the NA TA SCIVR reproduces almost in an exact way the trend observed in the exact spectrum. Though, there are some deviations in the absolute intensity of certain peaks. Since the agreement of this simple case is good both qualitatively and quantitatively, it is possible to consider a more complicated case. Clearly, in this case the employment of the MMST Hamiltonian was not necessary to obtain a simple FC spectrum. Thus, this case serves as a proof that in the limit case where the diabatic coupling is weak or non important for the excited state dynamics, the MMST will be able to return the simple picture.

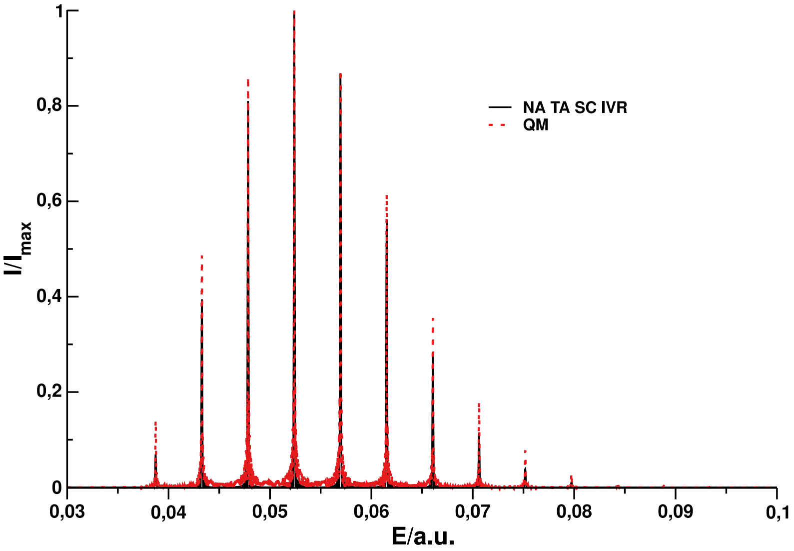

Fig. 6.1 Comparison of the vibronic spectrum of the decoupled harmonic oscillator for system in eq. 6.4 obtained with the semiclassical IVR (black solid line) and the numerically exact one (red dots).

6.3.2 Harmonic potentials with Gaussian diabatic coupling

As a first case of study in the nonadiabatic regime, the same system as before is considered. With the difference that the two states are now coupled

$$\mathbf{V}(R) = \begin{vmatrix} \frac{1}{2}\omega_1^2 (R - R_{eq_1})^2 + \varepsilon_1 & \Delta \\ \Delta & \frac{1}{2}\omega_2^2 (R - R_{eq_2})^2 + \varepsilon_2 \end{vmatrix}, \tag{6.6}$$

where the diabatic coupling $\Delta = 0.020$ a.u. is a constant with the same order of magnitude of the vertical excitations. The system is initialized as in the previous case. Therefore, the only difference stands in the fact that in this case the system will be able exchange amplitude between the electronic states.

In panel a of figure 6.2 it is possible to observe that the spectrum for the system of eq. 6.6, is composed by two splitted FC progressions of oscillators with the same frequency. It is also easy to demonstrate that in such system the distance between the barycenter of the two spectral features is proportional to the diabatic coupling. In other words, the spectroscopic nonadiabatic effects are manifested as a splitting of the FC features together with a change in the separation of the vibronic lines for the state 1 and state 2 features.

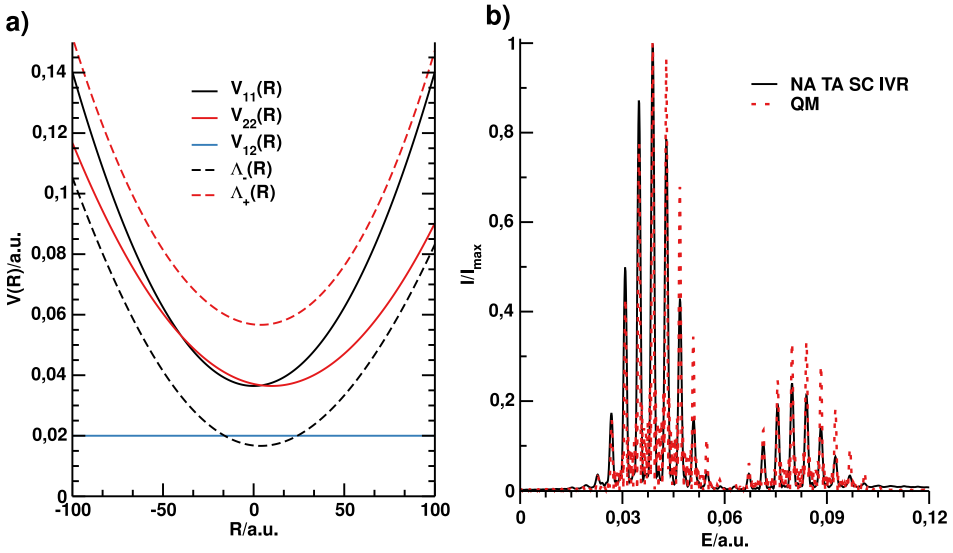

Fig. 6.2 a) Plot of the potential energy surfaces in both the diabatic (black, red an light blue solid lines) and adiabatic representations (black and red dotted lines) obtained by direct diagonalization of the potential. b) Comparison of the semiclassical spectrum (black solid line) with the numerically exact one (red dots) obtained with the split-operator method for the system of eq. 6.6.

Comparing the results obtained from the split-operator propagation with the one from the NA TA SCIVR, it is possible to see that the overall agreement between the QM and semiclassical is generally good. In particular, the vibronic features are observed to reproduced quietly well in terms of frequencies by the NA TA SCIVR. Instead, by looking at the intensities, it is observed that the semiclassical approach catches the right relative intensity for the higher intensity peak, while generally tend to underestimate it for all the other vibronic transitions. This could be due to the fact that the MMST Hamiltonian is not able to reproduce correctly the long time behavior of the electronic populations and coherences, causing differences in the intensity of some absorption lines.

6.3.3 Harmonic potentials with Gaussian diabatic coupling

The case in which the diabatic coupling is a constant is usually uncommon except for condensed phase systems. Therefore, it is necessary to test the method with a localized coupling. In this subsection is considered the same harmonic system of the previous subsections, with the difference that the diabatic coupling is no more a

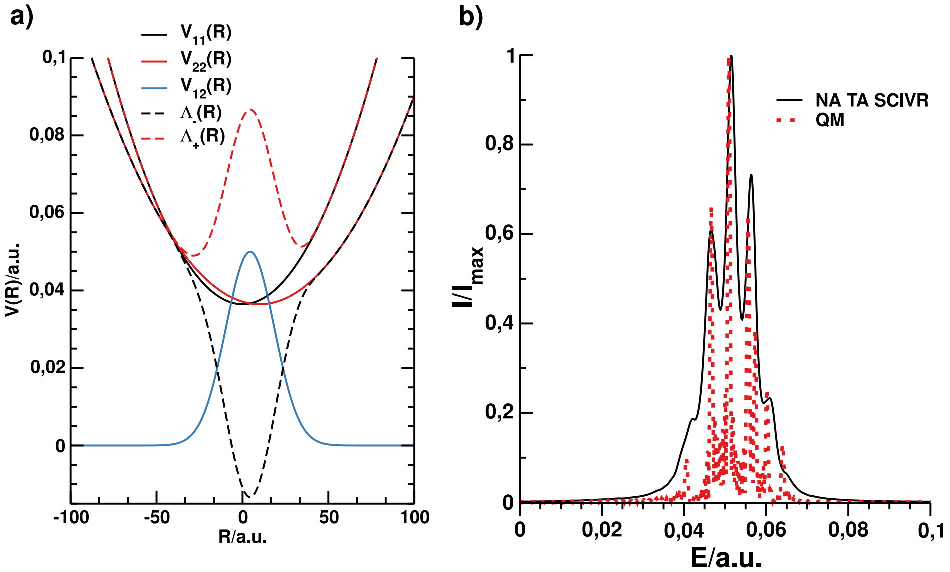

Fig. 6.3 a) Plot of the potential energy surfaces in both the diabatic (black, red an light blue solid lines) and adiabatic representations (black and red dotted lines). b) Comparison of the semiclassical spectrum (black solid line) with the numerically exact one (red dots) obtained with the split-operator method for the system fo eq. 6.6 with Gaussian coupling (eq. 6.7).

constant but a Gaussian centered at the crossing point ($R_c = \frac{R_{eq_1}\omega_1 + R_{eq_2}\omega_2}{\omega_1 + \omega_2}$) of the two diabatic potentials

$$\Delta = \Delta(R) = de^{-c[R-R_c]^2} \, , \tag{6.7}$$

where $d = 0.05$ a.u. and $c = 0.0025$ a.u. are fine-tuning parameters that regulates the strength and localization of the coupling respectively.

Similarly to the previous study case, by comparing the NA TA SCIVR result with the QM one it is noticed again a good agreement in terms of frequency. Also in terms of relative intensities we observe an overall satisfactory agreement. Though, it is also observed that the semiclassical approach fails in predicting the relative peak heights of the two vibronic transitions next the most intense transition. Moreover, the semiclassical spectrum features an anomalous vibronic features enlargement probably due to the fact that the Monte Carlo samples are too different one to each other or a fast decay of the time integral of eq. 2.114.

6.3.4 Two mode model of butatriene cation

An important class of models that was fundamental for the development of spectroscopic methods for nonadiabatic systems, are the vibronic coupling models. In this kind of models the Electronic Hamiltonian is locally diabatized around a conical intersection.Though, since the adiabatic to diabatic switching angle , is position-dependent and must satisfy the curl condition. A series expansion around a reference geometry is necessary to build the diabatic Hamiltonian. Moreover, as pointed out by early works within this field,[90] not all modes contribute in forming the conical intersection and its seam. Thus, in this model is possible to consider a reduced number of modes. In this subsection the vibronic-coupling model of the butatriene cation is employed to test the NA TA SCIVR performance in a two-dimensional system.

In particular, this system describes the conical intersection of the two lowest-lying electronic states ($^2B_{2u}$, $^2B_{3g}$) of the cationic butatriene, and takes as a reference geometry the ground state equilibrium of the neutral molecule.[334] The modes that are observed to contribute the most to the formation of multidimensional intersection, are the central $C-C$ stretch of symmetry A_g (tuning mode) and the torsion on the molecular axis of symmetry A_u (coupling mode), which couples the two ionic states.[339] The second-order vibronic coupling Hamiltonian is defined as

$$\hat{H} = \sum_{J \in \nu_{A_g}, \nu_{A_u}} \left[\hat{T}_J + \frac{\omega_J}{2} R_J^2\right] \mathbb{1} + \begin{vmatrix} E_1 + \kappa^{(1)}_{\nu_{A_g}} R_{\nu_{A_g}} & \lambda R_{\nu_{A_u}} \\ \lambda R_{\nu_{A_u}} & E_2 + \kappa^{(2)}_{\nu_{A_g}} R_{\nu_{A_g}} \end{vmatrix}, \tag{6.8}$$

where ν_{A_g} and ν_{A_u} are the labels of the tuning and coupling modes respectively, $\kappa^{(1)}_{A_g}$ and $\kappa^{(2)}_{A_g}$ are the state specific gradients of the tuning mode and λ is the vibronic coupling constant, E_1 and E_2 the vertical excitation energies. The value of each parameter of eq. 6.8 can be found in the table 6.1.

Since the vibronic-coupling Hamiltonian of the butriene cation is written in normal modes coordinates, the FC point is located at the origin $\mathbf{R}^{(0)}_{eq} = 0$. In this case the initial state to be considered is the neutral molecule in the electronic ground state, which later is photo ionized to the dibatically coupled states. As reported by experimental data [340] the two ionic states are equally populated after ionization. Therefore, both the exact and the semiclassical propagation has been initiated by imposing that one half of the amplitude is initially both on state 1 and 2. Moreover,

Table 6.1 Numerical value in atomic units of the parameters used for the simulation of the two modes model of butatriene cation.[334]

$\kappa^{(1)}_{\nu_{A_g}}$	
-0.0055124	
$\kappa^{(2)}_{\nu_{A_g}}$	
0.0066149	
$\omega_{\nu_{A_g}}$	$\omega^{(1)}_{\nu_{A_u}}$
0.0094726	0.003353
E_1	E_2
0.34728	0.36198
λ	
0.00826859	

to keep the wavepacket narrow in the position space and favor numerical convergence, the width factor for the nuclear DoFs was chosen to be equal to the unity matrix.

For the exact propagation of the wavefunction a bi-dimensional discrete grid of 100 points defined between $\mathbf{R} \in [-10, 10]$ was employed. The initial wavefunction is a Gaussian centered in the FC point of the two populated electronic states

$$\Psi(\mathbf{R}, t=0) = \frac{1}{\sqrt{\pi}} \begin{vmatrix} \sqrt{0.5}e^{-\frac{1}{2}\mathbf{R}^T\mathbf{R}} \\ \sqrt{0.5}e^{-\frac{1}{2}\mathbf{R}^T\mathbf{R}} \end{vmatrix} . \tag{6.9}$$

In the mapped Hamiltonian the state independent potential (V_0) was set as the Harmonic ground state appearing in the diabatic Hamiltonian of eq. 6.6

$$V_0(\mathbf{R}) = \sum_{J \in \nu_{A_g}, \nu_{A_u}} \frac{\omega_J}{2} R_J^2 . \tag{6.10}$$

Finally, for the calculation of the spectrum it was also added to the time-integral a phenomenological dephasing factor $e^{-t/T}$ of $T = 40$ fs.

In figure 6.4 it is possible to compare the quantum mechanical spectrum with the one obtained by means of the NA TA SCIVR. In particular, it is possible to notice that the QM spectrum displays a main feature followed by a crowded series of vibronic transitions. The semiclassical approach seems to be able to reproduce the overall envelope of the exact QM spectrum. Though, it seems that such vibronic

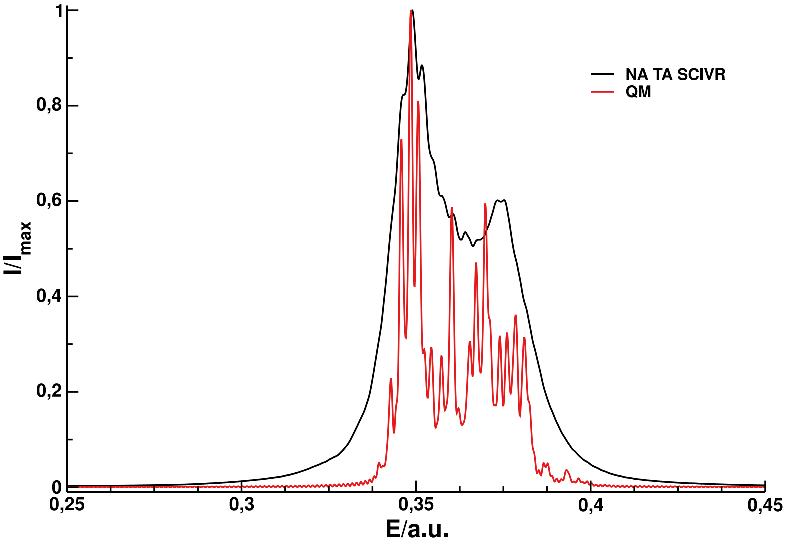

Fig. 6.4 Comparison of the NA TA SCIVR (black solid line) and exact quantum mechanical spectrum (red solid line) for the two modes vibronic coupling model of the butatriene cation.

resolution is not fully reproduced. On the other hand, even if the semiclassical spectrum is composed only by two large bands, it is possible to notice that the relative intensities in the envelope of the vibronic transitions are well reproduced. It is not fully possible to asses the accuracy in terms of frequency since the spectrum is not well vibrationally resolved. From the few features that are identifiable, it seems though that the positions of the bands are in good agreement with the exact spectrum.

6.3.5 Four mode model of pyrazine

As last model system it was considered the four mode vibronic coupling model of pyrazine developed by Woywod et. al. [341] for the symmetry allowed conical intersection between the S_1 and S_2 electronic states

$$\hat{H} = \sum_{J\in G_1,\nu_{10a}} \left[\hat{T}_J + \frac{\omega_J}{2}R_J^2\right]\mathbb{1} + \begin{vmatrix} E_1 + \sum_{J\in G_1}\kappa_J^{(1)}R_J & \lambda R_{\nu_{10a}} \\ \lambda R_{\nu_{10a}} & E_2 + \sum_{J\in G_1}\kappa_J^{(2)}R_J \end{vmatrix} . \quad (6.11)$$

where $G_1 = \{\nu_1, \nu_{6a}, \nu_{9a}\}$ is the group of the three total-symmetric modes that most contributes to the multidimensional intersection between S_2 and S_1 (tuning modes), ν_{10a} is the out of plane bending mode that couples the two electronic states (coupling mode), the other parameters of the potential are summarized in table 6.2.

Table 6.2 Numerical value in atomic units of the parameters employed in the diabatic Hamiltonian of eq. 6.11 for the four modes model of pyrazine.

$\kappa_{\nu_1}^{(1)}$	$\kappa_{\nu_{6a}}^{(1)}$	$\kappa_{\nu_{9a}}^{(1)}$	
-0.0017271273	-0.003542633	0.005857839	
$\kappa_{\nu_1}^{(2)}$	$\kappa_{\nu_{6a}}^{(2)}$	$\kappa_{\nu_{9a}}^{(2)}$	
-0.0073939602	0.004384192	0.001778666	
ω_{ν_1}	$\omega_{\nu_{6a}}$	$\omega_{\nu_{9a}}$	$\omega_{\nu_{10a}}$
0.0046794	0.00272	0.0057592	0.004164
E_1		E_2	
0.15508		0.18558	
λ			
0.006706748			

As in the previous subsection the model in eq. 6.11 was built in mass-scaled normal modes by taking the ground state (S_0) equilibrium geometry as the reference structure, this means that the FC point is again located at $\mathbf{R}_{eq}^{(0)} = 0$. The width parameter, as previously done in a work by Thoss, Miller and Stock (Ref. [173]) regarding the same system, is set equal to the unity matrix also for the nucler DoFs. Therefore, the wavefunction for the exact propagation was initiated as

$$\Psi(\mathbf{R}, t=0) = \frac{1}{\pi} \left| \begin{array}{c} \sqrt{0.25} e^{-\frac{1}{2}\mathbf{R}^T\mathbf{R}} \\ \sqrt{0.75} e^{-\frac{1}{2}\mathbf{R}^T\mathbf{R}} \end{array} \right| , \tag{6.12}$$

where in this case some amplitude is also transferred in S_1, since $n\pi^*$ transitions are usually observed but with a low intensity. As done previously, the state independent potential was set as $V_0(\mathbf{R}) = \sum_{J \in G_1, \nu_{10a}} \frac{\omega_J}{2} R_J^2$. For the spectrum calculations in both the semiclassical and exact calculations a phenomenological dephasing factor $e^{-\frac{t}{T_2}}$, where $T_2 = 30$ fs, is added to account for the experimentally observed ultrafast decay of the population of S_2.

In figure 6.5 the semiclassical result with the numerically exact one are compared between each other. In first instance, it is possible to observe that both the position of the S_1 band (0.14-0.18 a.u.) and S_2 band (0.18-0.22 a.u.) are in good agreement between the QM and NA TA SCIVR. Moreover, in terms of absolute intensities the semiclassical approach is able to catch most of the features of the QM spectrum

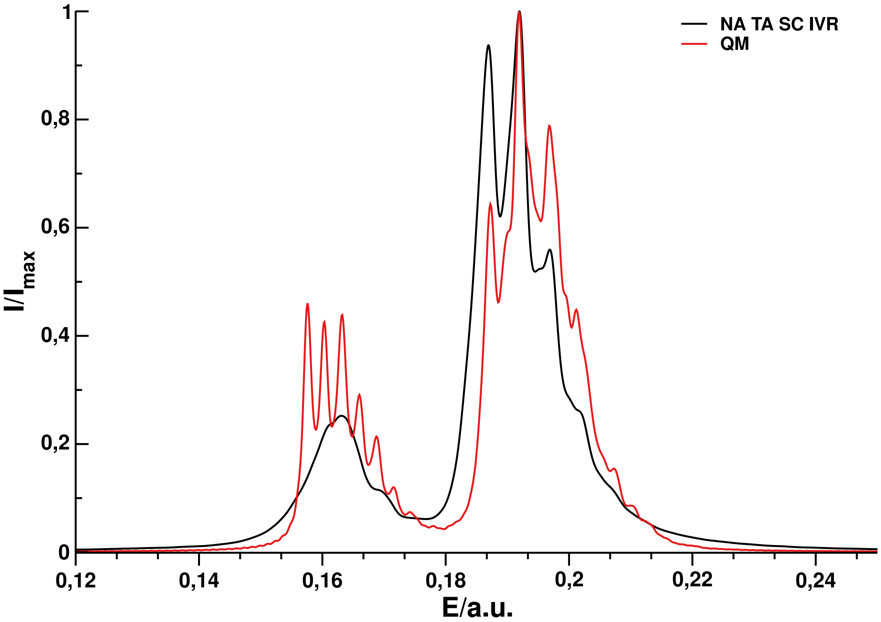

Fig. 6.5 Comparison of the semiclassical spectrum (black solid line) with the numerically exact one (red solid line) obtained with a 4D implementation of the split-operator method for the four mode of pyrazine.

with again an anomalous broadening which shall be investigated in future works. Where instead it is found a higher degree of disagreement, is the overall vibronic resolution which in the semiclassical spectrum seems to miss some features in the S_2 band and all of them in the S_1 one. Similarly to one of the previous study cases, the relative intensities of the features near the higher intensity peak is inverted with respect to the QM spectrum, such behavior could be observed due to the incorrect account of the populations and coherences in the long time limit. Moreover, it was also observed for this model, that the MMST trajectories tend to end multiple times in each trajectory in regions of negative population. While this is a known problem in the case of mapping Hamiltonians, it is possible to think that this could be one of the causes of some of the disagreements we observe between the semiclassical results and exact ones.

It is possible to conclude this subsection by observing that even though such system was already extensively studied by means of MCTDH methods [178] and semiclassical IVR by cellularization of the surviving amplitude [199, 173] obtaining very accurate results, the present approach is computationally less intensive since does not require the evaluation of the wavefunction on a discrete grid and is able to reach converge with a relatively low number of trajectories.

6.4 Conclusions

In this chapter a semiclassical time averaged approach to compute absorption spectra of nonadiabatic systems was tested. In particular, by starting from the full formula of the absorption spectrum, by applying the low temperature limit and the FC approximation it was possible to arrive to a working formula composed by a lineshape factor and a density of states factor. The latter is defined as the Fourier transform of the survival amplitude between the wavepacket at $t = 0$ and its time-evolved under the diabatic Hamiltonian. By introducing the mapping Hamiltonian, it became possible to rewrite semiclassically the density of states making possible the computation of absorption spectra by means of SC IVR methods.

By means of some numerical applications for the presented method on four model systems of different difficulty. Each semiclassical result was directly compared with numerically exact quantum mechanical results obtained by propagating the time-dependent wavefunction with the split-operator technique. Regarding this comparison, it was found a satisfactory agreement in reproducing the most important features of each system. Though, the lack of fine details makes the semiclassical approach to vibronic spectroscopy still in needs of some improvements.

In conclusion, the author believes that the presented nonadiabatic time-averaged semiclassical initial value representation has still room for improvements and at the moment efforts are being put in improving both the calculation protocols and fixing some of the issues that we observe. Said that, by previous experience with semiclassical methods, it is known that once the methodology is well assessed and fully consolidated it will also be possible to increase the efficiency and open the way for full atomistic simulations which can be used for understanding complex molecular processes beyond the Born-Oppenheimer approximations.

CHAPTER 7

CONCLUSIONS AND PERSPECTIVES

At the beginning of this manuscript, during the introduction a brief part of the discussion was centered on how quantum dynamics and classical dynamics are compatible. By means of few arguments it was possible to state that to some degree there is always a certain compatibility between the two. Moreover, as shown in chapter 2 in a more extensive way, it was clearly demonstrated that trajectory-based approaches as the SC IVR are able to return quantum-mechanical observables by including also quantum effects.

The content of the manuscript is focused on applications of semiclassical molecular dynamics to vibrational and vibronic spectroscopy. In particular, regarding vibrational spectroscopy, the corroborated capability of the SCIVR method to reproduce nuclear quantum effects was in first instance used in chapter 3 to shed some light on a debated question regarding what is classifiable as classical anharmonicity and what as a quantum feature. The main conclusion that one can draw from this discussion is that before deeming a result as due to a "quantum effect" direct comparison with legit and reliable classical approaches should be considered. Moreover, instead of considering study cases in which NQEs are known to be neglectable or more marginal, one should consider systems where the difference between classical and quantum approaches is radical. Another interesting debate which is still active and widely discussed regards the importance of NQEs in high dimensional molecular systems and the possibility to observe them with approximated quantum-dynamical approaches. For this reason, some of the most relevant developments of the semiclassical methodology reported in section 2.3.1 are aimed to improve its applicability on higher dimensional molecular and supramolecular systems.

In chapter 4 both quasiclassical MD and semiclassical MD are used to study the effects of solvation on complex molecular systems. In this chapter is particularly emphasized how the employed trajectories are useful not only as means to compute the spectrum, but also as an analysis tool to understand the complex network of interactions occurring between the different part of the atomistic systems and their role. Another aspect that is particularly evident from the results displayed in chapter 4, even if is not the main focus of it, regards the fact that in order to simulate such complex systems is necessary to employ an empirical force field. Such description of the molecular potential energy surface is often employed in the field of molecular modeling of biological systems, though the employment for the purpose of simulating vibrational spectra was found to be often inadequate especially when it comes to considering the quantitative agreement with respect to experimental results. The main conclusion that is possible to draw from the latter chapter is that the while tailored computational protocols and approximations can be used to compute semiclassical spectra of large molecular systems, the lack of accurate potentials poses a limit to the amount of information and their reliability.

Chapter 5 poses a question similar to the one of the previous chapter, and set the objective to explain with atomistic details a peculiar experimentally observed phenomenon. The main difference, lies in the fact that for this chapter hybrid QM/MM approaches are used to improve the aforementioned lack of reliable information and accuracy. In particular, during this chapter it can be appreciated how critical can be a good description of the interactions between the main system and the surrounding solvent molecules. Thanks to the latter, it was possible to observe that even if not as widely regarded, dispersion and polarization effects tend to be of crucial importance in reproducing the correct physical picture of the solvated system. Moreover, the use of the semiclassical approach for this problem provided a spectrum not only very accurate but also complemented of NQEs.

To conclude the overall discussion of these last two chapters. At the current status of the work and given all the results displayed in both chapter 4 and 5, it is not fully possible to claim that the inclusion of NQEs in the studied systems is fundamental for their description. And in general, as largely discussed in chapter 3, there are no solid bases to claim that NQEs are indeed observed. Though at the same time, two interesting cases from these chapters should be brought to attention in order the highlight the advantages obtained by employing the SC IVR with respect to a classical one. In particular, in the first two subsections of the results of chapter 4 was shown how a single trajectory QCT approach was not able to fully distinguish the spectroscopic features of the asymmetric and symmetric stretch C2'H_2, which has led us to opt for a multiple trajectory approach. On the other hand, in the last subsection of results, it was possible to observe that such distinction can be made when employing the DC SCIVR method by means of a single trajectory. Instead, in the discussion section of chapter 5, an important part of the argument is centered on the importance of the contribution given by quantum effects such as delocalization to the total energetics of the system. As a conclusion of such arguments it was found out that even if not of radical importance, delocalization tend to give a non-negligible contribution to the water-thymidine interaction. To obtain such result a mono dimensional model was used to obtain that estimate, though it was found to be reliable since the employed trajectory for the SCIVR calculation keeps in account of the vibrational ZPE and build Gaussian wavepackets on top of that. Which means that quantum delocalization and large amplitude motion are to some degree accounted for.

A minor part of the manuscript was also used to extend the treatise over the limits imposed by the Born-Oppenheimer approximation. Therefore section 2.5 of chapter 2 was used to formalize a semiclassical method able to account for nonadiabatic effects in vibronic spectroscopies. To this end, we employed the mapped Hamiltonian in order to map the problem of propagating the time-dependent wave function under the diabatic propagator into propagating classical trajectories. The presented results in chapter 6, showed that in general a semiclassical approach is able to correctly reproduce exact results for model systems. Though, some key aspects such as relative intensities and the overall vibronic resolution are still in need of improvement. The main advantage that comes with the employment of the NA TA SCIVR with respect to other methods is that does not rely on a stochastic method to emulate the branching of the wavepacket and does not require the direct evaluation of the wavefunction on a discrete grid. Also, when compared to other attempt to use SC IVR methods for the same purpose, convergence in this case is reached with a lower number of Monte Carlo samples and without the need of using ad-hoc fine-tuning parameters. Finally, one last aspect that is not properly new but was improved from previous work on the subject, regards the symplectic propagation of the trajectories and monodromy matrix elements which thanks to new working formulae returned more accurate results.

As a future perspective, it seems logical to think that with the growing efficiency of the electronic structure software, employment of accurate QM/MM potentials will become more and more advantageous for the computation of semiclassical vibrational spectra. By following this way, applications to high dimensional molecular systems wont require anymore to compromise the accuracy of the final results. Moreover, such tools could also help to further inquire about the presence and importance of NQEs in high dimensional systems. Always regarding this topic, a newly developed approach to semiclassical IR spectroscopy showed to be promising in reproducing both exact and experimental data for different systems. As further developments will follow it will be interesting to observe how the dimensionality related issues are handled. What is instead still missing and could lead to a real breakthrough in the field of semiclassical spectroscopy, is the development of a semiclassical approach to Raman spectroscopy. Such technique is widely applicable to water solution systems and samples of high biological/chemical importance, therefore could be of fundamental importance for the assessment of the SCIVR in the field of applied quantum dynamics. Talking about a less explored ground for semiclassical dynamics, it is now widely debated if NQEs plays an important role in systems placed in nano cavities.[342–344, 148, 345] For this reason we believe that a possible further field of application in which semiclassical dynamics can be a helpful tool to shed some light on, is polaritonic chemistry or in general systems under vibrational strong coupling.

REFERENCES

[1] A. Einstein, "On the motion of small particles suspended in liquids at rest required by the molecular-kinetic theory of heat," *Annalen der physik*, vol. 17, no. 549-560, p. 208, 1905.

[2] J. A. McCammon, B. R. Gelin, and M. Karplus, "Dynamics of folded proteins," *nature*, vol. 267, no. 5612, pp. 585–590, 1977.

[3] A. D. MacKerell Jr, D. Bashford, M. Bellott, R. L. Dunbrack Jr, J. D. Evanseck, M. J. Field, S. Fischer, J. Gao, H. Guo, S. Ha, *et al.*, "All-atom empirical potential for molecular modeling and dynamics studies of proteins," *The journal of physical chemistry B*, vol. 102, no. 18, pp. 3586–3616, 1998.

[4] D. Chandler, "Interfaces and the driving force of hydrophobic assembly," *Nature*, vol. 437, p. 640–647, Sept. 2005.

[5] P. G. Bolhuis, D. Chandler, C. Dellago, and P. L. Geissler, "Transition path sampling: Throwing ropes over rough mountain passes, in the dark," *Annual Review of Physical Chemistry*, vol. 53, p. 291–318, Oct. 2002.

[6] P. Pechukas, "Transition state theory," *Annual Review of Physical Chemistry*, vol. 32, p. 159–177, Oct. 1981.

[7] W. H. Thompson and W. H. Miller, "State-specific reaction probabilities from a dvr-abc green function," *Chemical Physics Letters*, vol. 206, p. 123–129, Apr. 1993.

[8] E. Wigner, "The transition state method," *Transactions of the Faraday Society*, vol. 34, p. 29, 1938.

[9] A. Rahman, "Correlations in the motion of atoms in liquid argon," *Physical Review*, vol. 136, p. A405–A411, Oct. 1964.

[10] R. Car and M. Parrinello, “Unified approach for molecular dynamics and density-functional theory,” *Physical Review Letters*, vol. 55, p. 2471–2474, Nov. 1985.

[11] M. Karplus and G. A. Petsko, “Molecular dynamics simulations in biology,” *Nature*, vol. 347, p. 631–639, Oct. 1990.

[12] M. E. Tuckerman, “Ab initiomolecular dynamics: basic concepts, current trends and novel applications,” *Journal of Physics: Condensed Matter*, vol. 14, p. R1297–R1355, Dec. 2002.

[13] D. Marx and J. Hutter, *Ab Initio Molecular Dynamics: Basic Theory and Advanced Methods*. Cambridge University Press, Apr. 2009.

[14] M. Ceriotti, W. Fang, P. G. Kusalik, R. H. McKenzie, A. Michaelides, M. A. Morales, and T. E. Markland, “Nuclear quantum effects in water and aqueous systems: Experiment, theory, and current challenges,” *Chem. Rev.*, vol. 116, pp. 7529–7550, July 2016.

[15] T. E. Markland and M. Ceriotti, “Nuclear quantum effects enter the mainstream,” *Nat. Rev. Chem.*, vol. 2, p. 0109, Feb. 2018.

[16] G. Mandelli, C. Aieta, and M. Ceotto, “Heavy atom tunneling in organic reactions at coupled cluster potential accuracy with a parallel implementation of anharmonic constant calculations and semiclassical transition state theory,” *J. Chem. Theory Comput.*, vol. 18, pp. 623–637, Feb. 2022.

[17] F. Angiolari, G. Mandelli, S. Huppert, C. Aieta, and R. Spezia, “Elucidating heavy atom tunneling kinetics in the cope rearrangement of semibullvalene,” *Chemistry*, p. e202401000, June 2024.

[18] C. Qu, Q. Yu, P. L. Houston, R. Conte, A. Nandi, and J. M. Bowman, “Interfacing q-AQUA with a polarizable force field: The best of both worlds,” *J. Chem. Theory Comput.*, vol. 19, pp. 3446–3459, June 2023.

[19] D. Marx, M. E. Tuckerman, J. Hutter, and M. Parrinello, “The nature of the hydrated excess proton in water,” *Nature*, vol. 397, pp. 601–604, Feb. 1999.

[20] M. E. Tuckerman, D. Marx, M. L. Klein, and M. Parrinello, “On the quantum nature of the shared proton in hydrogen bonds,” *Science*, vol. 275, pp. 817–820, Feb. 1997.

[21] D. Bohm, “A suggested interpretation of the quantum theory in terms of “hidden” variables. i,” *Physical Review*, vol. 85, p. 166–179, Jan. 1952.

[22] R. P. Feynman, A. R. Hibbs, and D. F. Styer, *Quantum mechanics and path integrals*. Courier Corporation, 2010.

[23] Y. Goldfarb, I. Degani, and D. J. Tannor, “Bohmian mechanics with complex action: a new trajectory-based formulation of quantum mechanics,” *J. Chem. Phys.*, vol. 125, p. 231103, Dec. 2006.

[24] Y. Goldfarb and D. J. Tannor, “Interference in bohmian mechanics with complex action,” *J. Chem. Phys.*, vol. 127, p. 161101, Oct. 2007.

[25] Y. Goldfarb, J. Schiff, and D. J. Tannor, “Unified derivation of bohmian methods and the incorporation of interference effects,” *J. Phys. Chem. A*, vol. 111, pp. 10416–10421, Oct. 2007.

[26] B. Poirier and D. Tannor, “An action principle for complex quantum trajectories,” *Mol. Phys.*, vol. 110, pp. 897–908, May 2012.

[27] N. Zamstein and D. J. Tannor, “Non-adiabatic molecular dynamics with complex quantum trajectories. i. the diabatic representation,” *J. Chem. Phys.*, vol. 137, p. 22A517, Dec. 2012.

[28] B. F. E. Curchod, I. Tavernelli, and U. Rothlisberger, “Trajectory-based solution of the nonadiabatic quantum dynamics equations: an on-the-fly approach for molecular dynamics simulations,” *Phys. Chem. Chem. Phys.*, vol. 13, pp. 3231–3236, Feb. 2011.

[29] B. F. E. Curchod and I. Tavernelli, “On trajectory-based nonadiabatic dynamics: Bohmian dynamics versus trajectory surface hopping,” *J. Chem. Phys.*, vol. 138, p. 184112, May 2013.

[30] B. F. E. Curchod, U. Rothlisberger, and I. Tavernelli, “Trajectory-based nonadiabatic dynamics with time-dependent density functional theory,” *ChemPhysChem*, vol. 14, p. 1314–1340, Apr. 2013.

[31] B. J. Berne and D. Thirumalai, “On the simulation of quantum systems: Path integral methods,” *Annual Review of Physical Chemistry*, vol. 37, p. 401–424, Oct. 1986.

[32] J. Cao and G. A. Voth, “The formulation of quantum statistical mechanics based on the feynman path centroid density. i. equilibrium properties,” *The Journal of Chemical Physics*, vol. 100, p. 5093–5105, Apr. 1994.

[33] J. Cao and G. A. Voth, “The formulation of quantum statistical mechanics based on the feynman path centroid density. ii. dynamical properties,” *The Journal of Chemical Physics*, vol. 100, p. 5106–5117, Apr. 1994.

[34] J. Cao and G. A. Voth, “The formulation of quantum statistical mechanics based on the feynman path centroid density. iii. phase space formalism and analysis of centroid molecular dynamics,” *The Journal of Chemical Physics*, vol. 101, p. 6157–6167, Oct. 1994.

[35] J. Cao and G. A. Voth, “The formulation of quantum statistical mechanics based on the feynman path centroid density. iv. algorithms for centroid molecular dynamics,” *The Journal of Chemical Physics*, vol. 101, p. 6168–6183, Oct. 1994.

[36] J. Cao and G. A. Voth, “The formulation of quantum statistical mechanics based on the feynman path centroid density. v. quantum instantaneous normal mode theory of liquids,” *The Journal of Chemical Physics*, vol. 101, p. 6184–6192, Oct. 1994.

[37] I. R. Craig and D. E. Manolopoulos, “Quantum statistics and classical mechanics: Real time correlation functions from ring polymer molecular dynamics,” *The Journal of Chemical Physics*, vol. 121, p. 3368–3373, Aug. 2004.

[38] M. Rossi, M. Ceriotti, and D. E. Manolopoulos, “How to remove the spurious resonances from ring polymer molecular dynamics,” *The Journal of Chemical Physics*, vol. 140, June 2014.

[39] R. Conte and E. Pollak, “Comparison between different gaussian series representations of the imaginary time propagator,” *Physical Review E*, vol. 81, Mar. 2010.

[40] R. Conte and E. Pollak, “Continuum limit frozen gaussian approximation for the reduced thermal density matrix of dissipative systems,” *The Journal of Chemical Physics*, vol. 136, Mar. 2012.

[41] M. Bonfanti, J. Petersen, P. Eisenbrandt, I. Burghardt, and E. Pollak, “Computation of the s1 $\leftarrow$ s0 vibronic absorption spectrum of formaldehyde by variational gaussian wavepacket and semiclassical ivr methods,” *Journal of Chemical Theory and Computation*, vol. 14, p. 5310–5323, Aug. 2018.

[42] A. Rognoni, R. Conte, and M. Ceotto, “How many water molecules are needed to solvate one?,” *Chem. Sci.*, vol. 12, pp. 2060–2064, Dec. 2020.

[43] F. Gabas, G. Di Liberto, R. Conte, and M. Ceotto, “Protonated glycine supramolecular systems: the need for quantum dynamics,” *Chem. Sci.*, vol. 9, pp. 7894–7901, Nov. 2018.

[44] J. H. Van Vleck, “The correspondence principle in the statistical interpretation of quantum mechanics,” *Proceedings of the National Academy of Sciences*, vol. 14, p. 178–188, Feb. 1928.

[45] K. G. Kay, “Semiclassical propagation for multidimensional systems by an initial value method,” *The Journal of Chemical Physics*, vol. 101, p. 2250–2260, Aug. 1994.

[46] K. G. Kay, “Semiclassical initial value treatments of atoms and molecules,” *Annual Review of Physical Chemistry*, vol. 56, p. 255–280, May 2005.

[47] T. Yamamoto and W. H. Miller, “Semiclassical calculation of thermal rate constants in full cartesian space: The benchmark reaction d+h2$\rightarrow$dh+h,” *The Journal of Chemical Physics*, vol. 118, p. 2135–2152, Feb. 2003.

[48] L. Bonnet, “Semiclassical initial value representation: From møller to miller,” *The Journal of Chemical Physics*, vol. 153, Nov. 2020.

[49] L. Bonnet, “Semiclassical initial value representation: From møller to miller. ii,” *The Journal of Chemical Physics*, vol. 158, Mar. 2023.

[50] D. Huber and E. J. Heller, “Generalized gaussian wave packet dynamics,” *The Journal of Chemical Physics*, vol. 87, p. 5302–5311, Nov. 1987.

[51] T. Begušić and J. Vaníček, “On-the-fly ab initio semiclassical evaluation of vibronic spectra at finite temperature,” *The Journal of Chemical Physics*, vol. 153, July 2020.

[52] E. Kletnieks, Y. C. Alonso, and J. J. L. Vanicek, “Isotope effects on the electronic spectra of ammonia from ab initio semiclassical dynamics,” *The Journal of Physical Chemistry A*, vol. 127, p. 8117–8125, Sept. 2023.

[53] M. S. Church, T. J. H. Hele, G. S. Ezra, and N. Ananth, “Nonadiabatic semiclassical dynamics in the mixed quantum-classical initial value representation,” *The Journal of Chemical Physics*, vol. 148, Dec. 2017.

[54] S. Malpathak, M. S. Church, and N. Ananth, “A semiclassical framework for mixed quantum classical dynamics,” *The Journal of Physical Chemistry A*, vol. 126, p. 6359–6375, Sept. 2022.

[55] K. G. Kay, “The herman–kluk approximation: Derivation and semiclassical corrections,” *Chemical Physics*, vol. 322, p. 3–12, Mar. 2006.

[56] F. Grossmann, “A semiclassical hybrid approach to many particle quantum dynamics,” *The Journal of Chemical Physics*, vol. 125, July 2006.

[57] M. Buchholz, F. Grossmann, and M. Ceotto, “Mixed semiclassical initial value representation time-averaging propagator for spectroscopic calculations,” *The Journal of Chemical Physics*, vol. 144, Mar. 2016.

[58] W. Koch, F. Großmann, J. T. Stockburger, and J. Ankerhold, “Non-markovian dissipative semiclassical dynamics,” *Physical Review Letters*, vol. 100, June 2008.

[59] M. Buchholz, F. Grossmann, and M. Ceotto, “Simplified approach to the mixed time-averaging semiclassical initial value representation for the calculation of dense vibrational spectra,” *The Journal of Chemical Physics*, vol. 148, Mar. 2018.

[60] F. Grossmann, “A semiclassical hybrid approach to linear response functions for infrared spectroscopy,” *Physica Scripta*, vol. 91, p. 044004, Mar. 2016.

[61] M. F. Herman and E. Kluk, “A semiclasical justification for the use of non-spreading wavepackets in dynamics calculations,” *Chemical Physics*, vol. 91, p. 27–34, Nov. 1984.

[62] W. H. Miller, “The semiclassical initial value representation: A potentially practical way for adding quantum effects to classical molecular dynamics simulations,” *The Journal of Physical Chemistry A*, vol. 105, p. 2942–2955, Mar. 2001.

[63] C. Lanzi, C. Aieta, M. Ceotto, and R. Conte, “A time averaged semiclassical approach to IR spectroscopy,” *J. Chem. Phys.*, vol. 160, June 2024.

[64] R. Conte and M. Ceotto, “Semiclassical molecular dynamics for spectroscopic calculations,” Nov. 2020.

[65] K. G. Kay, “Integral expressions for the semiclassical time-dependent propagator,” *J. Chem. Phys.*, vol. 100, pp. 4377–4392, Mar. 1994.

[66] K. G. Kay, “Numerical study of semiclassical initial value methods for dynamics,” *J. Chem. Phys.*, vol. 100, pp. 4432–4445, Mar. 1994.

[67] M. Baranger, M. A. M. d. Aguiar, F. Keck, H. J. Korsch, and B. Schellhaaß, “Semiclassical approximations in phase space with coherent states,” *J. Phys. A Math. Gen.*, vol. 34, pp. 7227–7286, Sept. 2001.

[68] A. L. Kaledin and W. H. Miller, “Time averaging the semiclassical initial value representation for the calculation of vibrational energy levels,” *J. Chem. Phys.*, vol. 118, pp. 7174–7182, Apr. 2003.

[69] A. L. Kaledin and W. H. Miller, “Time averaging the semiclassical initial value representation for the calculation of vibrational energy levels. ii. application to h2co, nh3, ch4, ch2d2,” *J. Chem. Phys.*, vol. 119, pp. 3078–3084, Aug. 2003.

[70] M. Ceotto, D. Dell’Angelo, and G. F. Tantardini, “Multiple coherent states semiclassical initial value representation spectra calculations of lateral interactions for CO on cu(100),” *J. Chem. Phys.*, vol. 133, p. 054701, Aug. 2010.

[71] R. Conte, A. Aspuru-Guzik, and M. Ceotto, “Reproducing deep tunneling splittings, resonances, and quantum frequencies in vibrational spectra from a handful of direct ab initio semiclassical trajectories,” *J. Phys. Chem. Lett.*, vol. 4, pp. 3407–3412, Oct. 2013.

[72] M. Ceotto, G. Di Liberto, and R. Conte, “Semiclassical “divide-and-conquer” method for spectroscopic calculations of high dimensional molecular systems,” *Phys. Rev. Lett.*, vol. 119, July 2017.

[73] G. Di Liberto, R. Conte, and M. Ceotto, ““divide and conquer” semiclassical molecular dynamics: A practical method for spectroscopic calculations of high dimensional molecular systems,” *J. Chem. Phys.*, vol. 148, p. 014307, Jan. 2018.

[74] R. Conte, F. Gabas, G. Botti, Y. Zhuang, and M. Ceotto, “Semiclassical vibrational spectroscopy with hessian databases,” *J. Chem. Phys.*, vol. 150, p. 244118, June 2019.

[75] M. Gandolfi, A. Rognoni, C. Aieta, R. Conte, and M. Ceotto, “Machine learning for vibrational spectroscopy via divide-and-conquer semiclassical initial value representation molecular dynamics with application to n-methylacetamide,” *J. Chem. Phys.*, vol. 153, p. 204104, Nov. 2020.

[76] M. Gandolfi and M. Ceotto, “Unsupervised machine learning neural gas algorithm for accurate evaluations of the hessian matrix in molecular dynamics,” *J. Chem. Theory Comput.*, vol. 17, pp. 6733–6746, Nov. 2021.

[77] H. J. Worner, J. B. Bertrand, D. V. Kartashov, P. B. Corkum, and D. M. Villeneuve, “Following a chemical reaction using high-harmonic interferometry,” *Nature*, vol. 466, p. 604–607, July 2010.

[78] M.-C. Bellissent-Funel, A. Hassanali, M. Havenith, R. Henchman, P. Pohl, F. Sterpone, D. van der Spoel, Y. Xu, and A. E. Garcia, “Water determines the structure and dynamics of proteins,” *Chemical Reviews*, vol. 116, p. 7673–7697, May 2016.

[79] F. Madeja and M. Havenith, “High resolution spectroscopy of carboxylic acid in the gas phase: Observation of proton transfer in (dcooh)2,” *The Journal of Chemical Physics*, vol. 117, p. 7162–7168, Oct. 2002.

[80] J. O. Richardson, C. Pérez, S. Lobsiger, A. A. Reid, B. Temelso, G. C. Shields, Z. Kisiel, D. J. Wales, B. H. Pate, and S. C. Althorpe, “Concerted hydrogen-bond breaking by quantum tunneling in the water hexamer prism,” *Science*, vol. 351, p. 1310–1313, Mar. 2016.

[81] F. Krausz, “From femtochemistry to attophysics,” *Physics World*, vol. 14, p. 41–46, Sept. 2001.

[82] M. Gao, C. Lu, H. Jean-Ruel, L. C. Liu, A. Marx, K. Onda, S.-y. Koshihara, Y. Nakano, X. Shao, T. Hiramatsu, G. Saito, H. Yamochi, R. R. Cooney, G. Moriena, G. Sciaini, and R. J. D. Miller, “Mapping molecular motions leading to charge delocalization with ultrabright electrons,” *Nature*, vol. 496, p. 343–346, Apr. 2013.

[83] M. Eichberger, H. Schafer, M. Krumova, M. Beyer, J. Demsar, H. Berger, G. Moriena, G. Sciaini, and R. J. D. Miller, “Snapshots of cooperative atomic motions in the optical suppression of charge density waves,” *Nature*, vol. 468, p. 799–802, Nov. 2010.

[84] R. Conte, C. Aieta, G. Botti, M. Cazzaniga, M. Gandolfi, C. Lanzi, G. Mandelli, D. Moscato, and M. Ceotto, “Anharmonicity and quantum nuclear effects in theoretical vibrational spectroscopy: a molecular tale of two cities,” *Theor. Chem. Acc.*, vol. 142, May 2023.

[85] N. De Leon and E. J. Heller, “Semiclassical quantization and extraction of eigenfunctions using arbitrary trajectories,” *J. Chem. Phys.*, vol. 78, pp. 4005–4017, Mar. 1983.

[86] M. Ceotto, S. Atahan, G. F. Tantardini, and A. Aspuru-Guzik, “Multiple coherent states for first-principles semiclassical initial value representation molecular dynamics,” *J. Chem. Phys.*, vol. 130, p. 234113, June 2009.

[87] Z. Chen and Y. Yang, “Incorporating nuclear quantum effects in molecular dynamics with a constrained minimized energy surface,” *The Journal of Physical Chemistry Letters*, vol. 14, p. 279–286, Jan. 2023.

[88] J. C. Tully, “Molecular dynamics with electronic transitions,” *J. Chem. Phys.*, vol. 93, pp. 1061–1071, July 1990.

[89] T. J. Martinez, M. Ben-Nun, and R. D. Levine, “Multi-electronic-state molecular dynamics: A wave function approach with applications,” *J. Phys. Chem.*, vol. 100, pp. 7884–7895, Jan. 1996.

[90] W. Domcke, D. R. Yarkony, and H. Koppel, *Conical intersections: Electronic structure, dynamics & spectroscopy*. Advanced Series In Physical Chemistry, Singapore, Singapore: World Scientific Publishing, Apr. 2004.

[91] H. D. Meyer and W. H. Miller, “A classical analog for electronic degrees of freedom in nonadiabatic collision processes,” *J. Chem. Phys.*, vol. 70, pp. 3214–3223, Apr. 1979.

[92] G. Stock and M. Thoss, “Semiclassical description of nonadiabatic quantum dynamics,” *Phys. Rev. Lett.*, vol. 78, pp. 578–581, Jan. 1997.

[93] S. Kundu and N. Makri, “<scp>pathsum</scp>: A c++ and fortran suite of fully quantum mechanical real-time path integral methods for (multi-)system + bath dynamics,” *The Journal of Chemical Physics*, vol. 158, June 2023.

[94] S. C. Althorpe, “Path-integral approximations to quantum dynamics,” *The European Physical Journal B*, vol. 94, July 2021.

[95] S. C. Althorpe, “Path integral simulations of condensed-phase vibrational spectroscopy,” *Annual Review of Physical Chemistry*, vol. 75, p. 397–420, June 2024.

[96] J. O. Richardson and S. C. Althorpe, “Ring-polymer instanton method for calculating tunneling splittings,” *The Journal of Chemical Physics*, vol. 134, Feb. 2011.

[97] M. Topaler and N. Makri, “System-specific discrete variable representations for path integral calculations with quasi-adiabatic propagators,” *Chemical Physics Letters*, vol. 210, p. 448–457, July 1993.

[98] N. Makri and D. E. Makarov, “Tensor propagator for iterative quantum time evolution of reduced density matrices. i. theory,” *The Journal of Chemical Physics*, vol. 102, p. 4600–4610, Mar. 1995.

[99] N. Makri, “Numerical path integral techniques for long time dynamics of quantum dissipative systems,” *Journal of Mathematical Physics*, vol. 36, p. 2430–2457, May 1995.

[100] N. Makri, “Small matrix disentanglement of the path integral: Overcoming the exponential tensor scaling with memory length,” *The Journal of Chemical Physics*, vol. 152, Jan. 2020.

[101] G. A. Voth, “Path-integral centroid methods in quantum statistical mechanics and dynamics,” Jan. 1996.

[102] S. Habershon, D. E. Manolopoulos, T. E. Markland, and T. F. Miller, “Ring-polymer molecular dynamics: Quantum effects in chemical dynamics from classical trajectories in an extended phase space,” *Annual Review of Physical Chemistry*, vol. 64, p. 387–413, Apr. 2013.

[103] V. P. Maslov and M. V. Fedoriuk, *Semi-classical approximation in quantum mechanics*, vol. 7. Springer Science and Business Media, 2001.

[104] W. H. Miller, "Classical s matrix: Numerical application to inelastic collisions," *The Journal of Chemical Physics*, vol. 53, p. 3578–3587, Nov. 1970.

[105] E. J. Heller, "Frozen gaussians: A very simple semiclassical approximation," *The Journal of Chemical Physics*, vol. 75, p. 2923–2931, Sept. 1981.

[106] K. Miyazaki and N. Ananth, "Nonadiabatic simulations of photoisomerization and dissociation in ethylene using ab initio classical trajectories," *The Journal of Chemical Physics*, vol. 159, Sept. 2023.

[107] S. Malpathak and N. Ananth, "Semiclassical dynamics in Wigner phase space I: Adiabatic hybrid Wigner dynamics," *The Journal of Chemical Physics*, vol. 161, p. 094109, 09 2024.

[108] S. Malpathak and N. Ananth, "Semiclassical dynamics in Wigner phase space II: Nonadiabatic hybrid Wigner dynamics," *The Journal of Chemical Physics*, vol. 161, p. 094110, 09 2024.

[109] X. Sun, H. Wang, and W. H. Miller, "Semiclassical theory of electronically nonadiabatic dynamics: Results of a linearized approximation to the initial value representation," *The Journal of Chemical Physics*, vol. 109, p. 7064–7074, Nov. 1998.

[110] X. Sun, H. Wang, and W. H. Miller, "On the semiclassical description of quantum coherence in thermal rate constants," *The Journal of Chemical Physics*, vol. 109, p. 4190–4200, Sept. 1998.

[111] X. Sun and W. H. Miller, "Forward–backward initial value representation for semiclassical time correlation functions," *The Journal of Chemical Physics*, vol. 110, p. 6635–6644, Apr. 1999.

[112] R. Conte, C. Aieta, M. Cazzaniga, and M. Ceotto, "A perspective on the investigation of spectroscopy and kinetics of complex molecular systems with semiclassical approaches," *The Journal of Physical Chemistry Letters*, vol. 15, p. 7566–7576, July 2024.

[113] C. Aieta, M. Micciarelli, G. Bertaina, and M. Ceotto, "Anharmonic quantum nuclear densities from full dimensional vibrational eigenfunctions with application to protonated glycine," *Nature Communications*, vol. 11, Aug. 2020.

[114] C. Aieta, G. Bertaina, M. Micciarelli, and M. Ceotto, "Representing molecular ground and excited vibrational eigenstates with nuclear densities obtained from semiclassical initial value representation molecular dynamics," *The Journal of Chemical Physics*, vol. 153, Dec. 2020.

[115] S. Garashchuk and D. Tannor, "Wave packet correlation function approach to h2(v)+h→h+h2(v'): semiclassical implementation," *Chemical Physics Letters*, vol. 262, p. 477–485, Nov. 1996.

[116] D. J. Tannor and S. Garashchuk, “Semiclassical calculation of chemical reaction dynamics via wavepacket correlation functions,” *Annual Review of Physical Chemistry*, vol. 51, p. 553–600, Oct. 2000.

[117] M. Micciarelli, R. Conte, J. Suarez, and M. Ceotto, “Anharmonic vibrational eigenfunctions and infrared spectra from semiclassical molecular dynamics,” *The Journal of Chemical Physics*, vol. 149, Aug. 2018.

[118] M. Micciarelli, F. Gabas, R. Conte, and M. Ceotto, “An effective semiclassical approach to ir spectroscopy,” *The Journal of Chemical Physics*, vol. 150, May 2019.

[119] F. Kroninger, C. Lasser, and J. J. L. Vanicek, “Sampling strategies for the herman–kluk propagator of the wavefunction,” *Frontiers in Physics*, vol. 11, Mar. 2023.

[120] F. Kroninger, C. Lasser, and J. J. L. Vanicek, “Sampling strategies for expectation values within the herman–kluk approximation,” *arXiv preprint arXiv:2408.00130*, 2024.

[121] K. Husimi, “Some formal properties of the density matrix,” *Proceedings of the Physico-Mathematical Society of Japan. 3rd Series*, vol. 22, no. 4, pp. 264–314, 1940.

[122] N. Makri and W. H. Miller, “Monte carlo integration with oscillatory integrands: implications for feynman path integration in real time,” *Chemical Physics Letters*, vol. 139, p. 10–14, Aug. 1987.

[123] N. Makri, “Monte carlo evaluation of forward-backward semiclassical correlation functions with a quantized coherent state density,” *The Journal of Physical Chemistry B*, vol. 106, p. 8390–8398, July 2002.

[124] S. X. Sun and W. H. Miller, “Statistical sampling of semiclassical distributions: Calculating quantum mechanical effects using metropolis monte carlo,” *The Journal of Chemical Physics*, vol. 117, p. 5522–5528, Sept. 2002.

[125] G. Tao and W. H. Miller, “Time-dependent importance sampling in semiclassical initial value representation calculations for time correlation functions,” *The Journal of Chemical Physics*, vol. 135, July 2011.

[126] G. Tao and W. H. Miller, “Time-dependent importance sampling in semiclassical initial value representation calculations for time correlation functions. ii. a simplified implementation,” *The Journal of Chemical Physics*, vol. 137, Sept. 2012.

[127] H. Wang, D. E. Manolopoulos, and W. H. Miller, “Generalized filinov transformation of the semiclassical initial value representation,” *The Journal of Chemical Physics*, vol. 115, p. 6317–6326, Oct. 2001.

[128] M. Ceotto, G. F. Tantardini, and A. Aspuru-Guzik, “Fighting the curse of dimensionality in first-principles semiclassical calculations: Non-local reference states for large number of dimensions,” *The Journal of Chemical Physics*, vol. 135, Dec. 2011.

[129] F. Gabas, R. Conte, and M. Ceotto, “On-the-fly ab initio semiclassical calculation of glycine vibrational spectrum,” *Journal of Chemical Theory and Computation*, vol. 13, p. 2378–2388, May 2017.

[130] M. Cazzaniga, M. Micciarelli, F. Moriggi, A. Mahmoud, F. Gabas, and M. Ceotto, “Anharmonic calculations of vibrational spectra for molecular adsorbates: A divide-and-conquer semiclassical molecular dynamics approach,” *The Journal of Chemical Physics*, vol. 152, Mar. 2020.

[131] F. Gabas, R. Conte, and M. Ceotto, “Semiclassical vibrational spectroscopy of biological molecules using force fields,” *Journal of Chemical Theory and Computation*, vol. 16, p. 3476–3485, May 2020.

[132] A. Rognoni, R. Conte, and M. Ceotto, “Caldeira–leggett model vs ab initio potential: A vibrational spectroscopy test of water solvation,” *The Journal of Chemical Physics*, vol. 154, Mar. 2021.

[133] D. Moscato, G. Mandelli, M. Bondanza, F. Lipparini, R. Conte, B. Mennucci, and M. Ceotto, “Unraveling water solvation effects with quantum mechanics/molecular mechanics semiclassical vibrational spectroscopy: The case of thymidine,” *J. Am. Chem. Soc.*, vol. 146, pp. 8179–8188, Mar. 2024.

[134] D. Moscato, F. Gabas, R. Conte, and M. Ceotto, “Vibrational spectroscopy simulation of solvation effects on a g-quadruplex,” *J. Biomol. Struct. Dyn.*, vol. 41, pp. 14248–14258, Mar. 2023.

[135] J. M. DICKEY and A. PASKIN, “Computer simulation of the lattice dynamics of solids,” *Physical Review*, vol. 188, p. 1407–1418, Dec. 1969.

[136] M. E. Tuckerman, *Statistical mechanics: theory and molecular simulation*. Oxford university press, 2023.

[137] M. Buchholz, E. Fallacara, F. Gottwald, M. Ceotto, F. Grossmann, and S. D. Ivanov, “Herman-kluk propagator is free from zero-point energy leakage,” *Chemical Physics*, vol. 515, p. 231–235, Nov. 2018.

[138] J. M. Bowman, A. Kuppermann, and G. C. Schatz, “Quantum initial conditions in quasi-classical trajectory calculations,” *Chemical Physics Letters*, vol. 19, no. 1, p. 21–25, 1973.

[139] J. M. Bowman, B. Gazdy, and Q. Sun, “A method to constrain vibrational energy in quasiclassical trajectory calculations,” *The Journal of Chemical Physics*, vol. 91, p. 2859–2862, Sept. 1989.

[140] C. Qu and J. M. Bowman, “Revisiting adiabatic switching for initial conditions in quasi-classical trajectory calculations: Application to ch4,” *The Journal of Physical Chemistry A*, vol. 120, p. 4988–4993, Feb. 2016.

[141] L. Mino, M. Cazzaniga, F. Moriggi, and M. Ceotto, “Elucidating nox surface chemistry at the anatase (101) surface in tio2 nanoparticles,” *The Journal of Physical Chemistry C*, vol. 127, p. 437–449, Dec. 2022.

[142] D. Barbiero, G. Bertaina, M. Ceotto, and R. Conte, “Anharmonic assignment of the water octamer spectrum in the oh stretch region,” *The Journal of Physical Chemistry A*, vol. 127, p. 6213–6221, July 2023.

[143] T. L. Fischer, M. Bodecker, S. M. Schweer, J. Dupont, V. Lepère, A. Zehnacker-Rentien, M. A. Suhm, B. Schroder, T. Henkes, D. M. Andrada, R. M. Balabin, H. K. Singh, H. P. Bhattacharyya, M. Sarma, S. Kaser, K. Topfer, L. I. Vazquez-Salazar, E. D. Boittier, M. Meuwly, G. Mandelli, C. Lanzi, R. Conte, M. Ceotto, F. Dietrich, V. Cisternas, R. Gnanasekaran, M. Hippler, M. Jarraya, M. Hochlaf, N. Viswanathan, T. Nevolianis, G. Rath, W. A. Kopp, K. Leonhard, and R. A. Mata, “The first hydra challenge for computational vibrational spectroscopy,” *Physical Chemistry Chemical Physics*, vol. 25, no. 33, p. 22089–22102, 2023.

[144] T. J. Martinez, “Seaming is believing,” *Nature*, vol. 467, p. 412–413, Sept. 2010.

[145] F. Segatta, I. Gdor, J. Réhault, S. Taioli, N. Friedman, M. Sheves, I. Rivalta, S. Ruhman, G. Cerullo, and M. Garavelli, “Ultrafast carotenoid to retinal energy transfer in xanthorhodopsin revealed by the combination of transient absorption and two-dimensional electronic spectroscopy,” *Chemistry – A European Journal*, vol. 24, p. 12084–12092, Aug. 2018.

[146] N. H. List, C. M. Jones, and T. J. Martínez, “Internal conversion of the anionic gfp chromophore: in and out of the i-twisted s1/s0 conical intersection seam,” *Chemical Science*, vol. 13, no. 2, p. 373–385, 2022.

[147] N. H. List, C. M. Jones, and T. J. Martínez, “Chemical control of excited-state reactivity of the anionic green fluorescent protein chromophore,” *Communications Chemistry*, vol. 7, Feb. 2024.

[148] J. O. Richardson, “Nonadiabatic tunneling in chemical reactions,” *The Journal of Physical Chemistry Letters*, vol. 15, p. 7387–7397, July 2024.

[149] G. A. Worth and L. S. Cederbaum, “Beyond born-oppenheimer: Molecular dynamics through a conical intersection,” *Annual Review of Physical Chemistry*, vol. 55, p. 127–158, June 2004.

[150] J. E. Subotnik and N. Shenvi, “A new approach to decoherence and momentum rescaling in the surface hopping algorithm,” *The Journal of Chemical Physics*, vol. 134, Jan. 2011.

[151] C. Pieroni and F. Agostini, “Nonadiabatic dynamics with coupled trajectories,” *Journal of Chemical Theory and Computation*, vol. 17, p. 5969–5991, Sept. 2021.

[152] E. Runge and E. K. U. Gross, “Density-functional theory for time-dependent systems,” *Physical Review Letters*, vol. 52, p. 997–1000, Mar. 1984.

[153] B. O. Roos, *Multiconfigurational quantum chemistry*, p. 725–764. Elsevier, 2005.

[154] L. Gonzalez, D. Escudero, and L. Serrano-Andres, “Progress and challenges in the calculation of electronic excited states,” *ChemPhysChem*, vol. 13, p. 28–51, Sept. 2011.

[155] M. F. Herman, “A semiclassical surface hopping propagator for nonadiabatic problems,” *The Journal of Chemical Physics*, vol. 103, p. 8081–8097, Nov. 1995.

[156] X. He and J. Liu, “A new perspective for nonadiabatic dynamics with phase space mapping models,” *The Journal of Chemical Physics*, vol. 151, July 2019.

[157] B. Wu, X. He, and J. Liu, “Nonadiabatic field on quantum phase space: A century after ehrenfest,” *The Journal of Physical Chemistry Letters*, vol. 15, p. 644–658, Jan. 2024.

[158] X. He, X. Cheng, B. Wu, and J. Liu, “Nonadiabatic field with triangle window functions on quantum phase space,” *The Journal of Physical Chemistry Letters*, vol. 15, p. 5452–5466, May 2024.

[159] J. R. Mannouch and J. O. Richardson, “A partially linearized spin-mapping approach for nonadiabatic dynamics. ii. analysis and comparison with related approaches,” *The Journal of Chemical Physics*, vol. 153, Nov. 2020.

[160] U. Muller and G. Stock, “Flow of zero-point energy and exploration of phase space in classical simulations of quantum relaxation dynamics. ii. application to nonadiabatic processes,” *The Journal of Chemical Physics*, vol. 111, p. 77–88, July 1999.

[161] S. J. Cotton and W. H. Miller, “Symmetrical windowing for quantum states in quasi-classical trajectory simulations: Application to electronically non-adiabatic processes,” *The Journal of Chemical Physics*, vol. 139, Dec. 2013.

[162] M. Tao, “Explicit symplectic approximation of nonseparable hamiltonians: Algorithm and long time performance,” *Physical Review E*, vol. 94, Oct. 2016.

[163] S. Choi and J. Vaníček, “Efficient geometric integrators for nonadiabatic quantum dynamics. i. the adiabatic representation,” *The Journal of Chemical Physics*, vol. 150, May 2019.

[164] L. E. Cook, J. E. Runeson, J. O. Richardson, and T. J. H. Hele, “Which algorithm best propagates the meyer–miller–stock–thoss mapping hamiltonian for non-adiabatic dynamics?,” *Journal of Chemical Theory and Computation*, vol. 19, p. 6109–6125, Sept. 2023.

[165] J. O. Richardson, P. Meyer, M.-O. Pleinert, and M. Thoss, “An analysis of nonadiabatic ring-polymer molecular dynamics and its application to vibronic spectra,” *Chemical Physics*, vol. 482, p. 124–134, Jan. 2017.

[166] A. Kelly, R. van Zon, J. Schofield, and R. Kapral, “Mapping quantum-classical liouville equation: Projectors and trajectories,” *The Journal of Chemical Physics*, vol. 136, Feb. 2012.

[167] I. Yamazaki, T. Murao, T. Yamanaka, and K. Yoshihara, “Intramolecular electronic relaxation and photoisomerization processes in the isolated azabenzene molecules pyridine, pyrazine and pyrimidine,” *Faraday Discussions of the Chemical Society*, vol. 75, p. 395, 1983.

[168] T. J. Penfold, E. Gindensperger, C. Daniel, and C. M. Marian, “Spin-vibronic mechanism for intersystem crossing,” *Chemical Reviews*, vol. 118, p. 6975–7025, Mar. 2018.

[169] E. Haller, H. Koppel, and L. Cederbaum, “The visible absorption spectrum of no2: A three-mode nuclear dynamics investigation,” *Journal of Molecular Spectroscopy*, vol. 111, no. 2, pp. 377–397, 1985.

[170] S. Mahapatra, “Excited electronic states and nonadiabatic effects in contemporary chemical dynamics,” *Accounts of Chemical Research*, vol. 42, p. 1004–1015, May 2009.

[171] I. B. Bersuker, “Modern aspects of the jahn-teller effect theory and applications to molecular problems,” *Chemical Reviews*, vol. 101, p. 1067–1114, Mar. 2001.

[172] I. B. Bersuker, “Jahn-teller and pseudo-jahn–teller effects: From particular features to general tools in exploring molecular and solid state properties,” *Chemical Reviews*, vol. 121, p. 1463–1512, Dec. 2020.

[173] M. Thoss, W. H. Miller, and G. Stock, “Semiclassical description of nonadiabatic quantum dynamics: Application to the s1–s2 conical intersection in pyrazine,” *The Journal of Chemical Physics*, vol. 112, p. 10282–10292, June 2000.

[174] A. R. Walton and D. E. Manolopoulos, “A new semiclassical initial value method for franck-condon spectra,” *Molecular Physics*, vol. 87, p. 961–978, Mar. 1996.

[175] J. Janos, P. Slavicek, and B. F. Curchod, “Including photoexcitation explicitly in trajectory-based nonadiabatic dynamics at no cost,” *The Journal of Physical Chemistry Letters*, vol. 15, pp. 10614–10622, 2024.

[176] T. Begusic and J. Vanicek, “Finite-temperature, anharmonicity, and duschinsky effects on the two-dimensional electronic spectra from ab initio thermo-field gaussian wavepacket dynamics,” *The journal of physical chemistry letters*, vol. 12, no. 11, pp. 2997–3005, 2021.

[177] Z. T. Zhang and J. J. Vaníček, “Finite-temperature vibronic spectra from the split-operator coherence thermofield dynamics,” *The Journal of Chemical Physics*, vol. 160, no. 8, 2024.

[178] G. A. Worth, H.-D. Meyer, and L. Cederbaum, “The effect of a model environment on the s 2 absorption spectrum of pyrazine: A wave packet study treating all 24 vibrational modes,” *The Journal of chemical physics*, vol. 105, no. 11, pp. 4412–4426, 1996.

[179] G. A. Worth, H.-D. Meyer, H. Koppel, L. Cederbaum, and I. Burghardt, “Using the mctdh wavepacket propagation method to describe multimode non-adiabatic dynamics,” *International Reviews in Physical Chemistry*, vol. 27, no. 3, pp. 569–606, 2008.

[180] N. Ananth, C. Venkataraman, and W. H. Miller, “Semiclassical description of electronically nonadiabatic dynamics via the initial value representation,” *The Journal of chemical physics*, vol. 127, no. 8, 2007.

[181] D. T. Colbert and W. H. Miller, “A novel discrete variable representation for quantum mechanical reactive scattering via the s-matrix kohn method,” *The Journal of chemical physics*, vol. 96, no. 3, pp. 1982–1991, 1992.

[182] J. M. Bowman, S. Carter, and X. Huang, “Multimode: a code to calculate rovibrational energies of polyatomic molecules,” *International Reviews in Physical Chemistry*, vol. 22, no. 3, pp. 533–549, 2003.

[183] V. Barone, M. Biczysko, J. Bloino, M. Borkowska-Panek, I. Carnimeo, and P. Panek, “Toward anharmonic computations of vibrational spectra for large molecular systems,” *International Journal of Quantum Chemistry*, vol. 112, no. 9, pp. 2185–2200, 2012.

[184] H.-D. Meyer, U. Manthe, and L. S. Cederbaum, “The multi-configurational time-dependent hartree approach,” *Chemical Physics Letters*, vol. 165, no. 1, pp. 73–78, 1990.

[185] E. J. Heller, “The semiclassical way to molecular spectroscopy,” *Accounts of Chemical Research*, vol. 14, no. 12, pp. 368–375, 1981.

[186] D. V. Shalashilin and M. S. Child, “Multidimensional quantum propagation with the help of coupled coherent states,” *The Journal of Chemical Physics*, vol. 115, no. 12, pp. 5367–5375, 2001.

[187] E. Pollak and S. Miret-Artes, “Thawed semiclassical ivr propagators,” *Journal of Physics A: Mathematical and General*, vol. 37, no. 41, p. 9669, 2004.

[188] E. Zambrano, M. vsulc, and J. Vanicek, “Improving the accuracy and efficiency of time-resolved electronic spectra calculations: Cellular dephasing representation with a prefactor,” *The Journal of chemical physics*, vol. 139, no. 5, 2013.

[189] D.-h. Lu and W. L. Hase, “Classical mechanics of intramolecular vibrational energy flow in benzene. iv. models with reduced dimensionality,” *The Journal of chemical physics*, vol. 89, no. 11, pp. 6723–6735, 1988.

[190] W. H. Miller, W. L. Hase, and C. L. Darling, “A simple model for correcting the zero point energy problem in classical trajectory simulations of polyatomic molecules,” *The Journal of chemical physics*, vol. 91, no. 5, pp. 2863–2868, 1989.

[191] G. Czako, A. L. Kaledin, and J. M. Bowman, “A practical method to avoid zero-point leak in molecular dynamics calculations: Application to the water dimer,” *The Journal of chemical physics*, vol. 132, no. 16, 2010.

[192] M. Cazzaniga, M. Micciarelli, F. Gabas, F. Finocchi, and M. Ceotto, "Quantum anharmonic calculations of vibrational spectra for water adsorbed on titania anatase (101) surface: dissociative versus molecular adsorption," *The Journal of Physical Chemistry C*, vol. 126, no. 29, pp. 12060–12073, 2022.

[193] T. Carrington Jr and W. H. Miller, "Reaction surface description of intramolecular hydrogen atom transfer in malonaldehyde," *The Journal of chemical physics*, vol. 84, no. 8, pp. 4364–4370, 1986.

[194] M. Wehrle, S. Oberli, and J. Vanicek, "On-the-fly ab initio semiclassical dynamics of floppy molecules: Absorption and photoelectron spectra of ammonia," *The Journal of Physical Chemistry A*, vol. 119, no. 22, pp. 5685–5690, 2015.

[195] C. Qu, R. Conte, P. L. Houston, and J. M. Bowman, "Full-dimensional potential energy surface for acetylacetone and tunneling splittings," *Physical Chemistry Chemical Physics*, vol. 23, no. 13, pp. 7758–7767, 2021.

[196] G. Bussi, D. Donadio, and M. Parrinello, "Canonical sampling through velocity rescaling," *The Journal of chemical physics*, vol. 126, no. 1, 2007.

[197] D. R. Galimberti, A. Milani, M. Tommasini, C. Castiglioni, and M.-P. Gaigeot, "Combining static and dynamical approaches for infrared spectra calculations of gas phase molecules and clusters," *Journal of chemical theory and computation*, vol. 13, no. 8, pp. 3802–3813, 2017.

[198] L. Bonnet and J. Rayez, "Quasiclassical trajectory method for molecular scattering processes: necessity of a weighted binning approach," *Chemical physics letters*, vol. 277, no. 1-3, pp. 183–190, 1997.

[199] M. L. Brewer, J. S. Hulme, and D. E. Manolopoulos, "Semiclassical dynamics in up to 15 coupled vibrational degrees of freedom," *The Journal of chemical physics*, vol. 106, no. 12, pp. 4832–4839, 1997.

[200] R. T. Skodje, F. Borondo, and W. P. Reinhardt, "The semiclassical quantization of nonseparable systems using the method of adiabatic switching," *The Journal of chemical physics*, vol. 82, no. 10, pp. 4611–4632, 1985.

[201] B. Johnson, "Semiclassical vibrational eigenvalues of h+ 3, d+ 3, and t+ 3 by the adiabatic switching method," *The Journal of chemical physics*, vol. 86, no. 3, pp. 1445–1450, 1987.

[202] Q. Sun, J. M. Bowman, and B. Gazdy, "Application of adiabatic switching to vibrational energies of three-dimensional hco, h2o, and h2co," *The Journal of chemical physics*, vol. 89, no. 5, pp. 3124–3130, 1988.

[203] S. Saini, J. Zakrzewski, and H. S. Taylor, "Semiclassical quantization via adiabatic switching. ii. choice of tori and initial conditions for multidimensional systems," *Physical Review A*, vol. 38, no. 8, p. 3900, 1988.

[204] A. Bose and N. Makri, "Wigner phase space distribution via classical adiabatic switching," *The Journal of Chemical Physics*, vol. 143, no. 11, 2015.

[205] C. Qu and J. M. Bowman, “Revisiting adiabatic switching for initial conditions in quasi-classical trajectory calculations: application to ch4,” *The Journal of Physical Chemistry A*, vol. 120, no. 27, pp. 4988–4993, 2016.

[206] T. Nagy and G. Lendvay, “Adiabatic switching extended to prepare semiclassically quantized rotational–vibrational initial states for quasiclassical trajectory calculations,” *The Journal of Physical Chemistry Letters*, vol. 8, no. 18, pp. 4621–4626, 2017.

[207] R. Conte, L. Parma, C. Aieta, A. Rognoni, and M. Ceotto, “Improved semiclassical dynamics through adiabatic switching trajectory sampling,” *The Journal of Chemical Physics*, vol. 151, no. 21, 2019.

[208] G. Botti, M. Ceotto, and R. Conte, “On-the-fly adiabatically switched semiclassical initial value representation molecular dynamics for vibrational spectroscopy of biomolecules,” *The Journal of Chemical Physics*, vol. 155, no. 23, 2021.

[209] G. Botti, C. Aieta, and R. Conte, “The complex vibrational spectrum of proline explained through the adiabatically switched semiclassical initial value representation,” *The Journal of Chemical Physics*, vol. 156, no. 16, 2022.

[210] L. D. Landau and E. M. Lifshitz, *Quantum mechanics: non-relativistic theory*, vol. 3. Elsevier, 2013.

[211] J. Martin, T. Lee, and P. Taylor, “An accurate ab initio quartic force field for formaldehyde and its isotopomers,” *Journal of Molecular Spectroscopy*, vol. 160, p. 105–116, July 1993.

[212] S. Carter, N. Pinnavaia, and N. C. Handy, “The vibrations of formaldehyde,” *Chemical Physics Letters*, vol. 240, p. 400–408, July 1995.

[213] K. Hoogsteen, “The crystal and molecular structure of a hydrogen-bonded complex between 1-methylthymine and 9-methyladenine,” *Acta Crystallographica*, vol. 16, pp. 907–916, Sep 1963.

[214] R. E. A. Kelly, Y. J. Lee, and L. N. Kantorovich, “Homopairing possibilities of the dna bases cytosine and guanine: An ab initio dft study,” *The Journal of Physical Chemistry B*, vol. 109, p. 22045–22052, Oct. 2005.

[215] J. Sponer, A. Mladek, N. Spackova, X. Cang, T. E. Cheatham, and S. Grimme, “Relative stability of different dna guanine quadruplex stem topologies derived using large-scale quantum-chemical computations,” *Journal of the American Chemical Society*, vol. 135, p. 9785–9796, June 2013.

[216] T. Sieranski, “Energy, orbital and structural stacking landscape of a purine homodimer system,” *Theoretical Chemistry Accounts*, vol. 139, Sept. 2020.

[217] H. J. Lipps and D. Rhodes, “G-quadruplex structures: in vivo evidence and function,” *Trends in Cell Biology*, vol. 19, pp. 414–422, Aug. 2009.

[218] D. Rhodes and H. J. Lipps, "G-quadruplexes and their regulatory roles in biology," *Nucleic acids research*, vol. 43, pp. 8627–8637, Oct. 2015.

[219] W. M. Guiblet, M. DeGiorgio, X. Cheng, F. Chiaromonte, K. A. Eckert, Y.-F. Huang, and K. D. Makova, "Selection and thermostability suggest g-quadruplexes are novel functional elements of the human genome," *Genome Research*, vol. 31, pp. 1136–1149, July 2021.

[220] S.-J. Adam, L. Grand Cory, J. Bearss David, and H. Hurley Laurence, "Direct evidence for a g-quadruplex in a promoter region and its targeting with a small molecule to repress c-myc transcription," *Proceedings of the National Academy of Sciences*, vol. 99, pp. 11593–11598, Sept. 2002.

[221] S. Rankin, A. P. Reszka, J. Huppert, M. Zloh, G. N. Parkinson, A. K. Todd, S. Ladame, S. Balasubramanian, and S. Neidle, "Putative dna quadruplex formation within the human c-kit oncogene," *J. Am. Chem. Soc.*, vol. 127, pp. 10584–10589, Aug. 2005.

[222] S. Cogoi and L. E. Xodo, "G-quadruplex formation within the promoter of the kras proto-oncogene and its effect on transcription," *Nucleic Acids Res*, vol. 34, pp. 2536–2549, May 2006.

[223] R. Hansel-Hertsch, M. Di Antonio, and S. Balasubramanian, "Dna g-quadruplexes in the human genome: detection, functions and therapeutic potential," *Nature Reviews Molecular Cell Biology*, vol. 18, pp. 279–284, May 2017.

[224] B. K. Mohanty, J. A. Q. Karam, B. V. Howley, A. C. Dalton, S. Grelet, T. Dincman, W. S. Streitfeld, J.-H. Yoon, L. Balakrishnan, W. J. Chazin, D. T. Long, and P. H. Howe, "Heterogeneous nuclear ribonucleoprotein e1 binds polycytosine dna and monitors genome integrity," *Life Sci. Alliance*, vol. 4, p. e202000995, Sept. 2021.

[225] D. Musumeci, C. Riccardi, and D. Montesarchio, "G-quadruplex forming oligonucleotides as anti-hiv agents," *Molecules*, vol. 20, no. 9, 2015.

[226] R. Perrone, M. Nadai, I. Frasson, J. A. Poe, E. Butovskaya, T. E. Smithgall, M. Palumbo, G. Palu, and S. N. Richter, "A dynamic g-quadruplex region regulates the hiv-1 long terminal repeat promoter," *J. Med. Chem.*, vol. 56, pp. 6521–6530, Aug. 2013.

[227] E. Ruggiero, I. Zanin, M. Terreri, and S. N. Richter, "G-quadruplex targeting in the fight against viruses: An update," *International Journal of Molecular Sciences*, vol. 22, no. 20, 2021.

[228] G. Liu, W. Du, X. Sang, Q. Tong, Y. Wang, G. Chen, Y. Yuan, L. Jiang, W. Cheng, D. Liu, Y. Tian, and X. Fu, "Rna g-quadruplex in tmprss2 reduces sars-cov-2 infection," *Nature Communications*, vol. 13, p. 1444, Mar. 2022.

[229] S. Neidle, "Quadruplex nucleic acids as novel therapeutic targets," *J. Med. Chem.*, vol. 59, pp. 5987–6011, July 2016.

[230] J.-L. Mergny, A.-T. Phan, and L. Lacroix, “Following g-quartet formation by uv-spectroscopy,” *FEBS Letters*, vol. 435, pp. 74–78, Sept. 1998.

[231] S. Paramasivan, I. Rujan, and P. H. Bolton, “Circular dichroism of quadruplex dnas: Applications to structure, cation effects and ligand binding,” *Quadruplex DNA*, vol. 43, pp. 324–331, Dec. 2007.

[232] C. V. Pagba, S. M. Lane, and S. Wachsmann-Hogiu, “Raman and surface-enhanced raman spectroscopic studies of the 15-mer dna thrombin-binding aptamer,” *J. Raman Spectrosc.*, vol. 41, no. 3, pp. 241–247, 2010.

[233] S. J. Friedman and A. C. Terentis, “Analysis of g-quadruplex conformations using raman and polarized raman spectroscopy,” *J. Raman Spectrosc.*, vol. 47, pp. 259–268, Mar. 2016.

[234] S. Di Fonzo, J. Amato, F. D’Aria, M. Caterino, F. D’Amico, A. Gessini, J. W. Brady, A. Cesaro, B. Pagano, and C. Giancola, “Ligand binding to g-quadruplex dna: new insights from ultraviolet resonance raman spectroscopy,” *Phys. Chem. Chem. Phys.*, vol. 22, no. 15, pp. 8128–8140, 2020.

[235] C. Zhang, C. Lu, Z. Jing, C. Wu, J.-P. Piquemal, J. W. Ponder, and P. Ren, “Amoeba polarizable atomic multipole force field for nucleic acids,” *J. Chem. Theory Comput.*, vol. 14, pp. 2084–2108, Apr. 2018.

[236] J. Rackers, Z. Wang, C. Lu, M. L. Laury, L. Lagardere, M. J. Schnieders, J.-P. Piquemal, P. Ren, and J. W. Ponder, “Tinker 8: software tools for molecular design,” *J. Chem. Theory Comput.*, vol. 14, pp. 5273–5289, Oct. 2018.

[237] D. Beeman, “Some multistep methods for use in molecular dynamics calculations,” *Journal of Computational Physics*, vol. 20, pp. 130–139, Feb. 1976.

[238] T. Darden, D. York, and L. Pedersen, “Particle mesh ewald: An n*log(n) method for ewald sums in large systems,” *J. Chem. Phys.*, vol. 98, pp. 10089–10092, June 1993.

[239] U. Essmann, L. Perera, M. L. Berkowitz, T. Darden, H. Lee, and L. G. Pedersen, “A smooth particle mesh ewald method,” *J. Chem. Phys.*, vol. 103, pp. 8577–8593, Nov. 1995.

[240] B. G. Levine, J. E. Stone, and A. Kohlmeyer, “Fast analysis of molecular dynamics trajectories with graphics processing units–radial distribution function histogramming,” *Journal of Computational Physics*, vol. 230, pp. 3556–3569, May 2011.

[241] C. Krafft, J. M. Benevides, and J. Thomas, George J., “Secondary structure polymorphism in oxytricha nova telomeric dna,” *Nucleic Acids Res*, vol. 30, pp. 3981–3991, Sept. 2002.

[242] M.-C. Bellissent-Funel, A. Hassanali, M. Havenith, R. Henchman, P. Pohl, F. Sterpone, D. van der Spoel, Y. Xu, and A. E. Garcia, “Water determines the structure and dynamics of proteins,” *Chem. Rev.*, vol. 116, no. 13, pp. 7673–7697, 2016. PMID: 27186992.

[243] D. M. Czajka, A. J. Finkel, C. S. Fischer, and J. J. Katz, "Physiological effects of deuterium on dogs," *Am. J. Physiology-Legacy Cont.*, vol. 201, no. 2, pp. 357–362, 1961. PMID: 13719048.

[244] N. M. Levinson, S. D. Fried, and S. G. Boxer, "Solvent-induced infrared frequency shifts in aromatic nitriles are quantitatively described by the vibrational stark effect," *J. Phys. Chem. B*, vol. 116, no. 35, pp. 10470–10476, 2012. PMID: 22448878.

[245] T. Schleif, M. Prado Merini, S. Henkel, and W. Sander, "Solvation effects on quantum tunneling reactions," *Acc. Chem. Res.*, vol. 55, no. 16, pp. 2180–2190, 2022. PMID: 35730754.

[246] C. J. Cramer and D. G. Truhlar, "A universal approach to solvation modeling," *Acc. Chem. Res.*, vol. 41, no. 6, pp. 760–768, 2008.

[247] P. Wu, X. Hu, and W. Yang, "λ-metadynamics approach to compute absolute solvation free energy," *J. Phys. Chem. Lett.*, vol. 2, no. 17, pp. 2099–2103, 2011.

[248] F. Lipparini, G. Scalmani, B. Mennucci, E. Cances, M. Caricato, and M. J. Frisch, "A variational formulation of the polarizable continuum model," *J. Chem. Phys.*, vol. 133, no. 1, p. 014106, 2010.

[249] B. Mennucci, "Continuum solvation models: What else can we learn from them?," *J. Phys. Chem. Lett.*, vol. 1, no. 10, pp. 1666–1674, 2010.

[250] T. Giovannini, F. Egidi, and C. Cappelli, "Molecular spectroscopy of aqueous solutions: a theoretical perspective," *Chem. Soc. Rev.*, vol. 49, no. 16, pp. 5664–5677, 2020.

[251] T. Giovannini and C. Cappelli, "Continuum vs. atomistic approaches to computational spectroscopy of solvated systems," *Chem. Commun.*, vol. 59, no. 38, pp. 5644–5660, 2023.

[252] A. Y. Ivanov, S. G. Stepanian, V. A. Karachevtsev, and L. Adamowicz, "Nucleoside conformers in low-temperature argon matrices: Fourier transform ir spectroscopy of isolated thymidine and deuterothymidine molecules and quantum-mechanical calculations," *Low Temperature Physics*, vol. 45, pp. 1008–1017, Sept. 2019.

[253] L. Beyere, P. Arboleda, V. Monga, and G. Loppnow, "The dependence of thymine and thymidine raman spectra on solvent," *Can. J. Chem.*, vol. 82, no. 6, pp. 1092–1101, 2004.

[254] J. W. Ponder, C. Wu, P. Ren, V. S. Pande, J. D. Chodera, M. J. Schnieders, I. Haque, D. L. Mobley, D. S. Lambrecht, R. A. DiStasio Jr, *et al.*, "Current status of the amoeba polarizable force field," *J. Phys. Chem. B*, vol. 114, no. 8, pp. 2549–2564, 2010.

[255] D. Loco, E. Polack, S. Caprasecca, L. Lagardere, F. Lipparini, J.-P. Piquemal, and B. Mennucci, "A qm/mm approach using the amoeba polarizable embedding: From ground state energies to electronic excitations," *J. Chem. Theory Comput.*, vol. 12, no. 8, pp. 3654–3661, 2016. PMID: 27340904.

[256] D. Loco, L. Lagardere, S. Caprasecca, F. Lipparini, B. Mennucci, and J.-P. Piquemal, "Hybrid qm/mm molecular dynamics with amoeba polarizable embedding," *J. Chem. Theory Comput.*, vol. 13, no. 9, pp. 4025–4033, 2017. PMID: 28759205.

[257] Y. Shi, Z. Xia, J. Zhang, R. Best, C. Wu, J. W. Ponder, and P. Ren, "Polarizable atomic multipole-based amoeba force field for proteins," *J. Chem. Theory Comput.*, vol. 9, no. 9, pp. 4046–4063, 2013.

[258] M. Stöhr and A. Tkatchenko, "Quantum mechanics of proteins in explicit water: The role of plasmon-like solute-solvent interactions," *Sci. Adv.*, vol. 5, no. 12, p. eaax0024, 2019.

[259] P. Homem-de Mello, B. Mennucci, J. Tomasi, and A. Da Silva, "The effects of solvation in the theoretical spectra of cationic dyes," *Theor. Chem. Acc.*, vol. 113, pp. 274–280, 2005.

[260] G. Bertaina, G. Di Liberto, and M. Ceotto, "Reduced rovibrational coupling cartesian dynamics for semiclassical calculations: Application to the spectrum of the zundel cation," *The Journal of Chemical Physics*, vol. 151, no. 11, p. 114307, 2019.

[261] G. Schwaab, R. Pérez de Tudela, D. Mani, N. Pal, T. K. Roy, F. Gabas, R. Conte, L. Durán Caballero, M. Ceotto, D. Marx, and M. Havenith, "Zwitter ionization of glycine at outer space conditions due to microhydration by six water molecules," *Physical Review Letters*, vol. 128, Jan. 2022.

[262] J. P. Klinman and A. Kohen, "Hydrogen tunneling links protein dynamics to enzyme catalysis," *Ann. Rev. Biochem.*, vol. 82, pp. 471–496, 2013.

[263] L. Wang, S. D. Fried, S. G. Boxer, and T. E. Markland, "Quantum delocalization of protons in the hydrogen-bond network of an enzyme active site," *Proc. Natl Acad. Sci.*, vol. 111, no. 52, pp. 18454–18459, 2014.

[264] A. Perez, M. E. Tuckerman, H. P. Hjalmarson, and O. A. Von Lilienfeld, "Enol tautomers of watson- crick base pair models are metastable because of nuclear quantum effects," *J. Am. Chem. Soc.*, vol. 132, no. 33, pp. 11510–11515, 2010.

[265] W. Fang, J. Chen, M. Rossi, Y. Feng, X.-Z. Li, and A. Michaelides, "Inverse temperature dependence of nuclear quantum effects in dna base pairs," *J. Phys. Chem. Lett.*, vol. 7, no. 11, pp. 2125–2131, 2016.

[266] A. Nandi, G. Laude, S. S. Khire, N. D. Gurav, C. Qu, R. Conte, Q. Yu, S. Li, P. L. Houston, S. R. Gadre, *et al.*, "Ring-polymer instanton tunneling splittings of tropolone and isotopomers using a δ-machine learned ccsd (t) potential: Theory and experiment shake hands," *Journal of the American Chemical Society*, vol. 145, no. 17, pp. 9655–9664, 2023.

[267] J. Meisner and J. Kästner, "Atom tunneling in chemistry," *Angew. Chemie Intl Ed.*, vol. 55, no. 18, pp. 5400–5413, 2016.

[268] C. Castro and W. L. Karney, "Heavy-atom tunneling in organic reactions," *Angew. Chemie*, vol. 132, no. 22, pp. 8431–8442, 2020.

[269] D. Marx, M. E. Tuckerman, J. Hutter, and M. Parrinello, "The nature of the hydrated excess proton in water," *Nature*, vol. 397, no. 6720, pp. 601–604, 1999.

[270] Q. Yu, C. Qu, P. L. Houston, R. Conte, A. Nandi, and J. M. Bowman, "q-aqua: A many-body ccsd(t) water potential, including four-body interactions, demonstrates the quantum nature of water from clusters to the liquid phase," *J. Phys. Chem. Lett.*, vol. 13, no. 22, pp. 5068–5074, 2022. PMID: 35652912.

[271] C. Qu, Q. Yu, P. L. Houston, R. Conte, A. Nandi, and J. M. Bowman, "Interfacing q-aqua with a polarizable force field: The best of both worlds," *Journal of Chemical Theory and Computation*, vol. 19, no. 12, pp. 3446–3459, 2023. PMID: 37249502.

[272] X. Zhu, M. Riera, E. F. Bull-Vulpe, and F. Paesani, "Mb-pol(2023): Sub-chemical accuracy for water simulations from the gas to the liquid phase," *Journal of Chemical Theory and Computation*, vol. 19, no. 12, pp. 3551–3566, 2023.

[273] A. D. Becke, "Density-functional exchange-energy approximation with correct asymptotic behavior," *Physical review A*, vol. 38, no. 6, p. 3098, 1988.

[274] C. Lee, W. Yang, and R. G. Parr, "Development of the colle-salvetti correlation-energy formula into a functional of the electron density," *Physical review B*, vol. 37, no. 2, p. 785, 1988.

[275] P. J. Stephens, F. J. Devlin, C. F. Chabalowski, and M. J. Frisch, "Ab initio calculation of vibrational absorption and circular dichroism spectra using density functional force fields," *The Journal of physical chemistry*, vol. 98, no. 45, pp. 11623–11627, 1994.

[276] R. Ditchfield, W. J. Hehre, and J. A. Pople, "Self-consistent molecular-orbital methods. ix. an extended gaussian-type basis for molecular-orbital studies of organic molecules," *J. Chem. Phys.*, vol. 54, pp. 724–728, 1971.

[277] W. J. Hehre, R. Ditchfield, and J. A. Pople, "Self-consistent molecular orbital methods. xii. further extensions of gaussian-type basis sets for use in molecular orbital studies of organic molecules," *J. Chem. Phys.*, vol. 56, pp. 2257–2261, 1972.

[278] P. C. Hariharan and J. A. Pople, "The influence of polarization functions on molecular orbital hydrogenation energies," *Theor. Chim. Acta*, vol. 28, pp. 213–222, 1973.

[279] S. Ehrlich, J. Moellmann, W. Reckien, T. Bredow, and S. Grimme, “System-dependent dispersion coefficients for the dft-d3 treatment of adsorption processes on ionic surfaces,” *Chem. Phys. Chem.*, vol. 12, no. 17, pp. 3414–3420, 2011.

[280] M. e. Frisch, G. Trucks, H. B. Schlegel, G. Scuseria, M. Robb, J. Cheeseman, G. Scalmani, V. Barone, G. Petersson, H. Nakatsuji, *et al.*, “Gaussian 16,” 2016.

[281] M. Bondanza, M. Nottoli, L. Cupellini, F. Lipparini, and B. Mennucci, “Polarizable embedding qm/mm: the future gold standard for complex (bio)systems?,” *Phys. Chem. Chem. Phys.*, vol. 22, pp. 14433–14448, 2020.

[282] F. Lipparini, “General linear scaling implementation of polarizable embedding schemes,” *J. Chem. Theory Comput.*, vol. 15, pp. 4312–4317, July 2019.

[283] M. Nottoli, M. Bondanza, P. Mazzeo, L. Cupellini, C. Curutchet, D. Loco, L. Lagardère, J. Piquemal, B. Mennucci, and F. Lipparini, “Qm/amoeba description of properties and dynamics of embedded molecules,” *WIREs Computational Molecular Science*, vol. 13, June 2023.

[284] L. Martínez, R. Andrade, E. G. Birgin, and J. M. Martínez, “Packmol: A package for building initial configurations for molecular dynamics simulations,” *Journal of computational chemistry*, vol. 30, no. 13, pp. 2157–2164, 2009.

[285] H. Lin and D. G. Truhlar, “Qm/mm: what have we learned, where are we, and where do we go from here?,” *Theor. Chem. Acc.*, vol. 117, pp. 185–199, 2007.

[286] M. W. van der Kamp and A. J. Mulholland, “Combined quantum mechanics/molecular mechanics (qm/mm) methods in computational enzymology,” *Biochem.*, vol. 52, no. 16, pp. 2708–2728, 2013.

[287] E. Brunk and U. Rothlisberger, “Mixed quantum mechanical/molecular mechanical molecular dynamics simulations of biological systems in ground and electronically excited states,” *Chem. Rev.*, vol. 115, no. 12, pp. 6217–6263, 2015.

[288] U. N. Morzan, D. J. Alonso de Armino, N. O. Foglia, F. Ramirez, M. C. Gonzalez Lebrero, D. A. Scherlis, and D. A. Estrin, “Spectroscopy in complex environments from qm–mm simulations,” *Chem. Rev.*, vol. 118, no. 7, pp. 4071–4113, 2018.

[289] M. A. Thompson, “Qm/mmpol: A consistent model for solute/solvent polarization. application to the aqueous solvation and spectroscopy of formaldehyde, acetaldehyde, and acetone,” *J. Phys. Chem.*, vol. 100, no. 34, pp. 14492–14507, 1996.

[290] L. Gagliardi, R. Lindh, and G. Karlström, “Local properties of quantum chemical systems: The loprop approach,” *J. Chem. Phys.*, vol. 121, no. 10, pp. 4494–4500, 2004.

[291] P. Soderhjelm, C. Husberg, A. Strambi, M. Olivucci, and U. Ryde, "Protein influence on electronic spectra modeled by multipoles and polarizabilities," *J. Chem. Theory Comput.*, vol. 5, no. 3, pp. 649–658, 2009.

[292] J. M. Olsen, K. Aidas, and J. Kongsted, "Excited states in solution through polarizable embedding," *J. Chem. Theory Comput.*, vol. 6, no. 12, pp. 3721–3734, 2010.

[293] K. Sneskov, T. Schwabe, J. Kongsted, and O. Christiansen, "The polarizable embedding coupled cluster method," *J. Chem. Phys.*, vol. 134, 03 2011. 104108.

[294] V. Macaluso, S. Hashem, M. Nottoli, F. Lipparini, L. Cupellini, and B. Mennucci, "Ultrafast transient infrared spectroscopy of photoreceptors with polarizable qm/mm dynamics," *J. Phys. Chem. B*, vol. 125, pp. 10282–10292, Sept. 2021.

[295] G. Salvadori, V. Macaluso, G. Pellicci, L. Cupellini, G. Granucci, and B. Mennucci, "Protein control of photochemistry and transient intermediates in phytochromes," *Nat. Commun.*, vol. 13, no. 1, p. 6838, 2022.

[296] M. Nottoli and F. Lipparini, "General formulation of polarizable embedding models and of their coupling," *J. Chem. Phys.*, vol. 153, no. 22, p. 224108, 2020.

[297] B. T. Thole, "Molecular polarizabilities calculated with a modified dipole interaction," *Chem. Phys.*, vol. 59, no. 3, pp. 341–350, 1981.

[298] P. T. Van Duijnen and M. Swart, "Molecular and atomic polarizabilities: Thole's model revisited," *J. Phys. Chem. A*, vol. 102, no. 14, pp. 2399–2407, 1998.

[299] S. Miertus, E. Scrocco, and J. Tomasi, "Electrostatic interaction of a solute with a continuum. a direct utilizaion of ab initio molecular potentials for the prevision of solvent effects," *Chem. Phys.*, vol. 55, no. 1, pp. 117–129, 1981.

[300] R. Cammi and J. Tomasi, "Remarks on the use of the apparent surface charges (asc) methods in solvation problems: Iterative versus matrix-inversion procedures and the renormalization of the apparent charges," *J. Comput. Chem.*, vol. 16, no. 12, pp. 1449–1458, 1995.

[301] E. Cances, B. Mennucci, and J. Tomasi, "A new integral equation formalism for the polarizable continuum model: Theoretical background and applications to isotropic and anisotropic dielectrics," *J. Chem. Phys.*, vol. 107, no. 8, pp. 3032–3041, 1997.

[302] V. Barone and M. Cossi, "Quantum calculation of molecular energies and energy gradients in solution by a conductor solvent model," *J. Phys. Chem. A*, vol. 102, no. 11, pp. 1995–2001, 1998.

[303] G. Scalmani and M. J. Frisch, "Continuous surface charge polarizable continuum models of solvation. i. general formalism," *J. Chem. Phys.*, vol. 132, no. 11, p. 114110, 2010.

[304] B. Mennucci, “Polarizable continuum model,” *Wiley Interdisciplinary Reviews: Computational Molecular Science*, vol. 2, no. 3, pp. 386–404, 2012.

[305] S. L. Zhang, K. H. Michaelian, and G. R. Loppnow, “Vibrational spectra and experimental assignments of thymine and nine of its isotopomers,” *The Journal of Physical Chemistry A*, vol. 102, no. 2, pp. 461–470, 1998.

[306] F. Gabas, R. Conte, and M. Ceotto, “Quantum vibrational spectroscopy of explicitly solvated thymidine in semiclassical approximation,” *J. Phys. Chem. Lett.*, vol. 13, pp. 1350–1355, Feb. 2022.

[307] W. L. Jorgensen, “Quantum and statistical mechanical studies of liquids. 10. transferable intermolecular potential functions for water, alcohols, and ethers. application to liquid water,” *J. Am. Chem. Soc.*, vol. 103, no. 2, pp. 335–340, 1981.

[308] H. C. Urey and C. A. Bradley Jr, “The vibrations of pentatonic tetrahedral molecules,” *Phys. Rev.*, vol. 38, no. 11, p. 1969, 1931.

[309] N. Michaud-Agrawal, E. J. Denning, T. B. Woolf, and O. Beckstein, “Mdanalysis: a toolkit for the analysis of molecular dynamics simulations,” *Journal of computational chemistry*, vol. 32, no. 10, pp. 2319–2327, 2011.

[310] R. J. Gowers, M. Linke, J. Barnoud, T. J. Reddy, M. N. Melo, S. L. Seyler, J. Domanski, D. L. Dotson, S. Buchoux, I. M. Kenney, *et al.*, “Mdanalysis: a python package for the rapid analysis of molecular dynamics simulations,” in *Proceedings of the 15th python in science conference*, vol. 98, p. 105, SciPy Austin, TX, 2016.

[311] B. Jeziorski, R. Moszynski, and K. Szalewicz, “Perturbation theory approach to intermolecular potential energy surfaces of van der waals complexes,” *Chemical Reviews*, vol. 94, no. 7, pp. 1887–1930, 1994.

[312] H.-J. Werner, P. J. Knowles, F. R. Manby, J. A. Black, K. Doll, A. Heelmann, D. Kats, A. Kohn, T. Korona, D. A. Kreplin, *et al.*, “The molpro quantum chemistry package,” *The Journal of chemical physics*, vol. 152, no. 14, 2020.

[313] A. K. Belyaev, D. T. Colbert, G. C. Groenenboom, and W. H. Miller, “State-to-state reaction probabilities for $h - +h2, d2$ collisions,” *Chemical physics letters*, vol. 209, no. 4, pp. 309–314, 1993.

[314] R. Kapral and G. Ciccotti, “Mixed quantum-classical dynamics,” *The Journal of chemical physics*, vol. 110, no. 18, pp. 8919–8929, 1999.

[315] D. Mac Kernan, G. Ciccotti, and R. Kapral, “Surface-hopping dynamics of a spin-boson system,” *The Journal of chemical physics*, vol. 116, no. 6, pp. 2346–2353, 2002.

[316] J. E. Subotnik, W. Ouyang, and B. R. Landry, “Can we derive tully’s surface-hopping algorithm from the semiclassical quantum liouville equation? almost, but only with decoherence,” *The Journal of chemical physics*, vol. 139, no. 21, 2013.

[317] Y. Wu and M. F. Herman, “Nonadiabatic surface hopping herman-kluk semiclassical initial value representation method revisited: Applications to tully’s three model systems,” *The Journal of chemical physics*, vol. 123, no. 14, 2005.

[318] M. Thoss and G. Stock, “Mapping approach to the semiclassical description of nonadiabatic quantum dynamics,” *Physical Review A*, vol. 59, no. 1, p. 64, 1999.

[319] J. E. Runeson and J. O. Richardson, “Spin-mapping approach for nonadiabatic molecular dynamics,” *The Journal of Chemical Physics*, vol. 151, July 2019.

[320] J. E. Runeson and J. O. Richardson, “Generalized spin mapping for quantum-classical dynamics,” *J. Chem. Phys.*, vol. 152, p. 084110, Feb. 2020.

[321] J. R. Mannouch and J. O. Richardson, “A mapping approach to surface hopping,” *The Journal of Chemical Physics*, vol. 158, no. 10, 2023.

[322] J. E. Runeson and D. E. Manolopoulos, “A multi-state mapping approach to surface hopping,” *The Journal of Chemical Physics*, vol. 159, no. 9, 2023.

[323] J. Liu, “A unified theoretical framework for mapping models for the multi-state hamiltonian,” *The Journal of Chemical Physics*, vol. 145, no. 20, 2016.

[324] B. Wu, X. He, and J. Liu, “Nonadiabatic field on quantum phase space: A century after ehrenfest,” *The Journal of Physical Chemistry Letters*, vol. 15, no. 2, pp. 644–658, 2024.

[325] J. E. Lawrence, J. R. Mannouch, and J. O. Richardson, “Recovering marcus theory rates and beyond without the need for decoherence corrections: The mapping approach to surface hopping,” *The Journal of Physical Chemistry Letters*, vol. 15, no. 3, pp. 707–716, 2024.

[326] J. E. Lawrence, I. M. Ansari, J. R. Mannouch, M. A. Manae, K. Asnaashari, A. Kelly, and J. O. Richardson, “A mash simulation of the photoexcited dynamics of cyclobutanone,” *The Journal of Chemical Physics*, vol. 160, no. 17, 2024.

[327] K. Polley and R. F. Loring, “Two-dimensional vibronic spectroscopy with semiclassical thermofield dynamics,” *The Journal of Chemical Physics*, vol. 156, no. 12, 2022.

[328] J. Provazza, F. Segatta, M. Garavelli, and D. F. Coker, “Semiclassical path integral calculation of nonlinear optical spectroscopy,” *Journal of chemical theory and computation*, vol. 14, no. 2, pp. 856–866, 2018.

[329] N. Ananth, “Mapping variable ring polymer molecular dynamics: A path-integral based method for nonadiabatic processes,” *The Journal of chemical physics*, vol. 139, no. 12, 2013.

[330] J. O. Richardson and M. Thoss, "Communication: Nonadiabatic ring-polymer molecular dynamics," *The Journal of chemical physics*, vol. 139, no. 3, 2013.

[331] J.-X. Zeng and X.-Z. Li, "Semiclassical reaction rate constant of non-adiabatic system by means of initial value representation," *AIP Advances*, vol. 14, no. 3, 2024.

[332] S. Bonella and D. F. Coker, "Semiclassical implementation of the mapping hamiltonian approach for nonadiabatic dynamics using focused initial distribution sampling," *The Journal of Chemical Physics*, vol. 118, p. 4370–4385, Mar. 2003.

[333] S. Bonella and D. Coker, "Land-map, a linearized approach to nonadiabatic dynamics using the mapping formalism," *The Journal of chemical physics*, vol. 122, no. 19, 2005.

[334] W. Domcke, H. Koppel, and L. Cederbaum, "Spectroscopic effects of conical intersections of molecular potential energy surfaces," *Molecular Physics*, vol. 43, no. 4, pp. 851–875, 1981.

[335] H. Köppel, L. Cederbaum, and W. Domcke, "Strong nonadiabatic effects and conical intersections in molecular spectroscopy and unimolecular decay: C2h4+," *The Journal of Chemical Physics*, vol. 77, no. 4, pp. 2014–2022, 1982.

[336] U. Muller and G. Stock, "Consistent treatment of quantum-mechanical and classical degrees of freedom in mixed quantum-classical simulations," *The Journal of chemical physics*, vol. 108, no. 18, pp. 7516–7526, 1998.

[337] G. Di Liberto and M. Ceotto, "The importance of the pre-exponential factor in semiclassical molecular dynamics," *The Journal of Chemical Physics*, vol. 145, no. 14, 2016.

[338] M. Feit, J. Fleck Jr, and A. Steiger, "Solution of the schrodinger equation by a spectral method," *Journal of Computational Physics*, vol. 47, no. 3, pp. 412–433, 1982.

[339] C. Cattarius, G. A. Worth, H.-D. Meyer, and L. Cederbaum, "All mode dynamics at the conical intersection of an octa-atomic molecule: Multi-configuration time-dependent hartree (mctdh) investigation on the butatriene cation," *The Journal of chemical physics*, vol. 115, no. 5, pp. 2088–2100, 2001.

[340] F. Brogli, E. Heilbronner, E. Kloster-Jensen, A. Schmelzer, A. Manocha, J. Pople, and L. Radom, "The photoelectron spectrum of butatriene," *Chemical Physics*, vol. 4, no. 1, pp. 107–119, 1974.

[341] C. Woywod, W. Domcke, A. L. Sobolewski, and H.-J. Werner, "Characterization of the s1 - s2 conical intersection in pyrazine using ab initio multiconfiguration self-consistent-field and multireference configuration-interaction methods," *The Journal of chemical physics*, vol. 100, no. 2, pp. 1400–1413, 1994.

[342] P.-Y. Yang and J. Cao, “Quantum effects in chemical reactions under polaritonic vibrational strong coupling,” *The Journal of Physical Chemistry Letters*, vol. 12, no. 39, pp. 9531–9538, 2021.

[343] T. E. Li, B. Cui, J. E. Subotnik, and A. Nitzan, “Molecular polaritonics: Chemical dynamics under strong light–matter coupling,” *Annual review of physical chemistry*, vol. 73, no. 1, pp. 43–71, 2022.

[344] J. Fregoni, F. J. Garcia-Vidal, and J. Feist, “Theoretical challenges in polaritonic chemistry,” *ACS photonics*, vol. 9, no. 4, pp. 1096–1107, 2022.

[345] Y. Ke and J. O. Richardson, “Quantum nature of reactivity modification in vibrational polariton chemistry,” *The Journal of chemical physics*, vol. 161, no. 5, 2024.

APPENDIX A

A BRIEF DIGRESSION ON BOHMIAN DYNAMICS

In this appendix will be shown how to derive the quantum equations of motion found by David Bohm in his "hydrodynamic" formulation of quantum mechanics For an F-dimensional system with a generic collisional Hamiltonian

$$\hat{H} = \sum_{J=1}^{F} -\frac{\hbar^2}{2M_J}\nabla^2_{q_J} + V(\mathbf{q}) \ . \tag{A.1}$$

It is possible to start by defining a trial wavefunction as

$$\Psi(\mathbf{q},t) = A(\mathbf{q},t)e^{\frac{i}{\hbar}S(\mathbf{q},t)} \ , \tag{A.2}$$

where $A,\ S : \mathbb{R}^{F+1} \ \rightarrow \ \mathbb{R}$ are the amplitude and phase respectively. By inserting eq. A.2 into the time dependent Shcroedinger equation (TDSE) and by splitting it into a real part and an imaginary part one obtains a set of two coupled Partial Differential Equations (PDEs)

$$\begin{cases} \frac{\partial S}{\partial t}\left(\mathbf{q},t\right) & = \sum_{J=1}^{F} \frac{\hbar^2}{2M_J} \frac{\nabla_{q_J}^2 A(\mathbf{q},t)}{A(\mathbf{q},t)} - \sum_{J=1}^{F} \frac{\left(\nabla_{q_J} S(\mathbf{q},t)\right)^2}{2M_J} - V\left(\mathbf{q}\right) \\ \frac{\partial A}{\partial t}\left(\mathbf{q},t\right) & = \sum_{J=1}^{F} \left[-\frac{1}{M_J}\nabla_{q_J} A\left(\mathbf{q},t\right)\nabla_{q_J} S\left(\mathbf{q},t\right) - \frac{A(\mathbf{q},t)}{2M_J}\nabla_{q_J}^2 S\left(\mathbf{q},t\right)\right] \end{cases} , \qquad (A.3)$$

eqs. A.3 are now the new TDSEs for the phase and the amplitude of the total wavefunction. The equation of the amplitude can be easily rewritten in terms of probability density since $A^2\left(\mathbf{q},t\right) = \left|\Psi\left(\mathbf{q},t\right)\right|^2 = \rho\left(\mathbf{q},t\right)$. By applying this definition of the density to the amplitude TDSE one obtains a continuity equation

$$\begin{aligned} \frac{\partial \rho}{\partial t}\left(\mathbf{q},t\right) &= \sum_{J=1}^{F} \left[-\frac{1}{M_J}\nabla_{q_J}\rho\left(\mathbf{q},t\right)\nabla_{q_J} S\left(\mathbf{q},t\right) - \frac{\rho\left(\mathbf{q},t\right)}{M_J}\nabla_{q_J}^2 S\left(\mathbf{q},t\right)\right] \\ &= -M^{-1}\nabla_{\mathbf{q}}\left[\rho\left(\mathbf{q},t\right)\nabla_{\mathbf{q}} S\left(\mathbf{q},t\right)\right] \ . \end{aligned} \qquad (A.4)$$

With analogy to fluid dynamics the equation can be solved using a fixed framework where the term $\rho\left(\mathbf{q},t\right)\nabla_{\mathbf{q}} S\left(\mathbf{q},t\right)$ is considered as a flux $\mathbf{g}\left(\mathbf{q},t\right)$ with momentum $M\mathbf{v} = \nabla_{\mathbf{q}} S\left(\mathbf{q},t\right)$. Otherwise, one can also consider the Lagrangian or moving frame in which $\mathbf{q}$ becomes a time-dependent variable. This implies that

$$\frac{d}{dt}\rho\left(\mathbf{q}(t),t\right) = \frac{\partial \rho}{\partial t}\left(\mathbf{q}(t),t\right) + \nabla_{\mathbf{q}}\rho\left(\mathbf{q}(t),t\right)\dot{\mathbf{q}}(t) \ , \qquad (A.5)$$

in this framework $S(\mathbf{q}(t),t)$ is considered as the Hamilton's action, therefore it is possible to insert in equation A.4 the known identity $\nabla_{\mathbf{q}} S\left(\mathbf{q}(t),t\right) = M\dot{\mathbf{q}}(t)$, by inserting this identity in eq. A.4 and then in A.5 one can obtain

$$\frac{d}{dt}\rho\left(\mathbf{q}(t),t\right) = -\rho\left(\mathbf{q}(t),t\right)\nabla_{\mathbf{q}}\dot{\mathbf{q}}(t) \ . \qquad (A.6)$$

Returning to the other TDSE which will propagate the phase we can rearrange it as

$$\frac{\partial S\left(\mathbf{q}(t),t\right)}{\partial t} + \frac{M^{-1}}{2}\left(\nabla_{\mathbf{q}} S\left(\mathbf{q}(t),t\right)\right)^T\left(\nabla_{\mathbf{q}} S\left(\mathbf{q}(t),t\right)\right) + V\left(\mathbf{q}(t)\right) + Q\left[\rho\left(\mathbf{q}(t),t\right)\right] = 0 \ , \qquad (A.7)$$

where the functional $Q\left[\rho\left(\mathbf{q}(t),t\right)\right]$ is what is often referred as the quatum potential, which is defined as

$$Q\left[\rho\left(\mathbf{q}(t),t\right)\right] = \sum_{J=1}^{F} -\frac{\hbar^2}{2M_J}\frac{\nabla_{q_J}^2\sqrt{\rho\left(\mathbf{q}(t),t\right)}}{\sqrt{\rho\left(\mathbf{q}(t),t\right)}} \ . \tag{A.8}$$

A closer look at eq. A.7 will show that the TDSE for the phase is actually identical to the Hamilton-Jacobi (HJ) equation with an additional term that is responsible for the quantum mechanical behaviour. From equation A.7 by considering its gradient one can also find out that the EOMs of the reference frame $\mathbf{q}(t)$ are actually given by

$$M\ddot{\mathbf{q}}(t) = -\nabla_{\mathbf{q}}V\left(\mathbf{q}(t)\right) - \nabla_{\mathbf{q}}Q\left[\rho\left(\mathbf{q}(t),t\right)\right] \ , \tag{A.9}$$

which resemble classical EOMs. One big difference in this case is that the quantum force is a non-local field of which the evaluation can be cumbersome.